STABILITY OF HIGH-SPEED, THREE-DIMENSIONAL BOUNDARY LAYERS

A Dissertation

by

STUART ALEXANDER CRAIG

Submitted to the Office of Graduate and Professional Studies of
Texas A&M University
in partial fulfillment of the requirements for the degree of

DOCTOR OF PHILOSOPHY

Chair of Committee,	William S. Saric
Committee Members,	Helen L. Reed
	Rodney D. W. Bowersox
	Simon W. North
	Eli Reshotko
Head of Department,	Rodney D. W. Bowersox

May 2015

Major Subject: Aerospace Engineering

ABSTRACT

Boundary-layer experiments are performed in the low-disturbance, Mach 6 Quiet Tunnel (M6QT) at Texas A&M University. The experiments are focused specifically on investigating the physics of two three-dimensional phenomena in hypersonic boundary-layer stability and transition: the breakdown of second-mode waves and the growth and breakdown of crossflow waves. In order to enable these experiments, a new, three-dimensional probe traversing mechanism was designed and constructed.

In order to investigate the breakdown of second-mode waves, experiments are conducted on a flared cone with a 5° half angle at the tip at zero angle of attack. Experiments were typically performed at unit Reynolds number $Re' \approx 10 \times 10^6$/m with a slightly hot wall, $T/T_{aw} \approx 1.05$. A new, durable method of roughness element application is discussed for the purpose of exciting the unstable waves. Hot-wire measurements were made of the boundary layer and it is shown that even with roughness elements, transition to turbulence does not occur on the model. Therefore, the expected Λ vortices are not observed.

The crossflow instability in a hypersonic boundary layer is studied on a 7° right circular cone at 5.6° angle of incidence. Experiments were performed at $Re' \approx 10 \times 10^6$/m with an adiabatic wall. Hot wire measurements are made at a series of axial locations to generate contours of streamwise mass flux. The stationary vortex structure is shown through its saturation. Traveling waves are observed in the expected frequency range, 10 kHz to 60 kHz, predicted by computations and are located generally in the high-speed troughs in the vortex structure. Secondary instability is observed between 80 kHz and 130 kHz. Frequency scaling and location is shown to agree with low-speed experiments and good preliminary agreement with

hypersonic computations is obtained. Transition does not naturally occur on the model. Distributed roughness is applied to the tip in order to excite crossflow and cause transition. Transition is shown to occur with the rough tip, but is not likely a result of crossflow.

To my wife and family for their support and patience.

ACKNOWLEDGEMENTS

This work would not be possible without the input and support provided by a number of people. First and foremost, I offer my thanks to my committee chair and advisor, Dr. William Saric. The opportunities for growth I have been afforded under his guidance have been invaluable. I am truly grateful for the chance to learn from his extensive experience and the opportunity I have had to truly take ownership of the research under his guidance.

I would also like to thank Dr. Rodney Bowersox for all of the discussions and advice throughout this process. Dr. Helen Reed has also been especially helpful, both for her computational support and the discussions that often helped me look at the problems from a different perspective. The rest of my committee, Dr. Simon North and Dr. Eli Reshotko, are also acknowledged for their ongoing support.

These experiments involved many long days and nights, and I am indebted to my colleagues at the *National Aerothermochemistry Laboratory* for their help and cooperation. In particular I would like to thank Dr. Jerrod Hofferth and Dr. Ray Humble for all the discussion and advice they've provided.

Finally, I'd like to thank Ms. Colleen Leatherman for all of the support and general cheerfulness over the last several years. The lab would not function properly without her.

This work was principally funded by NASA and AFOSR through the *National Center for Hypersonic Laminar-Turbulent Transition Research* (AFOSR Grant FA9550-09-1-0341) and through the Texas A&M Foundation through the George Eppright '26 Chair in Engineering.

NOMENCLATURE

Acronyms

DNS	direct numerical simulation
DRE	discrete roughness element
FSD	focusing schlieren deflectometry
IR	infrared
LaRC	Langley Research Center
LFC	laminar flow control
LST	linear stability theory
LPSE	linear parabolized stability equations
M6NTC	Advanced Mach 6 Quiet Tunnel in the Nozzle Test Chamber
M6QT	Mach 6 Quiet Tunnel
NAL	National Aerothermochemistry Laboratory
NASA	National Aeronautics and Space Administration
NPSE	nonlinear parabolized stability equations
NS	Navier-Stokes
QTC	quiet test core
TAMU	Texas A&M University
TAMU 7DC	TAMU 7-degree cone model
TPS	thermal protection system

Symbols

d	hot-wire diameter
D	d/dy
k	wavenumber, roughness height

k_c	circumferential wavenumber $[1/2\pi]$
ℓ	hot-wire active length
M	Mach number
$\overline{M}$	relative Mach number
M_e	edge Mach number
N	N-factor, $\ln(A/A_0)$
r	radial coordinate
Re	Reynolds number, $\rho u L/\mu$
Re_d	Reynolds number based on wire diameter
Re_{kk}	Reynolds number at roughness height, k, using flow conditions at k
Re_{tr}	Reynolds number at the transition location
Re'	unit Reynolds number
T	temperature
T_{aw}	adiabatic wall temperature
V	voltage
z	axial coordinate

Greek symbols

α	$\alpha = \alpha_r + i\alpha_i$, wavenumber in the streamwise direction
β	$\beta = \beta_r + i\beta_i$, wavenumber in the spanwise direction
λ	wavelength
θ	azimuthal coordinate
ϕ_c	cone half angle
ω	angular frequency

Subscripts

0	stagnation condition

aw	adiabatic wall condition
fs	free-stream condition
t	total conditions
tr	transition conditions
w	near-wall condition

TABLE OF CONTENTS

LIST OF FIGURES

FIGURE Page

LIST OF TABLES

TABLE Page

1. INTRODUCTION

1.1 Background and motivation

Boundary-layer trasition on hypersonic vehicles is of paramount importance to their safe and efficient design as a result of the substantial increase in thermal load associated with a turbulent boundary layer. Substantial progress has been achieved in recent years as a result of cooperation between experiments, computations, and theory, particularly for the class of flows dominated by Mack's (1984) acoustic second-mode instability (Fedorov, 2011). Comparatively little attention has been paid to the crossflow instability, which dominates the three-dimensional boundary layers that arise on common hypersonic vehicle geometries such as swept surfaces and conical bodies at angle of attack.

Hypersonic vehicle designs are extraordinarily sensitive to the state of the boundary layer. These vehicles owe their survival to their ability to manage the thermal load due to aerodynamic heating and their ability to generate thrust to efficient mixing of the fuel and air. As turbulence enhances both heating and mixing, developing a physics-based theory for boundary-layer transition in hypersonic flows is a key enabling technology for the development of hypersonic vehicles. Despite its importance, such a predictive tool does not yet exist and vehicle designers have been forced to rely on empirical and vehicle-specific correlation methods with limited utility such as Re_θ/M_e (Reshotko, 2007). Poor predictive tools have led to the over-design of the thermal protection system on most hypersonic vehicles to date and scramjet engines continue to be plagued by poor performance and unstart related to insufficient understanding of the transition process (Borg & Schneider, 2008).

The ubiquity of subsonic swept-wing aircraft has motivated substantial investment

in the study of the crossflow instability at subsonic speeds and the experimental data on swept-wing models are quite rich (Saric *et al.*, 2003; White & Saric, 2005). However, a number of practical issues have led to the scarcity of similar experiments in hypersonic flows. The cost of flight-testing hypersonic vehicles is often prohibitive, as is the development of new hypersonic, low-disturbance wind tunnels, which are required for conducting meaningful transition experiments (Schneider, 2007). At present, only two such facilities are operational: a Ludwieg tube at Purdue University and a blowdown wind tunnel at Texas A&M University.

The present study seeks to fill this gap in experimental hypersonic boundary-layer data. The Mach 6 Quiet Tunnel (M6QT) facility at Texas A&M University, featuring a thirty-second run time and three-dimensional traversing mechanism, is uniquely suited for boundary layer measurements of this kind. Of particular interest is the degree to which the primary and secondary instability mechanisms mimic their subsonic counterparts and how well existing hypersonic theory and computations match with these experimental data.

1.2 Introduction to the transition process

The study of boundary-layer transition has been of theoretical and practical interest to the fluid dynamics community since the turn of the century, when Reynolds (1883) made his famous observations of turbulence in pipe flows and Prandtl (1904) developed the theory of the boundary layer. The studies over the ensuing century have shed light on a large portion of the process and are often distilled into a graphical overview known as the transition road map (Figure 1.1), which lays out the various paths a boundary layer may take from its laminar inception to the onset of turbulence. A boundary layer is a highly nonlinear dynamical system subject to a variety of stable and unstable waves, some of which may grow to such amplitude as to break down to

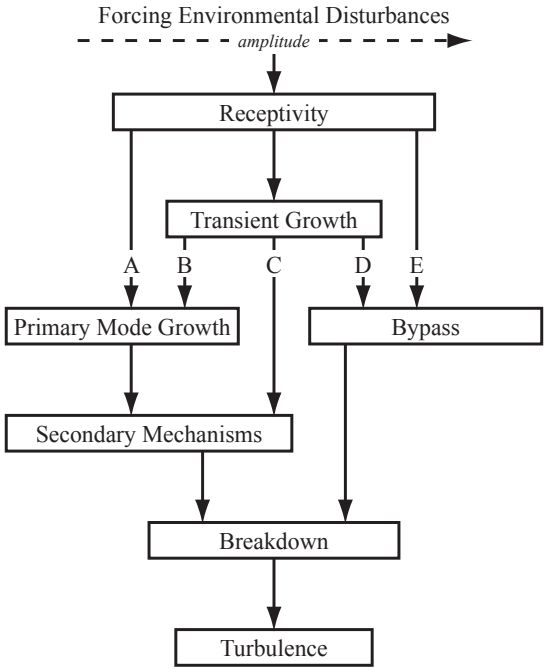

Figure 1.1: The transition road map

turbulence.

The genesis of the small boundary-layer disturbances lies in the free stream, where small fluctuations in the external flow (e.g. sound, vorticity, or entropy) interact with features of the surface such as roughness and become entrained in the incipient boundary layer through a process known as receptivity (Saric *et al.*, 2002). The receptivity process itself is poorly understood, but the end result is a spectrum of small disturbances within the boundary layer, some of which are dynamically unstable. The stability and transition problem therefore amounts to a nonlinear initial value problem governed by the Navier-Stokes equations whose initial conditions are those provided by the receptivity process. The path in Figure 1.1 followed for a given boundary layer depends on the magnitude of the initial conditions.

With this in mind, Figure 1.1 begins at the top with the forcing environmental

disturbances and receptivity. The road map lays out the various paths to turbulence such that the phenomena are ordered from left to right by increasing initial disturbance amplitude. The most commonly observed path in flight, and that which is of greatest interest to the present work, is *path A*. This path begins with the smallest initial disturbances and comprises four stages: receptivity, primary-mode growth, secondary mechanisms, and breakdown to turbulence. The initial growth phases of both the primary wave and the secondary mechanisms may often be modeled linearly. Continued mode growth eventually reaches the point where nonlinear terms can no longer be neglected and play a major role in the remainder of the transition process.

For very large initial disturbances (*path E*), the boundary layer undergoes a process known as bypass. In these situations, the boundary layer effectively bypasses all known boundary-layer instability mechanisms and transitions directly to turbulence. This path represents all instances of boundary layers for which no mechanism has yet been found to explain the observed transition.

For initial disturbances that fall between the levels required for *paths A* and *E*, a boundary layer may undergo transient growth. Transient growth results when two nonorthogonal modes, which are each linearly stable, interact to produce a resultant mode that grows algebraically (Landahl, 1980; Gustavsson, 1991; Butler & Farrell, 1992; Schmid *et al.*, 1993; Trefethen *et al.*, 1993; Reshotko, 2001) even while both individual modes decay. This slowly-growing disturbance can then lead to one of three phenomena depending on the intitial disturbance amplitude. Relatively small amplitudes may follow *path B*, whereby the disturbance energy from the transient growth helps amplify primary instability mechanisms in the boundary layer. For larger initial amplitude, transient growth may result in modification to the mean flow that is large enough to lead directly to the development of secondary instability mechanisms, cutting out primary modes altogether (*path C*). Finally, for large initial

amplitude, the process may follow *path D* and the modified boundary layer may be so unstable that it triggers bypass transition.

1.3 Linear stability theory

Much of the current theoretical understanding of the laminar-turbulent transition process is grounded in linear stability theory (LST). A boundary layer is a nonlinear dynamical system subject to instability in the same way as any other dynamical system. The highly nonlinear nature of the full Navier-Stokes (NS) equations makes direct solution difficult; however, the initial growth of small-amplitude disturbances within the boundary layer can be accurately described through a much simpler linear stability analysis. LST is treated at length by Mack (1984). However, several important features of the compressible stability problem can be highlighted by a brief discussion of the inviscid problem.

A LST analysis begins by assuming small perturbations to the full NS equations. These are implemented by writing the flow quantities as a sum of a time-independent mean component and a small fluctuating component, for example

$$u(\vec{x},t) = U(\vec{x}) + u'(\vec{x},t), \tag{1.1}$$

where $\vec{x}$ is the spatial coordinate and t is time. These are then substituted into the dimensionless, compressible NS equations, continuity equation, and energy equation. The mean flow terms identically satisfy the NS equations and fall out of the equations. Assuming the perturbations remain small, the equations are linearized. This leaves a six-equation system describing the evolution of the perturbation quantities. At this point, the analysis may follow a number of different routes. Typically, the flow is

assumed to be locally parallel and a normal mode solution is assumed of the form

$$q(x, y, z, t) = \hat{q}(y) \exp\left[i\left(\alpha x + \beta z - \omega t\right)\right], \tag{1.2}$$

where q is simply a variable representing any of the disturbance quantities. α and β represent the x and z components of the wavenumber vector, $\vec{k}$, and ω is the angular frequency of the disturbance. In general, *alpha* and β are complex and ω is real. The result is an eighth-order system of six equations describing the linear stability of the small perturbations.

The equations can be further manipulated by introducing the relative Mach number

$$\overline{M} = \frac{(\alpha U + \beta W - \omega)}{(\alpha^2 + \beta^2)^{1/2}} \frac{M_e}{T^{1/2}}. \tag{1.3}$$

The physical meaning of this "relative Mach number" is revealed by rewriting the definition as follows:

$$\overline{M} = \left(\frac{\vec{V} \cdot \vec{k}}{k} - \frac{\omega}{k}\right) \frac{M_e}{T^{1/2}} = M_{||} - \frac{c}{a}. \tag{1.4}$$

The relative Mach number therefore represents the Mach number of the mean flow in the direction of $\vec{k}$, $(M_{\|})$, relative to the phase speed (c). Using this definition, the inviscid stability equations can be written in the form

$$\frac{\partial^2 \psi}{\partial y^2} + \left(1 - \overline{M}^2\right) \frac{\partial^2 \psi}{\partial x^2} + f\left(\overline{M}, \psi, \frac{\partial \psi}{\partial y}\right) = 0. \tag{1.5}$$

The analytical character of Eq. 1.5 changes depending on the value of $\overline{M}^2$. When $\overline{M}^2 < 1$, the solutions are elliptic and a unique α exists for a given c (Lees & Lin, 1946). All subsonic boundary layers fit into this category. However, when $\overline{M}^2 > 1$,

the solutions are hyperbolic and an infinite series of wavenumbers may satisfy the governing equation. This leaves open the possibility that many inviscid modes may exist in a given supersonic boundary layer. These modes only exist in the region where $\overline{M} > 1$ (between some sonic line, y_a, and the wall) and represent a family of trapped acoustic waves reflecting back and forth between the wall and the sonic line. Depending on the flow conditions, these additional acoustic modes may be the most unstable (Mack, 1969, 1984).

It is also important to note that Rayleigh's criterion for inviscid instability in an incompressible flow does not hold for compressible flows. Instead, a modified form, the generalized inflection point, exists. For a compressible boundary layer, the necessary and sufficient condition for inviscid instability is that at some point $y_s > y_c$,

$$D(\rho DU) = 0. \tag{1.6}$$

Here, y_c is the point in the boundary layer where $U(y_c) = 1 - 1/M_e$, M_e is the edge Mach number, $D = d/dy$, and y represents the wall-normal direction. As a result, in contrast to the incompressible case, even a compressible boundary layer over a zero-pressure-gradient flat plate is always unstable to inviscid waves (Mack, 1984; Reed *et al.*, 1996).

Historically, the so-called e^N method proposed independently by Smith & Gamberoni (1956) and Van Ingen (1956) has been used to correlate LST predictions with transition in experiments and flight. In this method, the transition Reynolds number, Re_{tr}, is correlated with the amplification factor, N, defined as

$$N = \ln\left(\frac{A}{A_0}\right). \tag{1.7}$$

Here, A is the disturbance amplitude at a given location and A_0 is the initial amplitude.

Typically, the value of N at Re_{tr} for a given geometry is determined empirically and used to predict transition in other situations. Since e^N is simply an amplitude ratio, a N does not retain any information about receptivity, its effect on the transition process, or the underlying instability mechanisms that lead to transition. As a result, the e^N method must be used with care and only when the underlying physics and transition mechanisms of a given flow are understood (Arnal, 1994; Reed *et al.*, 1996).

Two-dimensional disturbances such as Tollmien-Schlichting (T-S) waves or the Mack mode (see section 1.4) are insensitive to small surface roughness and typically remain linear for much of their growth history. The e^N method is therefore well-suited to these problems and performs very well provided that the dominant instability mechanisms and the free-stream disturbance levels are the same in each application (Arnal, 1994).

In three-dimensional flows, e^N is a poor predictor of Re_{tr} for a number of reasons. Three-dimensional waves such as stationary crossflow and Görtler vortices are extraordinarily sensitive to surface roughness, complicating comparisons between different experiments and flight. Further, these disturbance are characterized by the rapid development of nonlinear mean flow modification and saturation behavior that is not captured by linear theory. The result is that there is considerable scatter in the predicted and measured values of N for a given flow measured on different models or in different tunnels (Reed *et al.*, 1996).

However, owing to the ubiquity of this method and its historical significance, the N factor is frequently used in other contexts within the body of stability research, including in three-dimensional flows. As many boundary-layer instabilities exhibit exponential growth, N is a convenient method for reporting mode amplification relative to some computed or measured initial state.

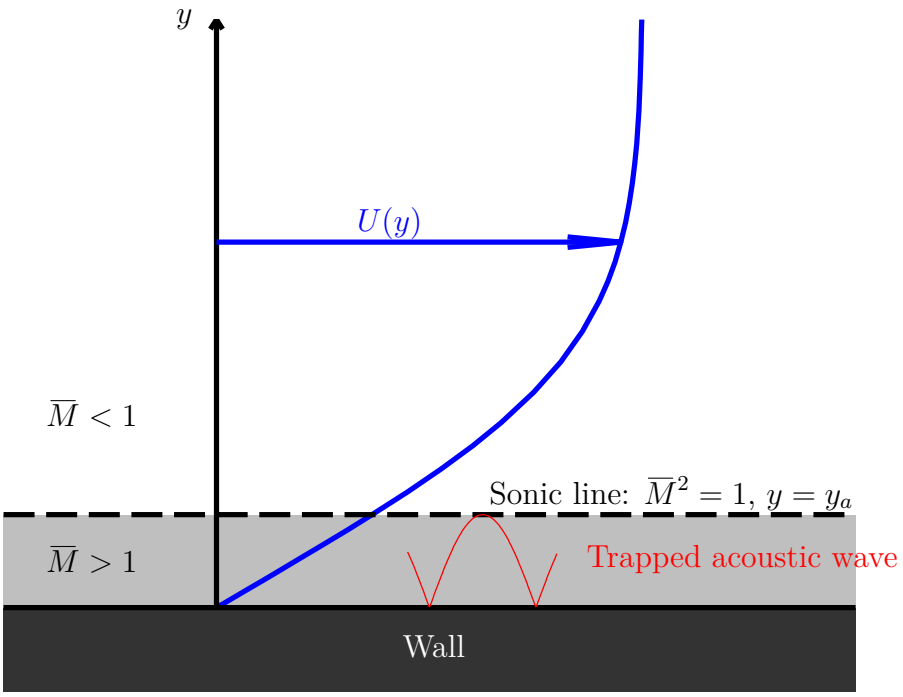

Figure 1.2: The Mack mode in a typical hypersonic, conical boundary layer.

1.4 The Mack mode

1.4.1 Instability mechanism and background

The multimodal nature of inviscid waves in hypersonic boundary layers is in stark contrast to flows of lower speed. In subsonic and low-supersonic applications, only the first mode is unstable; the others are stable and effectively decoupled from the first mode (Fedorov, 2011). The first mode includes instabilities such as the familiar T-S waves, which dominate the transition process in subsonic flows not subject to three-dimensional instabilities such as crossflow.

In hypersonic flows, the acoustic modes exist simultaneously with the first mode and represent acoustic waves in the $\overline{M}^2 > 1$ region of the boundary layer. This critical layer acts as an acoustic waveguide, trapping these waves between the sonic

line and the wall (Figure 1.2). The first of these acoustic modes is typically termed the "second-mode instability" or the "Mack mode". The "second mode" nomenclature derives from the fact that it is the second mode of inviscid instability in the boundary layer and is not a reflection of the multimodal nature of the acoustic instability. As such, the latter of the two terms, the "Mack mode," will be used henceforth to avoid confusion.

In contrast to subsonic T-S waves, which are two-dimensional and streamwise in nature, their supersonic counterparts, first-mode waves, become increasingly oblique with increasing Mach number. Up to $M_e \approx 2.2$, the first mode is the only instability present in a flat plate or cone boundary layer, at which point the Mack mode exhibits appreciable growth. At $M_e \approx 4$, the Mack mode becomes the dominant instability mechanism in the boundary layer (Mack, 1969, 1984).

Mack mode waves are two dimensional and tuned with the boundary layer thickness. The wavelength very nearly follows the relationship $\lambda \approx 2\delta$. The small wavelength combined with the large phase velocity means that these waves typically exhibit very high frequencies ranging from $O(10^5)$ Hz to $O(10^6)$ Hz in most situations, which complicates their measurement.

The Mack mode is highly sensitive to wall temperature and pressure gradient (Mack, 1984). Mack-mode waves are destabilized by an adverse pressure gradient, motivating the use of flared cone models in much of the experimental studies. The Mack mode is also destabilized substantially by wall cooling (this is opposite the behavior of the first mode). As a result, cooled models have been developed and represent a promising avenue of research.

1.4.2 Motivating studies

The Mack mode has been the subject of considerable study, both experimental and numerical. A detailed summary of Mack-mode research is given in Fedorov (2011). However, several studies in particular should be noted as motivation for the present work.

Much of the early experimental studies of Mack-mode waves can be found in experiments performed such as those by Demetriades (1974), Kendall (1975), Stetson *et al.* (1983), and Stetson & Kimmel (1992). Altogether, studies such as these made substantial progress toward our present understanding of hypersonic boundary-layer stability and the accuracy of LST toward these flows. However, in each case (and many others), these experiments have been performed in conventional hypersonic wind tunnels where free-stream disturbances are at least an order of magnitude larger than those encountered in a flight environment. While they did match up well with LST, recall from Figure 1.1 that increased free-stream disturbance levels can lead to dramatically different downstream behavior. In order to properly study the behavior of hypersonic boundary layers relevant to flight vehicles, it is therefore necessary to perform experiments in specialized low-disturbance facilities (Schneider, 2007).

Highlighting the recent computational work are a pair of studies by Sivasubramanian & Fasel (2012*a*,*b*). In these studies, a broadband wavepacket was first simulated using direct numerical simulation (DNS) showing evidence of nonlinear interaction of various streamwise and oblique modes. Following up on this, the most unstable two-dimensional wave was artificially stimulated along with the oblique wave found to be most likely to interact with the primary wave. The growth of this disturbance led ultimately to a K-type breakdown featuring Λ vortices reminiscent of the breakdown of T-S waves on an incompressible flat plate reported by Klebanoff *et al.* (1962).

Such a phenomenon, if confirmed experimentally, represents a fundamental similarity between the breakdown of high- and low-speed flows despite the substantial differences in the conditions under which these instability modes dominate.

1.5 The crossflow instability

1.5.1 Instability mechanism

The second mode is commonly the most unstable on unswept surfaces and conical geometries at zero angle of incidence. However, on other geometries common in high-speed flight (for example swept surfaces, cones at nonzero angle of incidence, or rotating axisymmetric bodies) the crossflow instability becomes occurs at lower Re and is the dominant instability mechanism in the transition process.

The crossflow instability arises in regions with a pressure gradient and curved streamlines. Using the example of a swept wing, the inviscid streamlines are curved as a result of the combined influence of sweep and the pressure gradient. The pressure gradient, being nonparallel to the streamlines, has a component normal to the inviscid streamlines which corresponds to the centripetal force for the curved streamlines. While the pressure gradient is constant throughout the boundary layer, the velocity is reduced near the wall. The pressure gradient therefore creates a nonzero stream-normal velocity component known as the crossflow component.

Figure 1.3 depicts a typical three-dimensional boundary layer subject to the crossflow instability. The crossflow boundary layer is precisely zero at the wall (no-slip) and smoothly approaches zero as z approaches infinity. It therefore necessarily features an inflection point. While the streamwise boundary layer is often inviscidly stable in low-speed flows, the inflection point in the crossflow boundary layer signals inviscid instability in the 3-D boundary layer. In high-speed flows, it provides a generalized inflectional instability in addition to that which already exists in the streamwise

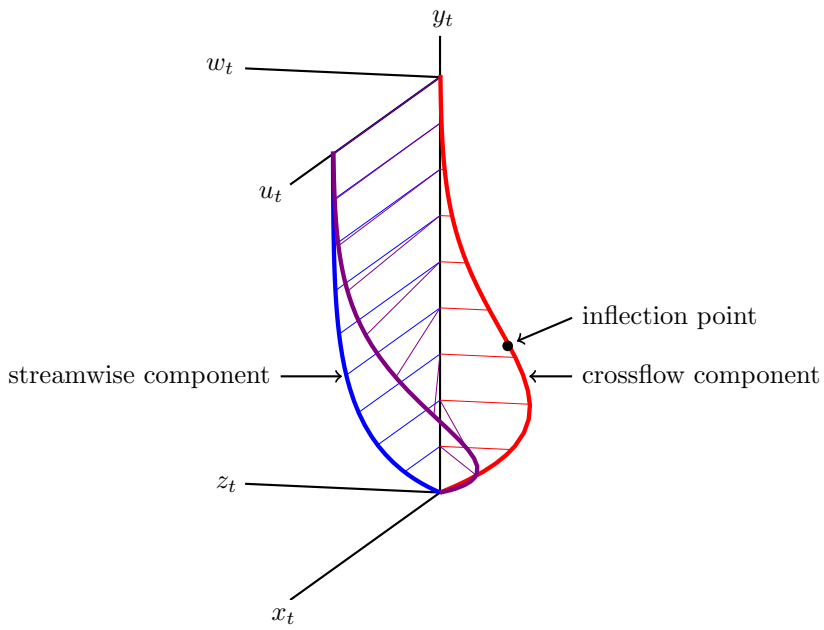

Figure 1.3: Diagram of a typical crossflow boundary-layer profile.

profile. The wavenumber vector $\vec{k}$ of the resulting crossflow waves points in the crossflow direction (z_t in Figure 1.3).

The crossflow instability in subsonic and low-supersonic flows has been the subject of considerable research since the foundational studies of Gray (1952) and Gregory *et al.* (1955). Early work focused on the boundary layer over a rotating disc, which was exactly solvable and served as a convenient canonical case for researchers at the time. A comprehensive review of the early literature can be found in Reed & Saric (1989) and of subsequent studies in Saric *et al.* (2003).

Both experiments and theory exhibit the existence and amplification of both stationary and traveling crossflow waves. Despite the existence of both modes, transition is usually dominated by one or the other rather than a combination of the two. While traveling modes are generally more unstable than are the stationary modes according to linear theory, stationary modes are often those observed causing transition

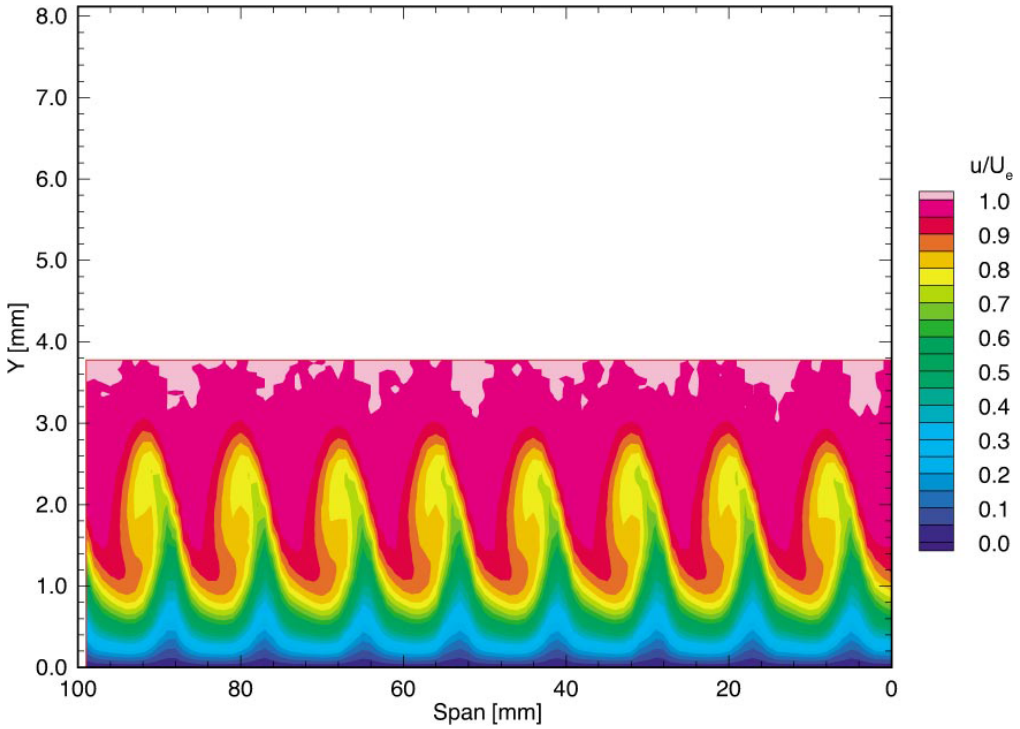

Figure 1.4: Streamwise velocity at constant-chord measured with a hot wire on a subsonic swept wing from Saric *et al.* (2003) (originally Reibert *et al.*, 1996).

in flight-like environments at subsonic and low-supersonic speeds. The reason for this lies in the receptivity process. The initial amplitudes for traveling waves are highly dependent on the free-stream turbulence levels, and the primary determining factor in whether traveling or stationary waves dominate is the level of turbulence in the test environment. Traveling waves tend to dominate in high-turbulence environments such as "noisy" wind tunnels, while stationary waves dominate in low-turbulence environments such as in flight or in low-disturbance wind tunnels (Deyhle & Bippes, 1996; Bippes, 1999).

The stationary waves manifest as approximately streamwise, corotating vortices. Since stationary crossflow modes grow relatively slowly, LST is sufficient to predict

the initial details of the instability (i.e. unstable wavenumbers). However, stationary crossflow vortices are body-fixed and nearly aligned with the inviscid streamlines; therefore, the integrated effect of the otherwise weak disturbances in v and w draw regions of the flow with $O(1)$ momentum low into the boundary layer while injecting low-momentum fluid into the upper portion boundary layer, depicted on a subsonic swept wing in Figure 1.4 from (Saric *et al.*, 2003). The figure shows a contour of streamwise velocity measured using a hot-wire probe and features the characteristic altered basic state of a crossflow-dominated boundary layer, which leads rapidly to nonlinearity and quickly invalidates linear theory (Dagenhart *et al.*, 1989*a*,*b*; Bippes & Nitschke-Kowsky, 1990; Bippes *et al.*, 1991; Deyhle *et al.*, 1993; Reibert *et al.*, 1996). For the determination of more useful statistics such as integrated mode growth, nonlinear techniques must therefore be used such as the parabolized stability equations (Herbert, 1997; Haynes & Reed, 2000).

As the nonlinear wave grows, the mean-flow distortion produced by the vortices becomes more pronounced, resulting in alternating high- and low-momentum regions in the boundary layer. As these low-momentum upwellings grow more pronounced, they begin to roll over in the upper region of the boundary layer, resulting in highly unstable boundary layers with multiple inflection points. These late-developing inflection points lead to secondary inviscid instability (Kohama *et al.*, 1991; Malik *et al.*, 1994; Wassermann & Kloker, 2002; White & Saric, 2005; Bonfigli & Kloker, 2007). It is these secondary instabilities rather than the primary wave that eventually cause the breakdown to transition.

It was predicted by Malik *et al.* (1996) and confirmed experimentally by White & Saric (2005) that two classes of secondary instability exist in the crossflow boundary layer. Type-I modes are dominated by the $\partial U/\partial z$ extrema, and type-II modes are dominated by the $\partial U/\partial y$ extrema. In most situations, the type-I secondary instability

modes have been observed first, followed rapidly by type-II modes.

1.5.2 Crossflow in compressible boundary layers

The overwhelming majority of crossflow research has been performed at subsonic and low-supersonic velocities. The underlying mechanism leading to crossflow, pressure gradient and curved streamlines, is the same across all Mach numbers. As such, crossflow waves in hypersonic flows are expected to behave qualitatively similar to their lower-speed counterparts. However, experiments in hypersonic flows dominated by crossflow instability are few and include no detailed boundary-layer experiments.

Early experiments such as those by Stetson (1982) focused on the movement of the transition front as a function of angle of attack and nose bluntness rather than the nature of the instability waves. More recently, a number of experiments have been performed in impulse facilities where run times restrict measurement techniques to surface measurements of pressure, temperature, and heat transfer (see, for example, van den Kroonenberg *et al.*, 2010; Swanson & Schneider, 2010; Muñoz *et al.*, 2014; Ward, 2014).

Experiments by Schuele *et al.* (2013) were performed in a Mach 3.5 blowdown facility on a yawed cone boundary layer using point measurements. However, the goal of this study was to test the extension of the use discrete roughness elements (DREs) for flow control, first pioneered by Saric *et al.* (1998), to a high-speed boundary layer. Further, The Pitot measurements performed were of limited bandwidth and were unable to resolve the secondary instability.

While experiments have not yet explored the structure and breakdown of hypersonic crossflow waves, several computational studies have been performed on this topic on cones at angle of attack. Balakumar & Owens (2010) performed a DNS on a cone with both a smooth tip and two patterns of DREs. Kuehl *et al.* (2012)

and Perez *et al.* (2013) have performed PSE calculations, both linear (LPSE) and nonlinear (NPSE) using a new code on the same geometry as Balakumar & Owens (2010) with the smooth tip. These PSE computations have shown good agreement with the DNS. Gronvall *et al.* (2012) performed a DNS on the same geometry with distributed roughness placed at the tip.

The surface methods popular in the above experiments have compared well with the above computations. However, no suitable experiment yet exists for comparison with the more detailed aspects of the boundary layer predicted by computations. Further, the hallmark features of low-speed crossflow such as stationary mode saturation, the development of secondary instability, and the ultimate breakdown mechanism(s) have yet to be confirmed experimentally in hypersonic flows.

1.6 Experimental objectives

1.6.1 Three-dimensional probe traverse

The planned experiments in M6QT are to be three-dimensional. As such, the first objective and key enabling technology for these studies is the development of a new probe traversing mechanism. This mechanism should work on axisymmetric models with either straight-walled or flared geometry.

1.6.2 The second mode

Previous experiments by Hofferth (2013) have documented the early growth and onset of nonlinear behavior in the second-mode-dominated boundary layer over a flared cone. Further, computations by Sivasubramanian & Fasel (2012*a*,*b*) and Reed (private communication) have indicated that the ultimate breakdown mechanism may be fundamentally similar to that of Tollmien-Schlichting waves on the low-speed flat plate. One objective of this study is therefore to promote the breakdown of second-mode waves and explore the characteristics of this breakdown.

1.6.3 High-speed crossflow

The crossflow instability is expected to be dominant on a wide class of common geometries on hypersonic vehicles. Despite this, it has been studied only lightly under such conditions and no detailed boundary-layer measurements exist. The resulting uncertainty surrounding the crossflow instability in the hypersonic regime partially motivated the nearly 2-D design of the X-43A. The final objective of this study is therefore to perform the first such boundary-layer experiments on hypersonic crossflow with the goal of providing data at the level of detail applied to low-speed flows. Questions of particular interest include:

- Do stationary waves still dominate in low-noise environments?
- Do stationary and traveling waves coexist?
- Do stationary waves exhibit saturation, and if so, at what amplitude?
- At what point does secondary instability occur and which type develops first? Do they lead rapidly to breakdown?
- Do frequency scaling rules from low-speed flows extend to the hypersonic regime?

2. EXPERIMENTAL SETUP & TECHNIQUES

2.1 The Mach 6 Quiet Tunnel Facility

2.1.1 Tunnel history

The Mach 6 Quiet Tunnel (M6QT) is a hypersonic, low-disturbance wind tunnel facility at Texas A&M University (TAMU) that traces its roots to the Advanced Mach 6 Pilot Quiet Tunnel in the Nozzle Test Chamber (M6NTC) developed at the NASA Langley Research Center (LaRC). The culmination of a 25-year research program spanning the 1970's, 80's and 90's, the M6NTC was designed to maximize the extent of the laminar boundary layer on the nozzle walls, allowing detailed stability experiments to be performed in an environment approaching that of flight. This goal was achieved using several techniques (Blanchard *et al.*, 1997; Chen *et al.*, 1993), including

- a series of meshes and screens installed in the upstream half of the settling chamber to dampen upstream tunnel noise;
- a suction slot just upstream of the throat;
- a slow-expansion nozzle design; and
- a highly-polished nozzle surface.

Extensive flow-quality characterization in the LaRC facility was performed by Blanchard *et al.* (1997), which showed that the RMS fluctuations in the uncalibrated hot-wire signal taken in the tunnel free stream remained under 0.08% across the entire useful range of the tunnel, defined as between $Re/L = 5.74 \times 10^6$ m^{-1} and $Re/L = 10.04 \times 10^6$ m^{-1}.

Following these experiments, the nozzle was placed in storage until transferred to TAMU in 2005. These components then underwent a major refurbishment and integration effort in order to reestablish the facility at the National Aerothermochemistry Laboratory (NAL) at Texas A&M University as part of the National Center for Hypersonic Laminar-Turbulent Transition Research program.

2.1.2 Re-establishment and flow quality

A substantial effort was required to reestablish M6QT. While the nozzle and settling chamber were transferred from NASA, all other infrastructure—including the test section; high pressure air and vacuum systems; heating and filtering systems; and data acquisition systems—required either substantial modification or complete re-design and fabrication. Initial flow quality tests (Hofferth *et al.*, 2010) showed a level of performance consistent with Blanchard *et al.* (1997). These measurements indicated that the free-stream total pressure fluctuations over the majority of the quiet region are no greater than 0.05% in the present experiment, which represents the noise floor of the instrumentation. In 2010, the nozzle was repolished, maintaining the performance levels previously achieved and greatly increasing the reliability of the facility by reducing the frequency of required cleaning. An extensive discussion of the reestablishment effort can be found in Hofferth (2013).

2.1.3 Tunnel design

M6QT operates as a pressure-vacuum blowdown facility within the infrastructure at NAL. Figure 2.1 depicts the indoor tunnel flow path including the settling chamber (§ 2.1.3.1), nozzle (§ 2.1.3.2), test section (§ 2.1.3.3), and diffuser. Pressure and vacuum are supplied by way of a high-pressure air system a two-stage ejector system (§ 2.1.4).

In hypersonic wind tunnels, vorticity disturbances are generally minimal as a

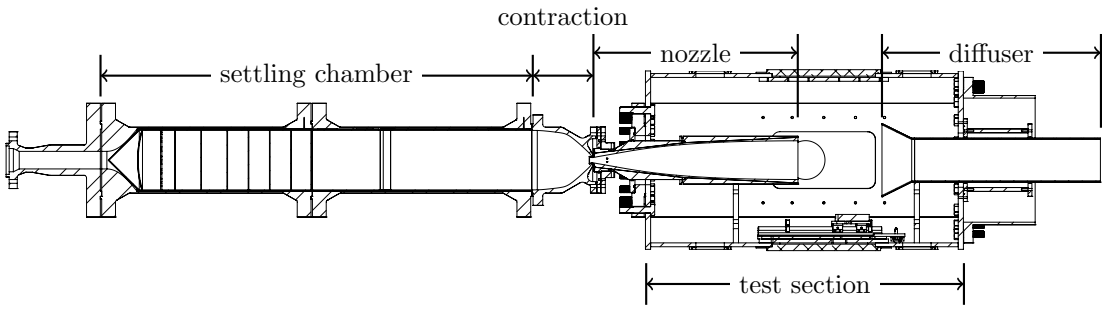

Figure 2.1: Cutaway of M6QT components.

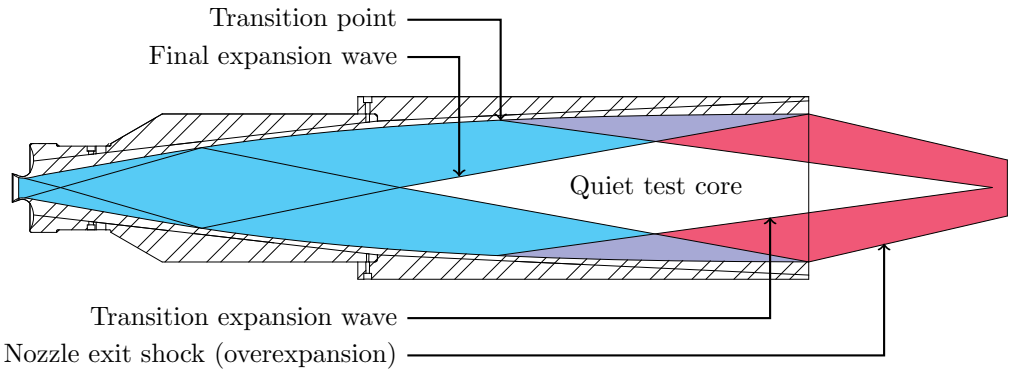

Figure 2.2: M6QT nozzle annotated with the quiet test core (QTC) and associated features.

result of the significant expansion required to generate a hypersonic flow. The primary source of free-stream noise is acoustic waves radiating along Mach lines from the turbulent nozzle-wall boundary layer where the turbulent structures appear to the free stream as a rough wall. The problem of designing a hypersonic, low-disturbance wind tunnel is therefore one of maximizing the region of laminar flow on the nozzle wall. The quiet region of the flow is created when the Mach lines emanating from the transitional region of the nozzle-wall boundary layer meet at the nozzle centerline significantly downstream of the onset of uniform flow in the nozzle, resulting in a biconic region of quiet flow called the quiet test core (QTC, Figure 2.2).

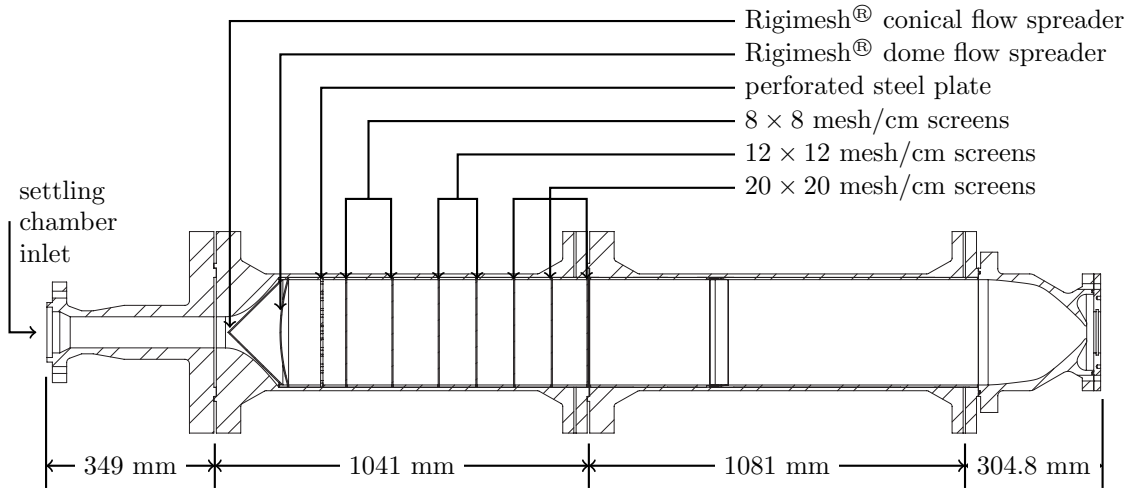

Figure 2.3: M6QT settling chamber and contraction, annotated with internal features.

The following sections detail the layout of the tunnel and how they pertain to the creation of the QTC.

2.1.3.1 Settling chamber

The M6QT settling chamber (Figure 2.3) is separated into two sections. The first section, approximately 1 m in length, contains a series of flow conditioning features, including a conical Rigimesh® flow spreader and a dome Rigimesh® flow spreader to encourage uniform flow entering the settling chamber, followed by a perforated steel plate and mesh screens of increasing mesh density to remove acoustic and turbulent fluctuations resulting from the upstream air flow path. The second section is empty and extends up to the contraction. These features provide a low-noise environment up to and entering the nozzle contraction and are the first step in generating a low-disturbance flow.

The entire settling chamber is heated externally by 8 kW of Ogden Mighty-Tuff electrical resistance heaters in order to maintain the settling chamber temperature at

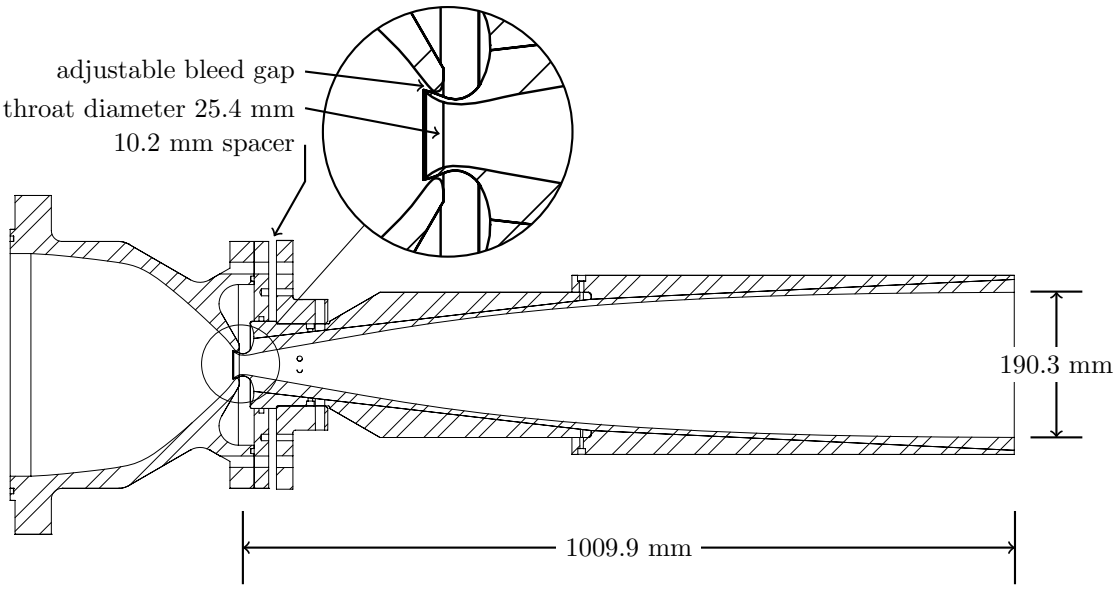

Figure 2.4: M6QT nozzle dimensions and detail. Inset is a close-up of the throat and bleed gap.

430 K and reduce convective preheating times.

2.1.3.2 Nozzle

The remaining three features pertinent to the QTC are part of the contraction and nozzle sections of the tunnel (Figure 2.4). While the flow quality features in the settling chamber help maintain a low-disturbance free-stream, minimizing the initial amplitudes generated by the receptivity process at the throat, the existing turbulent boundary layer in the settling chamber still contaminate the nozzle wall boundary layers in a conventional tunnel. In order to prevent this, M6QT includes a suction slot just upstream of the throat formed by the protrusion of the nozzle throat slightly into the contraction (Figure 2.4 inset). The bleed slot is connected to the vacuum in the diffuser and the turbulent boundary layer is sucked out of the tunnel prior to the throat, allowing a new, laminar boundary layer to form just upstream of

the throat. The low-disturbance free stream in the settling chamber combined with a highly polished nozzle surface minimizes the receptivity process in the incipient nozzle boundary layer.

Supersonic nozzles necessarily feature highly concave surfaces, and the transition process is therefore dominated by the Görtler instability. While the concave curvature cannot be avoided, the growth of the instability can be delayed by incorporating a long-expansion design. To this end the M6QT nozzle is substantially longer than a typical supersonic nozzle of the same Mach number, featuring an extended straight-wall section and pushing the onset of the concave surface farther downstream. This approach delays the growth of Görtler vortices and, therefore, the onset of turbulence in the boundary layer (Chen *et al.*, 1993).

2.1.3.3 Test section

The M6QT is configured as a free jet wind tunnel featuring a sizable test section and less-intrusive probing mechanisms (Figure 2.1). The four long sides of this test section include modular access panels that can be used to support a variety of instrumentation and model configurations. In a typical configuration, the two side walls are outfitted with quick-release doors with optical access, the bottom panel is fitted with the model-mounting system and traverse mounting hardware and the top panel is simply closed. Other configurations have included a ceiling-mounted traverse and probe supports attached to the walls. Windows are available for both the visible and infrared portion of the spectrum depending on the application.

2.1.4 Infrastructure

The M6QT facility as is installed at the TAMU National Aerothermochemistry Laboratory (TAMUNAL) where it shares pressure-vacuum infrastructure with several

additional supersonic and hypersonic facilities. High pressure air is provided by a pair of CompAir 5442, each with a pumping capacity of 3.68 m^3/min. (130 SCFM) at 20.68 MPa (3000 psig). The compressed air is filtered with a pair of 99% efficient sub-micron particle filters and dried to a dew point of $\leq -40°C$ by a twin-tower desiccant drier before being stored in an 23.2 m^3 (820 ft^3) tank at 17.24 MPa (2500 psig).

The vacuum for the pressure-vacuum tunnels is generated using a two-stage Venturi air ejector. This system uses approximately 20 kg/s of compressed air at 1033 kPa while in operation and is capable of supplying a back pressure of as low as approximately 500 Pa to the wind tunnels. This high mass-flow requirement is the dominant factor in determining the tunnel run time.

The same compressed air reservoir supplies air for the tunnels. Prior to reaching the settling chamber, the air is heated by a 500 kW Chromalox electrical-resistance heater to achieve the desired total temperature (maximum 533 K) and re-filtered using 1-μm particle filter immediately prior to entering the tunnel. While in operation, the M6QT draws approximately 1 kg/s of compressed air through the test section. The air requirements of the ejector and nozzle combined result in a maximum run time of approximately 50 seconds.

The M6QT shares this infrastructure with the Adaptively-Controlled Expansion (ACE) tunnel (Semper *et al.*, 2009) in a parallel installation. In order for each tunnel to run separately from one another and while work continues in the other facility, they must each be capable of being isolated from the flow path when not in use. Each tunnel is thus isolated from the high-pressure air using a ball valve just downstream of the final particle filter and from the ejector system using a pneumatic knife gate valve just downstream of the diffuser.

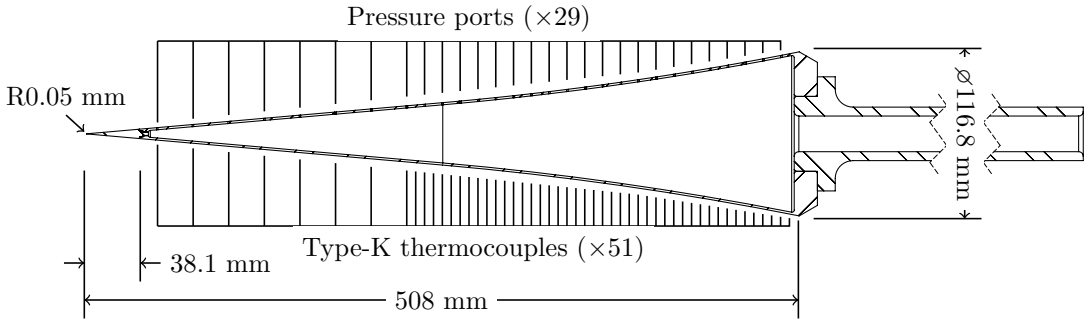

Figure 2.5: Diagram of the LaRC 93-10 flared cone. The first 8 pressure ports have an axial spacing of 25.4 mm on the forebody before transitioning to a 12.7 mm spacing. The first 8 thermocouples have the same spacing before transitioning to a 6.35 mm spacing.

2.2 Test models

The present experiments were performed using two wind tunnel models. The first, the NASA Langley 93-10 flared cone, was brought to Texas A&M along with the M6QT (§ 2.2.1). The second of these models, the TAMU 7DC, was recently designed at Texas A&M (§ 2.2.2). Each of these models has multiple roughness configurations including a smooth surface and roughness either in the form of azimuthally-periodic discrete roughness elements (DRE) or distributed roughness (§ 2.2.3).

2.2.1 Flared cone

The NASA Langley 93-10 flared cone (Figure 2.5) is the same model used in Lachowicz & Chokani (1996), Doggett & Wilkinson (1997), Horvath *et al.* (2002), and Hofferth (2013). Its profile consists of a right-circular cone with a 5° semi-vertex angle for the first 254 mm (10 in) of axial length at which point a flare with a constant radius of 2.36 m (93.071 in) begins and continues for an additional 254 mm (axially) to a total axial length of 508 mm (20 in). While tangency is maintained in the transition to the flare, radius of curvature is discontinuous. The adverse pressure

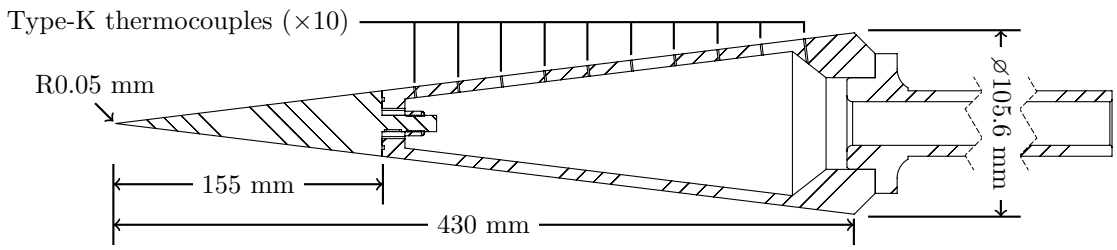

Figure 2.6: Diagram of the TAMU 7DC right-circular cone.

gradient introduced by the flare promotes the growth of the second-mode waves, producing larger second-mode N-factors than on a 5° right-circular cone of equivalent length.

The model model is constructed of thin-walled stainless steel with a nominal thickness of 1.8 mm. The model includes removable tips comprising the first 38 mm of its length. While a variety of blunt tips are available, tip bluntness is known to stabilize a boundary layer and a sharp tip was used for the present study. The sharp tip has a specified tip radius of 2.54 µm.

The model is instrumented with both a series of pressure ports and type-K thermocouples along two rays separated by 180° of azimuth. Along one ray is a series of 29 pressure ports (21 of which are in the flared section) of 1 mm diameter. These ports are unused in the present study as the length of tubing required gives insufficient frequency response. Along the opposing ray are 51 thermocouples (43 along the flare) welded to the interior wall so as not to introduce roughness to the surface. The wall thickness at the thermocouple locations is 0.8 mm. The thermocouples are sampled once at each measurement location in order to monitor the wall temperature during each run.

2.2.2 Straight cone

The sharp-tipped, 7° right-circular cone has been adopted as the canonical geometry for high-speed crossflow studies and was therefore chosen for the present study. The Texas A&M 7-degree Cone (TAMU 7DC) was designed in house out of 17-4 PH stainless steel and has a total length of 430 mm (16.92 in.) from the sharp tip to the base. The model was designed as a two-piece model including a detachable tip comprising the first 155 mm (6.10 in.) and a conic frustum for the remainder of the length (Figure 2.6).

The large size of the removable tip offers several advantages over the more traditional small tips such as those on the LaRC 93-10 flared cone:

- The downstream axial location of the interface is further removed from the receptivity region of the model, minimizing the potential adverse effects of the interface on the stability of the boundary layer.

- The larger volume of the tip facilitates the future design of tips instrumented with active elements such as plasma actuators or suction/blowing slots in addition to the more standard tip bluntness or external roughness.

- The large-diameter threaded post can be keyed to fix its orientation and is large enough to be held in place easily from the inside using a nut rather than relying solely on threads in the tip of the frustum.

The interface between the tip and the frustum includes an O-ring to prevent any leakage flow as a result of any pressure difference between the inside of the cone and the free stream.

The frustum is a hollow, thick-walled model and is instrumented with 10 type-K thermocouples along its length spaced at 25.4 mm along the surface of the frustum.

While the thin-walled LaRC 93-10 typically reaches its adiabatic condition rather quickly, the TAMU 7DC, owing to its much larger thermal mass, does not. To combat this effect, the cone can be fitted with an internal heating system to bring its temperature to it's adiabatic wall temperature and allowing the model to be held at a constant temperature during a run. In order to monitor the wall temperature during a run, the output from the thermocouples is averaged and provided to the PID process controller operating the model heaters.

2.2.3 Roughness configurations

2.2.3.1 Discrete roughness elements

Artificial roughness was created using high-temperature vinyl water slide decals. These decals involve screen-printing a UV-cured vinyl onto a dextrose backing and can be made in nearly any shape. The minimum decal thickness is approximately 3 μm and the maximum thickness used in the present work is approximately 20 μm, though decals upward of 200 μm are theoretically possible. These decals are wetted and placed on the surface of the model, at which point they can be easily slid into place and manipulated without the risk of damaging the elements. They are then allowed to dry overnight. The resulting decal roughness elements are durable and the surface may easily be cleaned by wiping with a damp towel or the elements may be removed with acetone.

2.2.3.2 Distributed roughness

Distributed roughness was created by combining 36-grit aluminum oxide abrasive blasting media with Duralco 4525 high-temperature epoxy. The resulting composite material adheres readily to metallic surfaces and is resistant to running on both

vertical and inverted surfaces, which are important qualities for application to the surface of the cone. The applied mixture can be spread on a surface in a layer that averages approximately 500 μm in thickness. Therefore, a depression of this depth was machined into the cone surface prior to application of the rough composite in order that the average height of the rough surface was approximately equal with the cone surface.

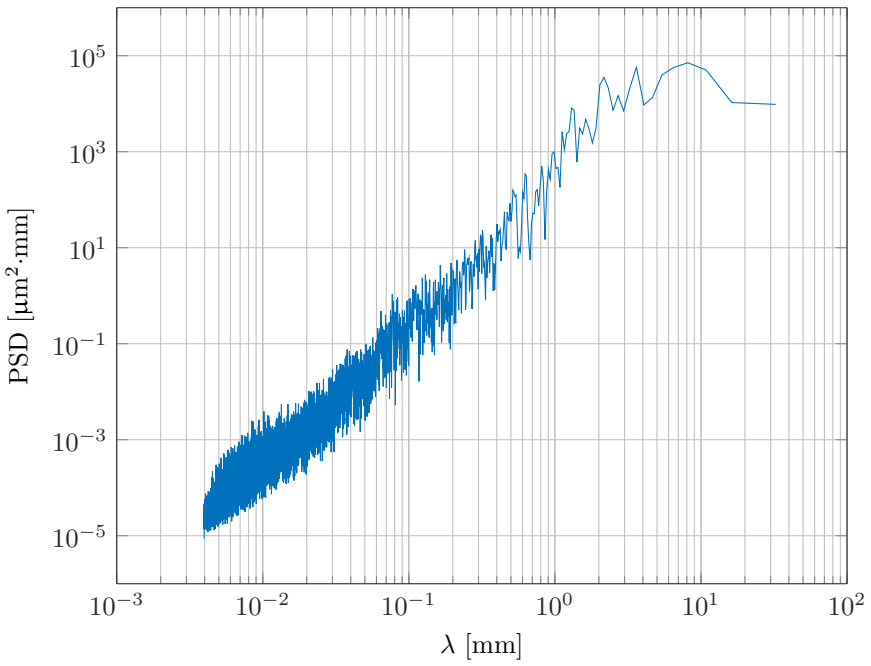

Figure 2.7: A typical power spectrum across the composite distributed roughness.

The final surface roughness can be controlled by adjusting the grit size and grit-to-epoxy ration. In the present case, the rms roughness was measured to be approximately $R_q \approx 150$ μm. The power spectral density of the roughness indicates that energy is concentrated largely in wavelengths $\lambda > 0.5$ mm with a roughly uniform, monomial decrease in power toward shorter wavelengths (Figure 2.7). The most

amplified azimuthal wavelength in the present experiments is expected to be $m = 50$, which, in the region of roughness, translates to approximately 0.5 mm $\leq \lambda \leq$ 1.5 mm.

2.3 Traversing system

2.3.1 Design considerations

All previous experiments performed in M6QT at Texas A&M utilized a two-axis probe traversing mechanism. These previous experiments focused exclusively on two-dimensional waves or free-stream measurements and were adeptly handled by the two-axis system. However, the limitations of this system prevented the study of three-dimensional phenomena. It was limited to wall-normal (or axis-normal) boundary-layer profiles along a given ray of a cone. For this reason, the development of a three-axis traversing mechanism was a key challenge in enabling the study of three-dimensional phenomena.

There were several parameters about which this new design was based. It must have three axes of motion, it must support axisymmetric models, it must support both flared cones and standard cones, and it must be able to function on models placed at nonzero angle of incidence to the flow.

While the requirement of three axes was obvious, the choice of coordinate system was not. The cheapest option would be to simply add a third z axis to the existing x-y traverse used in previous studies. Such a Cartesian system would be capable of measurements on a full half of an axisymmetric model, but would require a means of rotating the hot-wire probe to remain parallel to the surface and complicated adjustments to the probe to support nonzero angle of incidence. Given that all future plans involve axisymmetric models, a more natural choice of coordinate systems is cylindrical coordinates. Further, making the coordinate system co-axial with the model ensures that the system supports the angle of incidence requirement by default.

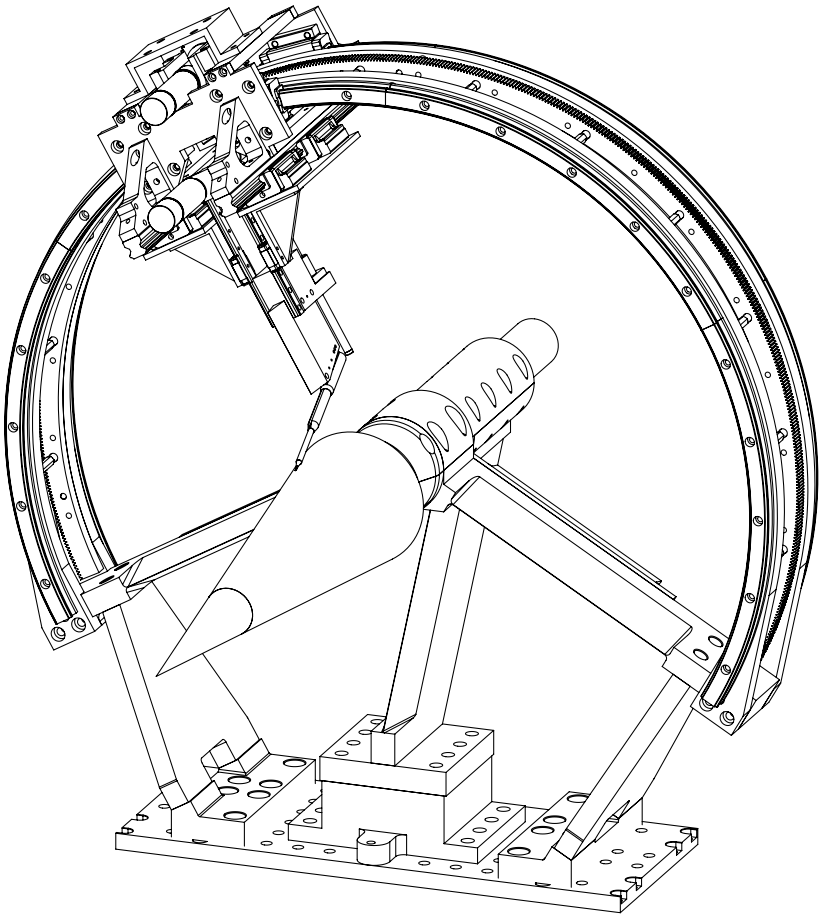

Figure 2.8: Three-dimensional traversing mechanism affixed to 7° cone model.

Several such traversing mechanisms have been designed and used in related studies at facility such as NASA Langley and Notre Dame (Corke *et al.*, 2002; Schuele *et al.*, 2013), which are fixed to the cone shaft and slide along the cone body. These systems, however, are unsuitable for use with flared cone models and their use as a template is limited. Instead, the final design features a two-axis "z-r" (axial-radial) traverse mounted to a carriage that moves around the model in the θ-direction (azimuth) using a rack and pinion gear system (Figure 2.8).

2.3.2 Design details

2.3.2.1 Ring structure

Figure 2.9 and Figure 2.10 depict the traverse with the carriage removed from the front and side respectively. The θ motion was constrained using a pair of THK HCR15-series motion guide systems. Each rail consists of 4 segments, each spanning 60°, whose ends are ground to match and provide a seamless transition from one to the next. Each of these tracks was affixed to a 17-4 PH stainless steel structural arc with outer diameter 620 mm. These rings are affixed to the two "wing" structures extending from the cone axis such that the tracks face opposing directions. The rings are held rigid at a constant separation using a series of adjustable, threaded tie rods.

The wing supports connect to the support arcs and the model mounting system. As they are one of only two portions of the device to be exposed to the flow, they feature a 12° half-angle wedge cut into their upstream side and a 20° half-angle wedge affixed to the downstream side. The wings are supported near their ends with steel plates that connect them rigidly with the floor of the mounting system.

The aft support arc also supports the rack gear. The module 0.8 gear has a pitch diameter of 612 mm and the full ring included 765 teeth with a 20° pressure angle. It was initially machined as a disc, at which point the center was machined out to form a ring, and a 120° arc was removed to match the inside of the support arc. The matching pinion gear is affixed to the carriage and used to control the azimuthal motion (Figure 2.11).

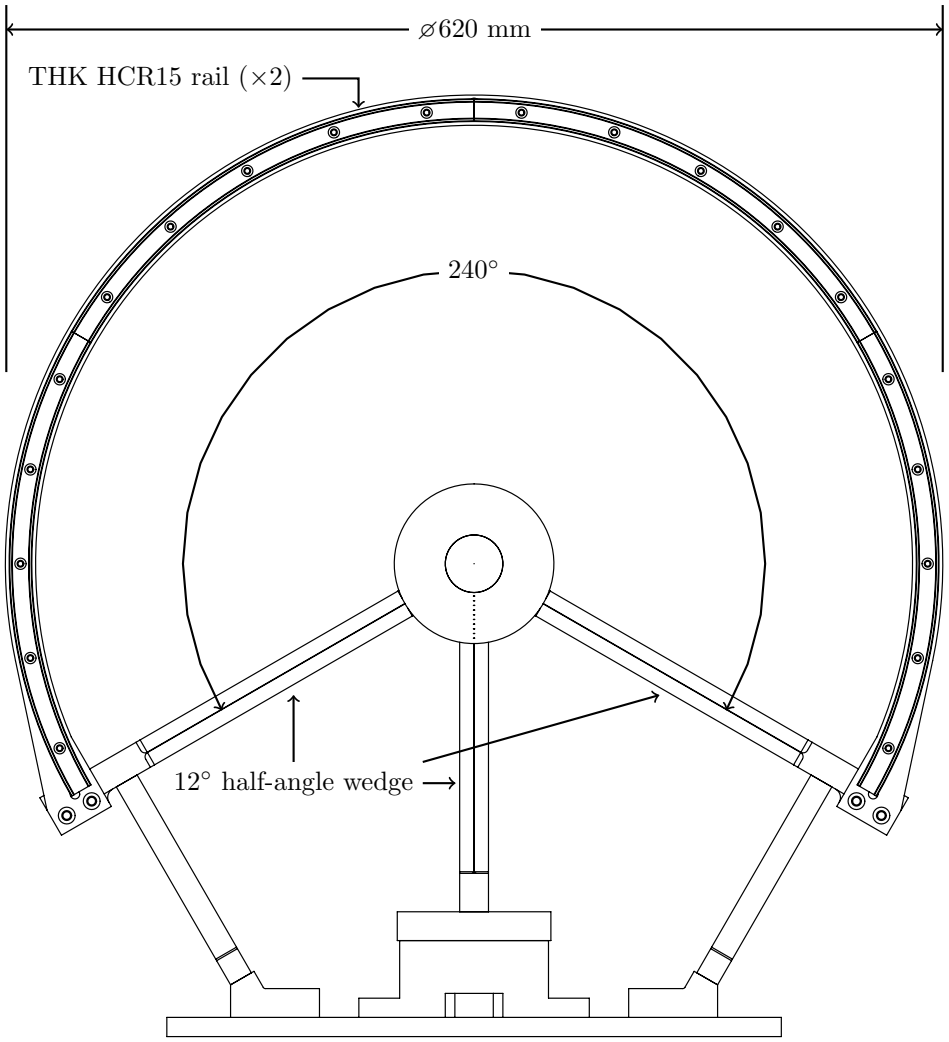

Figure 2.9: Cylindrical traverse system with the carriage removed (front view).

2.3.2.2 Carriage and motion stages

The carriage system (pictured in Figure 2.12), houses all three motors and the motion guides for the r- and z-axes. The carriage was constructed of many individual pieces, many of them designed to be rapidly cut from a single plate of steel on a wire EDM machine. This approach lends a great deal of modularity to many of the components, facilitating any future modification.

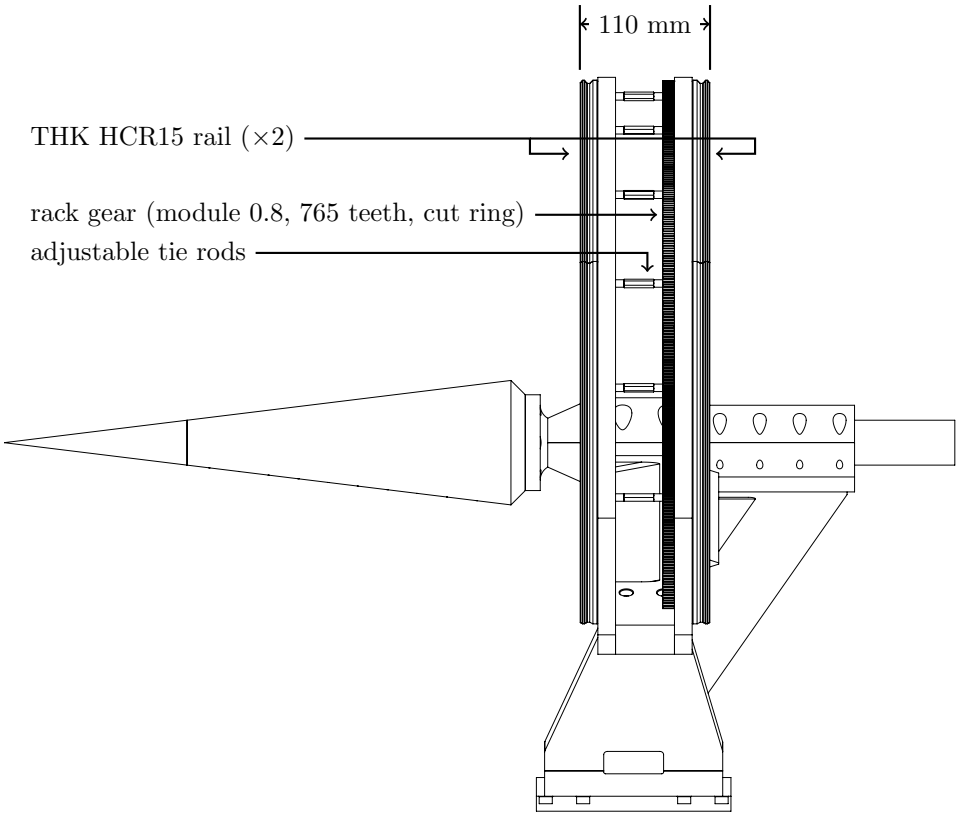

Figure 2.10: Cylindrical traverse system with the carriage removed (side view).

Each axis utilizes a Faulhaber brushless DC servomotor with a built-in absolute encoder for its motion. The radial stage (r) uses a Faulhaber 2232S024BX4 AES-4096 motor while the azimuthal (θ) and axial (z) stages each use a Faulhaber 2250S024BX4 AES-4096 motor. The r and z stages each have a ball screw with 1 mm lead coupled to their motors for a movement resolution of 244 nm per encoder line at an accuracy of ± 5 lines. The θ stage features a roughly 246:1 planetary gearhead to provide substantial torque on the pinion gear, resulting in a movement resolution of $3^\circ \times 10^{-5}$ per encoder line and a ± 10 line accuracy. The accuracy windows are adjustable within the Faulhaber MCBL 3006 S AES RS controllers, however these values represent the maximum degree of accuracy while still ensuring stable operation. These target

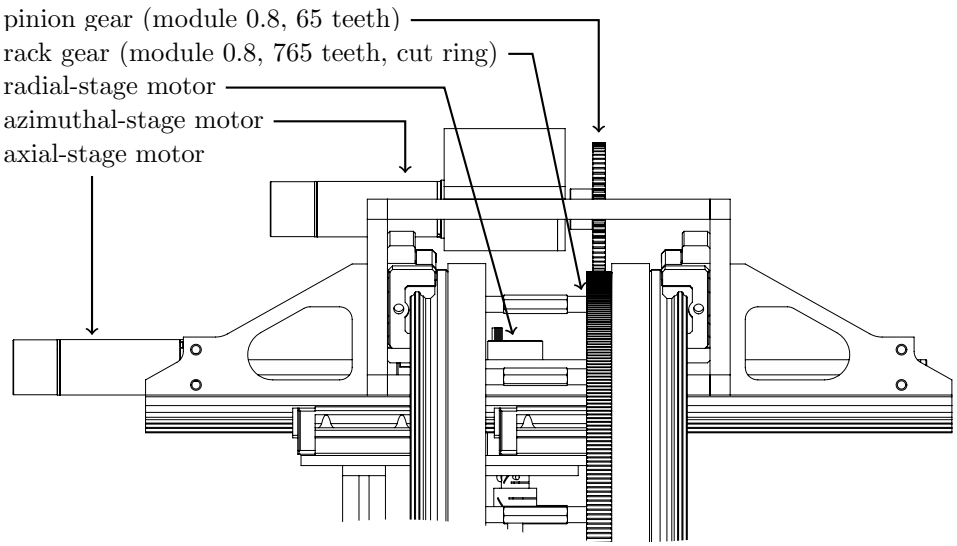

Figure 2.11: Close-up view of the carriage and ring assembly and gear orientation.

Axis	Range	Min. step	Accuracy
r	100 mm (max.)	2.5 μm	±1.22 μm
θ	220°	$3° \times 10^{-4}$	$\pm 3° \times 10^{-4}$
z	130 mm	2.5 μm	±1.22 μm

Table 2.1: Motion specification and details for the azimuthal traversing system

windows also determine the minimum step size. The specifications for this system are summarized in Table 2.1.

Figure 2.13 and Figure 2.14 depict the carrage from the front and side respectively. The azimuthal motor and pinion gear are attached to the top of the traverse using a set of adjustable screws and springs in order to provide adjustable contact force against the rack. Proper contact minimizes gear backlash and is checked prior to each wind tunnel run. The THK HCR15-series motion carriages affix to the inner sides of the two wall plates and the remainder of the interior space is used to provide room for the radial motor as it moves axially.

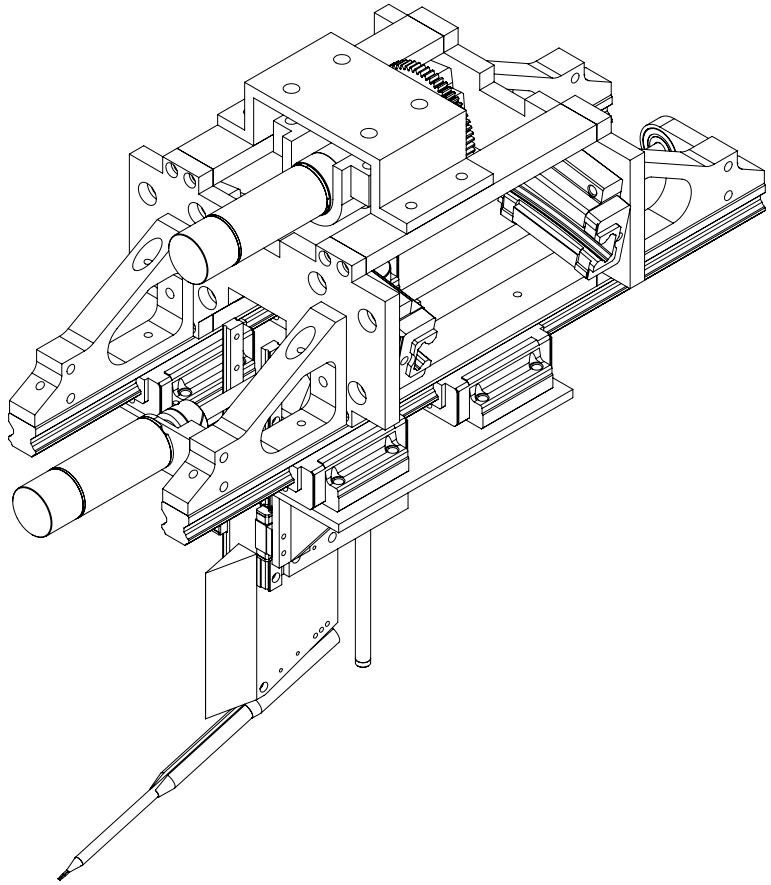

Figure 2.12: Isometric view of the carriage housing the motion stages.

The underside of the carriage includes a pair of THK HSR15-series linear motion guides, each with a pair of motion carriages to provide axial motion of the probe. A steel plate is mounted to the carriages. The radial stage is guided by a pair of THK RSR7 linear motion guides mounted to this plate along with the radial motor and ball screw.

The radial stage consists of several components. The first is a mounting block that attaches directly to the motion guides and ball screw and includes a channel used to mount the portion of the probe arm that will be exposed to the free stream. The system is designed to accommodate any number of probe designs so long as the

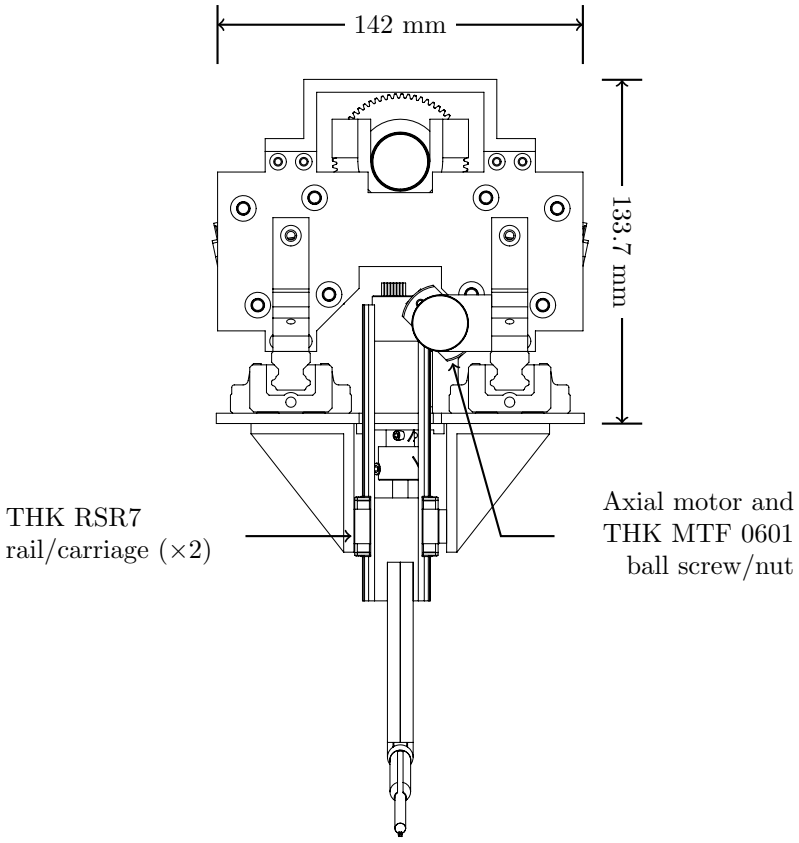

Figure 2.13: Traverse carriage and radial arm (front view).

upper portion matches the two holes in the mounting block. Two set screws on either side of this channel hold the probe arm in place.

The probe arm is exposed to the flow and features two parts: a wedged body and an adjustable probe holder. The probe holder fits into a groove on the bottom of the arm and pivots around a large screw just aft of the wedge. The holder includes a series of holes that line up with corresponding holes in the probe arm through which small screws can be inserted to set a probe angle. The holder is once again held in place rigidly by two set screws on either side. The probe holder can support any number of probe types, including hot-wire or Pitot probes as long as their shape is such that an adapter can be built to fit the circular mount.

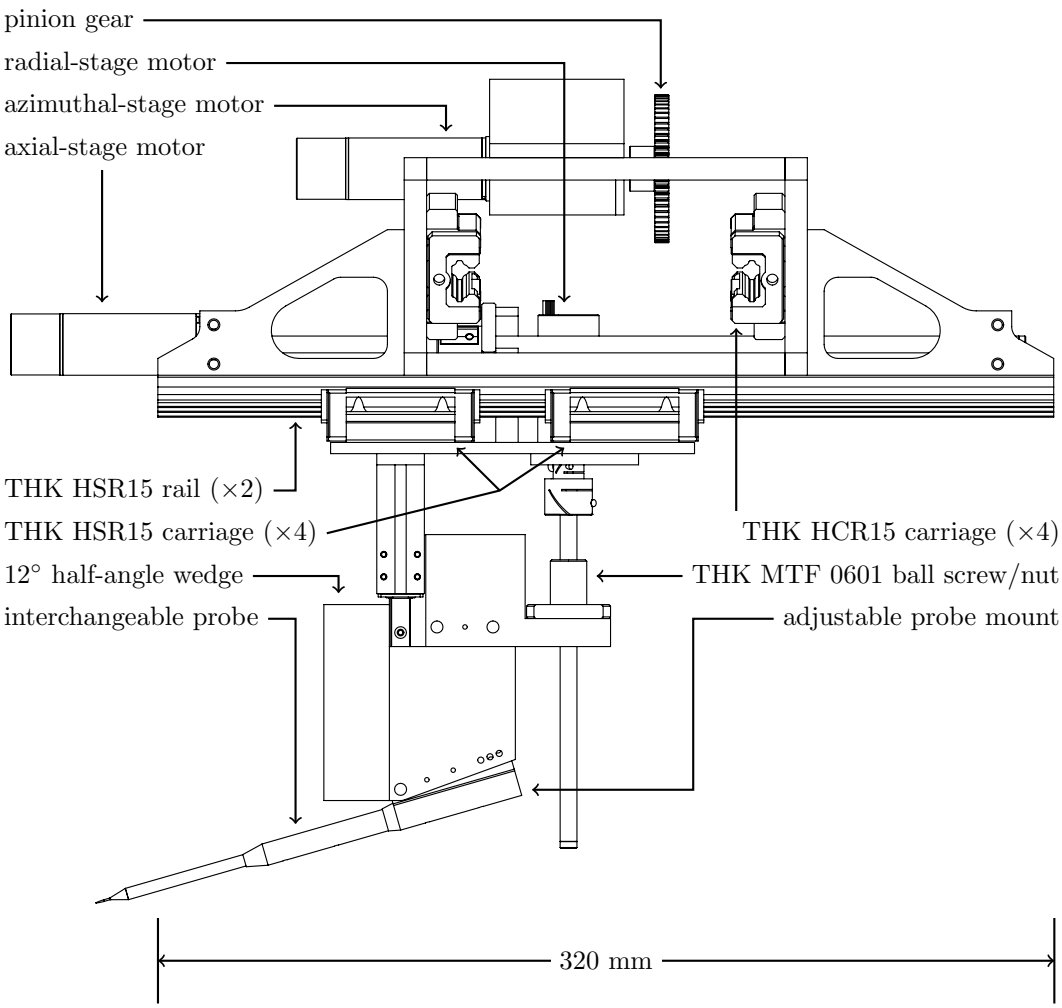

Figure 2.14: Traverse carriage and radial arm (side view).

The system is controlled by three Faulhaber MCBL 3006 S AES RS motor controllers installed in a custom 24 VDC control cabinet with a linear power supply to eliminate the electronic noise inherent in switching power supplies. The controllers are operated from a purpose-built LabVIEW VI with GUI control panel that handles all motion control and data acquisition functions (§ 2.4).

2.4 Instrumentation and data acquisition system

Data acquisition (DAQ) is performed using two separate DAQ computers equipped with National Instruments (NI) hardware and software. DAQ processes are coordinated using custom-designed LabVIEW VIs.

One of these systems, "NALDAQ", handles nearly all DAQ operations for general tunnel operating parameters for both hypersonic facilities installed at the lab including M6QT. The measured quantities handled by NALDAQ include temperatures and pressures at various stages along the ejector and tunnel air supply systems and the pressures at various stages along the tunnel flow path such as settling chamber temperature and pressure, test section pressure and diffuser pressure as well as M6QT bleed valve position and a host of other quantities. These quantities are sampled using an NI USB-6255 M Series 16-bit multiplexing DAQ board with 40 differential input channels at 1 kHz. These data are then averaged to 10 Hz and saved in a spreadsheet for each run cataloging ejector and tunnel performance. This system also displays the same data in a realtime monitoring mode when not acquiring and handles data for compressor status and storage tank pressure and is programmed to alert tunnel operators via SMS to changes in status of the high-pressure air system such as a full tank or compressor warnings and faults.

Pressures and temperatures handled by NALDAQ that are not critical to M6QT experimental analysis are measured using generic pressure and temperature sensors, typically Omega-brand pressure transducers and type-K thermocouples. Tunnel-critical pressures are handled with more sophisticated equipment. The settling chamber pressure is measured with an MKS Batatron 615A High-Accuracy Capacitance Manometer with a 10,000 torr full range and an MKS 670B signal conditioner. This system is temperature compensated and is quoted to be accurate to $\pm 0.2\%$ of

the measured reading. Test section and diffuser pressures are handled by MKS 902 Piezo Vacuum Transducers with 1,000 torr range accurate to 1% of the reading.

The second system, "M6QTDAQ", handles DAQ operations in M6QT for specialized experimental data such as hot-wire measurements, cone-surface temperature measurements, schlieren photodiode data, and more. These functions are integrated into the same LabVIEW VI that handles motion control of the cylindrical traverse (§ 2.3). Each run typically samples data of two varieties: high-bandwidth, or "fast" channels; and low-bandwidth, or "slow" channels. For each point in the measurement profile, slow channels are sampled once and fast channels are sampled at a specified sampling frequency and time, (typically $f_s = 1$ MHz and $t_s = 100$ ms for hot-wire anemometry). Slow channels typically include the settling chamber total pressure and temperature and the wall temperature of the test article, while fast channels are generally various channels associated with the boundary-layer instability measurements.

Pressures and temperatures sampled on slow channels are measured using the aforementioned transducers and their associated signal conditioners. Additional slow channels are provided by a modular NI SCXI-1001 DAQ chassis. For the present experiment, this chassis was outfitted with several NI SCXI-1102 32-channel thermocouple amplifiers outfitted with NI SCXI-1303 32-channel isothermal terminal blocks for acquisition of model thermocouple data. Fast channels are sampled using an NI USB-6366 X-Series DAQ board offering 8 channels of simultaneous sampling up to 2 MHz per channel.

2.5 Measurement techniques

The present studies were performed largely using three measurement techniques. Constant-temperature hot-wire anemometry (§ 2.5.1) was used for point-wise bound-

ary layer measurements, infrared thermography (§ 2.5.2) was used to visualize surface temperature patterns for the sake of vortex and transition front visualization, and focusing schlieren deflectometry (§ 2.5.3) was used for ultra-high bandwidth measurement of 2-D waves and cone alignment.

2.5.1 Constant-temperature anemometry

2.5.1.1 Working principles

The primary measurement technique in the present study is constant-temperature hot-wire anemometry (CTA). CTA utilizes the thermoresistivity of a thin wire and convective heat transfer in order to measure flow properties. The small size of the wire in combination with fast electronics offer superior spatial resolution and frequency response to most other measurement methods. In CTA mode, a voltage is applied to the wire, heating it resistively. As air flows over the sensor, the wire is convectively cooled and the voltage required to maintain the constant temperature increases. This voltage is then correlated to the mass flux over the wire using a suitable calibration scheme.

In a compressible flow, the rate of heat transfer from the wire as quantified by the Nusselt number takes the form

$$Nu = f\left(Re_d, Pr, M, \tau, \frac{\ell}{d}\right), \tag{2.1}$$

where ℓ is the length of the active portion of the wire, d is the wire diameter, Re_d is the wire Reynolds number, Pr is the Prandtl number, $\tau = (T_w - \eta_w T_0)/T_0$ is the temperature loading factor, T_w is the wire temperature, T_0 is the total temperature, $\eta_w = T_r/T_0$ is the wire recovery factor, and T_r is the recovery temperature.

The ℓ/d term represents the effect of heat conduction from the wire into the

prongs. For large ℓ/d and assuming a constant Pr,

$$Nu = f(Re_d, M, \tau). \tag{2.2}$$

The work of Kovasznay (1950) showed that in supersonic flows, the dependence of Nu on M (both directly and indirectly through η_w) is negligible, and therefore, in supersonic flows,

$$Nu = f(Re_d, \tau), \tag{2.3}$$

which can be expressed alternatively by

$$Nu = f(\rho U, T_0, \tau). \tag{2.4}$$

For a given τ, which is set and held constant prior to making any measurements, the wire voltage responds to changes in both mass flux, ρU, and total temperature, T_0.

Furthermore, it was shown by Smits *et al.* (1983) that for a sufficiently high τ, the wire response is primarily dependent on ρU, while the T_0 dependence becomes negligible. As a result, all measurements in the present study were performed with $\tau \geq 0.8$ such that the contribution of T_0 fluctuations to the hot-wire response was minimized as much as was practical. At similar conditions to the present experiments in a co-located facility, Semper (2013) showed that this assumption resulted in approximately 2% in error as a result of residual T_0 sensitivity.

2.5.1.2 Probe design and fabrication

All of the hot-wire probes and sensors in the present study were fabricated in-house using a modified version of the procedure described by Hofferth (2013). The sensors use a Wollaston wire with a 90%/10% rhodium/platinum core with $d = 5$ μm

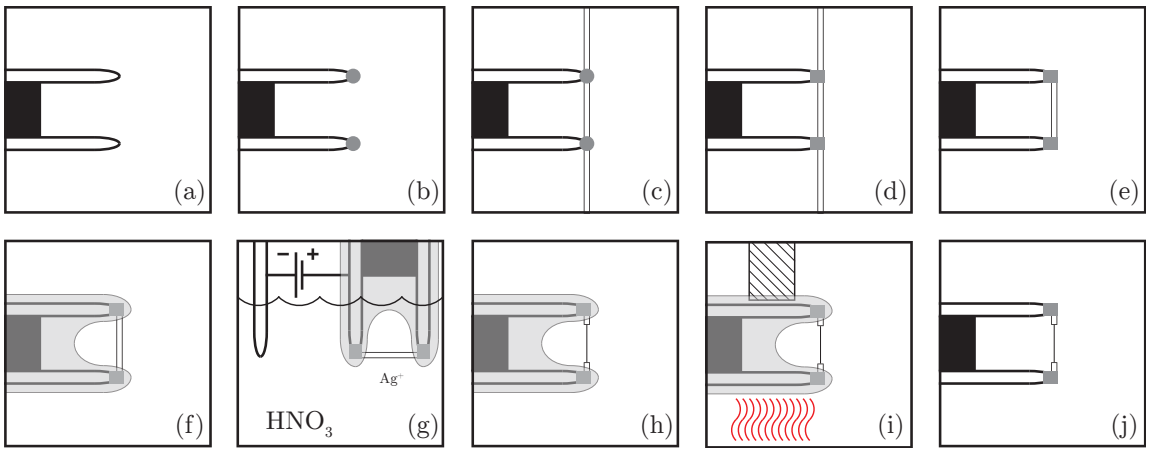

Figure 2.15: Hot-wire fabrication process.

that functions as the active element. The core is clad in silver to a diameter of approximately 50 µm for ease of manipulation. The wire is soldered to the prongs and silver coating is then selectively etched away from the wire to expose a length and create the active element. For the present experiments, the active length, ℓ, was typically between 600 µm and 700 µm, resulting in $120 \leq \ell/d \leq 140$.

The manufacturing procedure used by Hofferth (2013) involved a tediously painstaking etching process whereby a tiny drop of nitric acid was placed on a nichrome wire and used to remove a minute portion of the silver and repeated many times until the wire was exposed. The procedure was delicate and even small mistakes often lead to a wire breakage, requiring a restart of the process from scratch. As a result, the fabrication process was modified for the present experiments as illustrated in Figure 2.15.

The pins are first sanded and cleaned using a hydrochloric acid/zinc chloride flux and heat, then tinned with lead-free, 450°F solder (Figure 2.15a). Next, a small bead of solder-flux paste is applied to the tips of the prongs (Figure 2.15b). The wire is then moved into place using a binocular microscope for viewing the process

(Figure 2.15c), taking care to provide adequate slack in the wire to minimize the effect of strain-gaging (Kovasznay, 1953; Smits *et al.*, 1983). It is important to note that achieving a sufficient level of slack was key to producing a wire that is both durable and is free of strain-gaging modes. The wire ends were typically mounted at nearly a 45° angle to the line drawn between the two prong tips. The resulting sensors would often avoid any strain-gaging and would last as substantially longer than an un-slacked wire. The wire was then soldered to the pins (Figure 2.15d) and the loose ends were removed with a razor blade (Figure 2.15e). Paraffin wax was then melted on a low-temperature soldering iron tip and "painted" onto the probe tip, masking off areas that were not to be etched away (Figure 2.15f). The probe tip was then submerged in a small vial of 2 M nitric acid along with a second electrode (Figure 2.15g). When a voltage was applied across the two electrode (the probe serves as the anode), the system functions similar to electropolishing. All surfaces not masked by the wax are dissolved in the acid bath, leaving the insoluble active wire exposed (Figure 2.15h). The probe is then removed from the acid bath and the wax is removed using a heat gun and a wick (Figure 2.15i). The final probe tip is depicted in Figure 2.15j.

The NAL facilities utilize a modified A. A. Lab Systems AN-1003 hot-wire anemometer operated in constant temperature mode. The system has been optimized for 15 m cables and the custom M6QT probe design. For a 5 μm wire, this system is capable of achieving a corner frequency of $f_c \approx 180$ kHz. The frequency response is determined from the hot-wire response transfer function computed from a pulse test and measured using a National Instruments PCI-5122 digitizer/oscilloscope card.

It should be noted at this point that the frequency of the Mack mode is expected to be $f \approx 250$ kHz, which is substantially higher than the frequency response quoted above. Indeed, Hofferth (2013) utilized the same probe design using 2.5 μm wires

and was able to achieve a frequency response of $f_c \approx 280$ kHz. These smaller wires, however, are substantially more fragile. Since the present study seeks to generate contours of the boundary layer from profiles measured over many runs, wire durability was prioritized over frequency response.

For Mack-mode studies, the initial search for Λ vortex structures is primarily concerned with the structure mean flow and therefore does not require the higher frequency response. The study of any fluctuating quantities, once these structures are identified, would then require a smaller wire to resolve the Mack mode waves. In contrast, the crossflow study is primarily concerned with the stationary vortex structure and at least type-I secondary instabilities are expected to fall well within the frequency response of the 5 μm wire.

2.5.1.3 On hot-wire calibration and normalization

A hot-wire signal measured with a sufficiently high τ may, in general, be calibrated to the mass flux using the following relation:

$$E^2 = L + M(\rho U)^n, \tag{2.5}$$

where E is the hot-wire voltage, ρU is the mass flux, L and M are calibration constants for a given T_0 and τ, and n is a best-fit constant for the calibration data. Classically, $n \approx 0.55$ for sufficiently large Re_d. However, in the present experiments, $Re_d = O(1)$. Calibrated data for hot-wire sensors of similar design at similar conditions in a tunnel co-located with M6QT (Semper, 2013) as well as preliminary calibration estimates in M6QT (Hofferth, 2013) indicate that, for these probes at these conditions, $n \approx 1$.

The hot-wire measurements in the present study are uncalibrated. However, as shown by Smits *et al.* (1983), the high τ minimizes the effect of T_0 fluctuations on

the signal, representing approximately 2% error according to Semper (2013), and the reading therefore represents an uncalibrated mass flux measurement. The large number of wind tunnel runs required for each data set in the present study made wire breakages inevitable. Therefore, in lieu of a true calibration, measurements were normalized against a pair of free-stream and a near-wall points representing the lower and upper bounds on the voltage throughout the boundary layer. Provided that the $n \approx 1$ assumption is valid for each wire, this procedure provides both a DC shift in the hot-wire signal as well as scaling to the minimum and maximum boundary-layer values, corresponding to L and M in the Eq. 2.5. The normalized data from different wires are therefore approximately calibrated to each other, with the primary sources of uncertainty being variations in the precise location of the wall and free-stream points and any variation in n between wires. The mean and fluctuating components of these signals may then be used to compare the mean and fluctuating mass flux components as they develop throughout the flow. The spectral content of the signal also accurately reflects that of the unstable ρU modes in the boundary layer.

While obtaining calibrated data would be ideal, there are a number of reasons why this has remained impractical to date. The most significant of these is that, as has been previously discussed, the thin wires suffer from relatively short lifespans, with a typical probe lasting anywhere from a handful of runs to, more recently, a few dozen. The issue of probe lifespan therefore places limits on the feasibility of any calibration method requiring the use of many tunnel runs, as the calibration itself may use up an appreciable portion of the wire's life. Nevertheless, several calibration methods have been proposed and/or attempted in M6QT with mixed success.

The most convenient form of calibration would involve placing a probe in the tunnel free stream and performing a pressure sweep (ρU sweep), passing through many calibration points in a single run. While the range of mass flux in the boundary

layers of the models used in this study range from 0 to about 100 kg·m^{-2}·s^{-1}, the mass flux range achievable in the M6QT free stream under quiet flow is only about 25 to 45 kg·m^{-2}·s^{-1}, so there would be substantial extrapolation necessary to cover the range of mass flux in the boundary layer. While the tunnel is capable of operation at substantially higher pressures (up to $\rho U \approx 80$ kg $\cdot$ m^{-2} $\cdot$ s^{-1}), these conditions are unsuitable for wire calibration. Upon nozzle wall transition (just above 45 kg·m^{-2}·s^{-1}), the thicker nozzle-wall boundary layers cause a drop in Mach number of an unknown magnitude, making calculation of ρU from the known p_0 and T_0 impossible.

In response to the inadequacy of the standard pressure sweep, Hofferth (2013) outlined several proposed solutions to the calibration issue and their various pitfalls. The final proposal involved utilizing an oblique shock generated by a wedge model to increase the downstream mass flux in a known fashion. Such a design would be capable of producing ρU in excess of that in the upper portion of the boundary layer where the majority of the interesting content is located while still allowing low enough ρU to minimize extrapolation near the lower range of the boundary layer.

On its surface, the wedge method seems to be an ideal solution. It would, however, necessitate a model change any time a wire required calibration. Changing models incurs substantial risk to both the model and the nozzle while producing variability in the model alignment (shown by Hofferth (2013) to be a parameter of extraordinary importance for the stability characteristics of the boundary layer). To overcome this, it was proposed that multiple wires be calibrated simultaneously to produce many calibrated wires prior to a given campaign. Each wire would still requires its own separate run for tuning, but, once properly tuned, every wire could be calibrated simultaneously. Given the current instrumentation, this method could produce 4 calibrated wires with 9 tunnel runs (one per probe for wall finding, one per probe for tuning, and one for calibration of all probes). This represents two days of runs. The

primary remaining challenge is to adequately shield each probe from the start and unstart processes during the calibration runs.

2.5.2 Infrared thermography

Surface flow visualization was performed using infrared (IR) thermography. IR images were captured using a FLIR Systems SC8100 infrared camera. With its current support infrastructure, the camera is capable of taking 14-bit, 1024×1024 pixel images at approximately 30 frames per second in the 3.0 to 5.0 μm spectral range. For the present experiments, the camera is synchronized to the tunnel data acquisition system using a TTL pulse such that it captures ten frames per second, one centered in each data acquisition tunnel for the main tunnel operating parameters (the "slow" DAQ channels).

The steel models typically would not support the use of IR imaging as a result of their reflective surfaces. Hence, in order to adapt each model for IR use, the surface area of interest was coated with black, fiberglass-reinforced, PTFE-coated tape. The tape, including adhesive, is approximately 175 μm thick. The tape was applied only in downstream locations where the effect of its thickness on the flow was negligible.

2.5.3 Focusing schlieren deflectometry

High-bandwidth instability measurements were made using a lens-and-grid type focusing schlieren deflectometer. This system operates in a manner similar to that of a traditional schlieren system with the additional ability to focus on a region of interest in the flow. The resulting image is untainted by the effects of the turbulent shear layers at the nozzle exit. The removal of these shear layers from the signal allow the imaging of small boundary-layer fluctuations that would ordinarily be masked by noise.

The system consists of a light source and a Fresnel lens to produce a brighter,

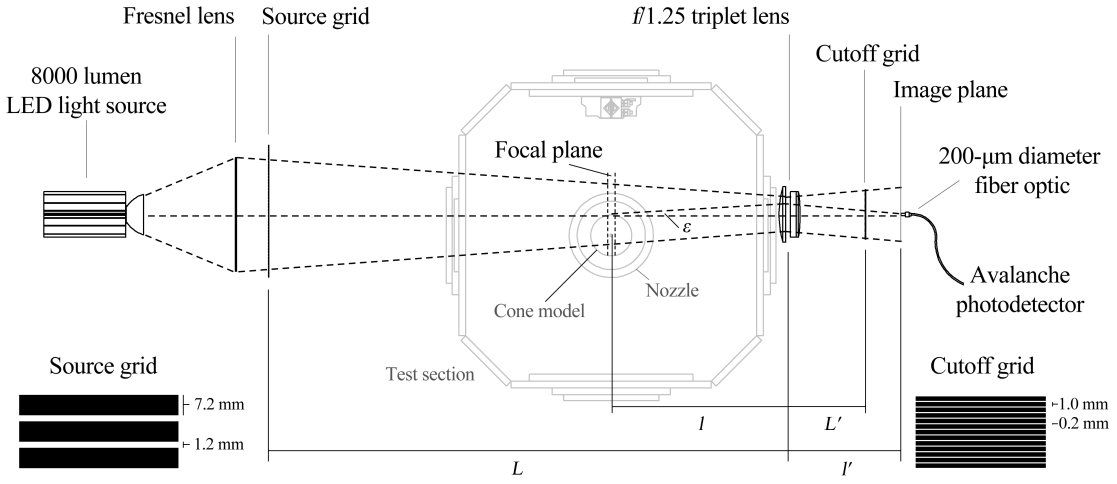

Figure 2.16: Detailed schematic of the focusing schlieren system (Hofferth, 2013).

more focused beam of light in the region of interest. In contrary to a standard schlieren system, the beam is not collimated. This beam passes through a source grid of opaque, black stripes and through the test section into a lens. The lens aperture and the non-collimated beam produce the focusing effect. The focused light is then passed through a cutoff grid, which is the photographic negative of the source grid and functions analogously to the knife edge in standard schlieren system. In this way, each pair of source and cut-off stripes acts as a separate light source and knife edge pair, and the system may be described as a superposition of multiple conventional systems (Hofferth *et al.*, 2013).

The resulting image can be viewed either directly or, as in the present study, using a optical fiber and a photodiode in order to record the light intensity at a single point. This system has a frequency response that is much higher than that of the CTA system and has been successfully used to capture harmonics and nonlinear interactions of the high-frequency Mack mode (Hofferth, 2013). Detailed information on this system may also be found in Hofferth *et al.* (2013).

Regime	T_{01} [K]	p_{01} [kPa, absolute]	M	Re' [$\times 10^6$ m^{-1}]
Quiet (BVO)	430	200 – 1000	5.9	2.3 – 11
Noisy (BVO)	430	1000 – 1350	5.8	11 – 15
Noisy (BVC)	430	200 – 1350	5.8	2.3 – 15

Table 2.2: M6QT operating envelope (Hofferth, 2013).

This system was primarily used for model alignment purposes in the present system. The focal depth is roughly 25 mm, and as such the system is well-suited for measurements of two-dimensional waves such as those of the Mack mode. However, the present study aims to study three-dimensional phenomena where the length scale normal to the focal plane is an order of magnitude smaller than the focal depth. Therefore, the three-dimensional content would be lost to the spatial integration of the system and it is unsuited for three-dimensional boundary layers of these sorts.

2.6 Operating procedure

The M6QT operates in three distinct regimes: quiet and noisy with the bleed valves open (BVO) and noisy with the bleed valves closed (BVC). The typical operating envelope for each of these regimes is tabulated in Table 2.2. It should be noted that while quiet flow is achieved by opening the bleed valves, this does not guarantee quiet flow in the test section. With BVO, quiet flow can be maintained from a unit Reynolds number of approximately $2.3 \times 10^6/\text{m} \leq Re/L \leq 11 \times 10^6/\text{m}$. While the tunnel will continue to run until roughly $Re/L = 15 \times 10^6/\text{m}$, at this Reynolds number the nozzle wall experiences early transition and quiet flow is lost regardless of the bleed valve status.

During a typical run, the total temperature of the flow, T_{01} must be maintained at an elevated 430 K in order to prevent the liquefaction of oxygen in the test section. In order to facilitate this, prior to each run the tunnel is convectively preheated at

a lower total pressure and no ejectors in order to bring the settling chamber and nozzle up to temperature. Early in the day, when the tunnel is still cool, this takes roughly 5 minutes. After the initial preheat, the tunnel temperature remains fairly high throughout the day due to 8 kW of electrical resistance heating installed on the settling chamber and fiberglass insulation installed along the entire flow path between the flow heaters and the nozzle. Preheats during the remainder of the day are therefore considerably shorter. During the final seconds of the preheat, the total pressure is raised to its desired value for the run.

Once the desired temperature and total pressure are achieved and the flow is stopped, the ejector is activated and allowed several seconds to draw the test section and diffuser down to approximately 1 kPa. The upstream valve is then opened, supplying pressure to the settling chamber and starting the tunnel. The bleed valves are typically opened after the upstream supply valve is opened and the settling chamber has reached roughly half of its desired value. At this time the tunnel has achieved its test conditions and measurements can begin. This condition can be maintained for approximately 40 to 50 seconds.

When the measurements are completed or the tank pressure reaches 9600 kPa, the bleed valves are closed and the ejector supply valves are closed, resulting in tunnel unstart. The tunnel supply valve is then closed and the air lines allowed to vent subsonically until the pressure reaches ambient and the remaining valves are closed.

3. RESULTS: THE MACK MODE ON A FLARED CONE

3.1 Overview

A series of recent computation studies by Sivasubramanian & Fasel (2012*a*,*b*) have indicated that the Mack mode, despite being a two-dimensional wave, exhibits highly three-dimensional behavior prior to its eventual breakdown to turbulence. Furthermore, this behavior is expected to take the form of Λ-vortices in a so-called K-type breakdown. This phenomenon, if confirmed, would closely mirror the breakdown behavior of Tollmien-Schlichting waves in subsonic flows.

In an effort to observe the hypothesized K-type breakdown, the LaRC 93-10 flared cone was used in M6QT. The characteristics of the Mack mode have been well-studied on this cone (Lachowicz & Chokani, 1996; Hofferth & Saric, 2012; Hofferth *et al.*, 2012; Hofferth, 2013; Hofferth *et al.*, 2013) and it is well-known that transition does not occur on the model under M6QT quiet operation, although evidence of nonlinear behavior was observed. As a result, it is believed that the Mack mode waves in boundary later over the LaRC 93-10 in M6QT need only be stimulated slightly in order to achieve transition.

Two methods were employed in order to attempt to stimulate the boundary layer. First, a two-dimensional strip was affixed to the surface in order to provide a larger initial amplitude to the two-dimensional wave with a streamwise length of $0.5\lambda_{\text{Mack}}$ (where λ_{Mack} is the expected Mack-mode wavelength). This strip was applied in conjunction with a small-amplitude ring of DREs to encourage the development of the oblique waves at the specified wavenumber $k_c = 150$ (based on the results of Sivasubramanian & Fasel, 2012*a*,*b*). It is expected that these oblique waves and their interaction with the primary two-dimensional wave play a key role in the production

of the Λ-vortices.

Second, a single ring of DREs were applied using a modified design. These elements had an ovoid geometry with their major axes aligned with the free stream. The major axes were of length $0.5\lambda_{\text{Mack}}$ in order to stimulate the two-dimensional wave. The minor axes were sized such that their width was $0.5\lambda_c$, where λ_c is the wavelength obtained by dividing the circumference by the azimuthal wavenumber,

$$\lambda_c = \frac{2\pi z \tan \phi_c}{k_c}, \tag{3.1}$$

where z is the axial location and ϕ_c is the cone half-angle. The objective of this modified design was therefore to stimulate both the two-dimensional and oblique waves with the same set of roughness elements.

Boundary-layer measurements were performed using constant-temperature hot-wire anemometry (CTA). All CTA signals were sampled for 100 ms at a rate of 1 MHz. These signals were there squared in order that they are proportional to the mass flux (§ 2.5.1, Eq. 2.5).

The sampled signal represents the sum of a steady, mean component with a perturbation component centered around the mean,

$$V^2(r, \theta, z, t) = \overline{V^2}(r, \theta, z) + (V^2)'(r, \theta, z, t). \tag{3.2}$$

The mean component, $\overline{V^2}$, is measured by taking the mean of the squared signal. The signal is separately passed through an AC-coupled amplifier to increases the resolution of the fluctuations, which is then sampled to obtain an amplified V' signal. This is combined with $\overline{V}$, squared, and $\overline{V^2}$ subtracted to calculate $(V^2)'$.

3.2 Model alignment

Small deviations from 0° angle of incidence will not affect the dominance of the Mack mode (as opposed to a three-dimensional instability such as crossflow). However, experiments (Hofferth, 2013) and computations (Kocian *et al.*, 2013) alike have shown the most amplified frequency to be highly dependent on even small amounts of misalignment, complicating comparisons between experiments and computations. In particular, Hofferth (2013) observed on the same cone in M6QT a deviation of approximately 84 kHz per degree of deviation from 0° incidence for measurements taken near the attachment line. As such, special care must be taken when installing the model.

This extreme sensitivity to angle of incidence is not without its advantages, however. While it complicates the installation of the model, it also provides an extraordinarily sensitive model alignment tool. In performing such an alignment procedure, the focusing schlieren deflectometry (FSD) system is used to measure boundary-layer fluctuations along both the top and bottom ray of the cone. A pressure sweep is performed across a range of Re'. The spectrograms for the top and bottom measurements are compared and the angle adjusted until both the most amplified frequency, f_0, and the slope of f_0 versus Re' match. At this point the cone is as near 0° as is practical. An example of one such spectrogram is depicted in Figure 3.1. Often, the small adjustments necessary require only a fraction of a turn of the mounting bolts.

3.3 Operating conditions

The flow conditions in the present experiment were typically chosen to maximize Re' while maintaining quiet flow in the free stream. This corresponds to $T_0 \approx 430$ K and $p_0 \approx 896$ kPa (130 psia), corresponding to $Re' \approx 10 \times 10^6$/m. Each run lasted

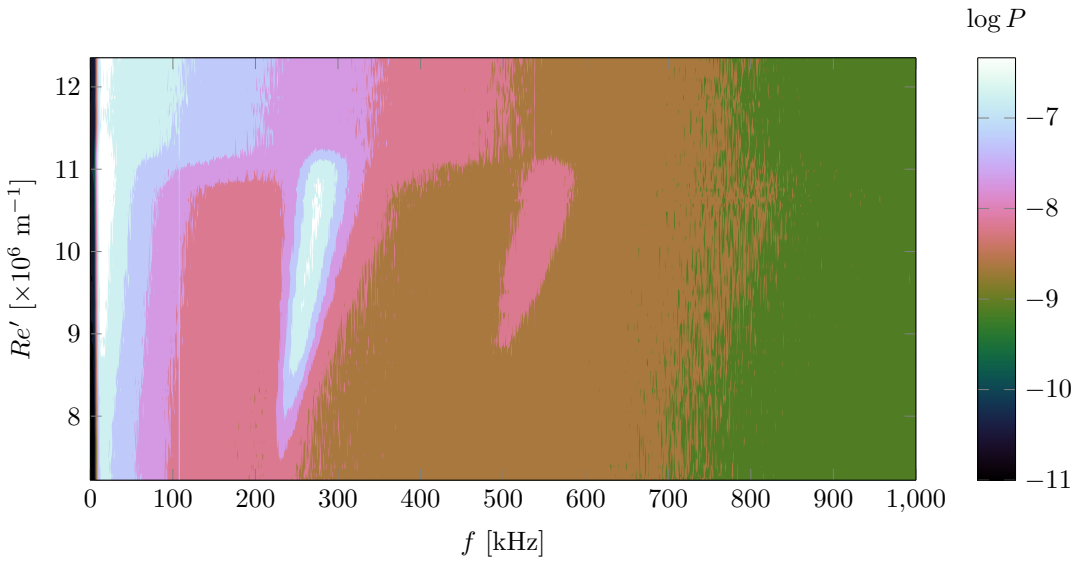

Figure 3.1: Typical spectrogram produced during a pressure sweep used for cone alignment.

approximately 40 seconds.

While the Mack mode is sensitive to the wall temperature, there is no way to set and maintain a constant wall temperature during the course of a tunnel run. As a result, the thin-walled LaRC 93-10 heats to a temperature greater than the adiabatic wall temperature (for a laminar flow) as a result of the preheat and slowly cools during the course of the actual run. At the beginning of the run, $T_w/T_{aw} \approx 1.05$. By the end of the run, the wall has cooled somewhat to $T_w/T_{aw} \approx 1.03$. Figure 3.2 depicts the surface temperature of the model as a function of time and axial location during a run. The hot-wall condition therefore serve to slightly stabilize the Mack mode.

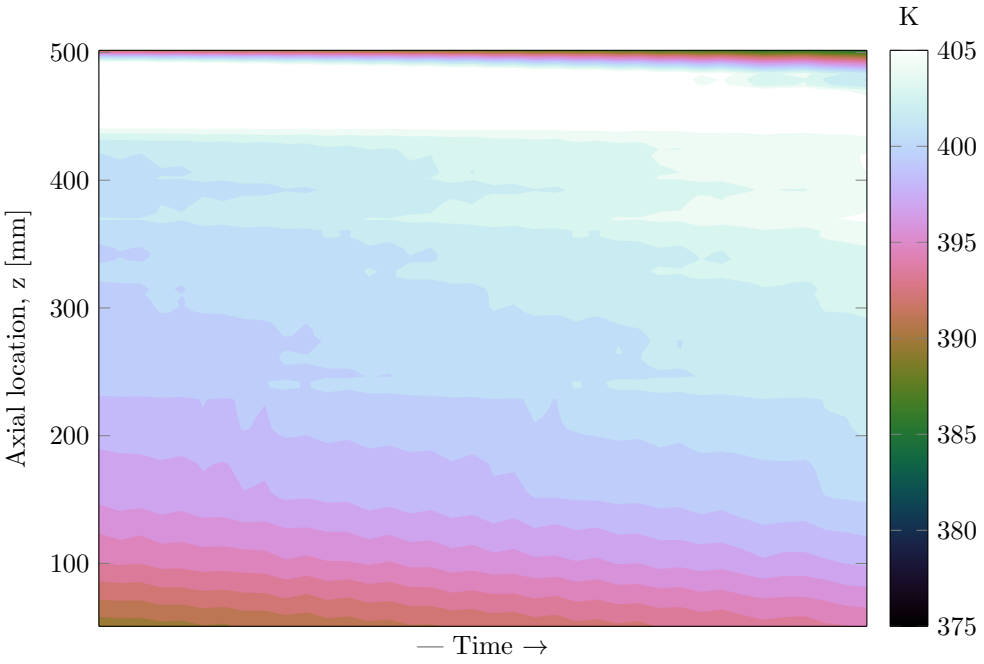

Figure 3.2: Model surface temperature on the LaRC 93-10 flared cone over the course of one tunnel run.

3.4 Two-dimensional strip and DRE

3.4.1 Roughness elements

The first method of exciting the Mack mode to be employed was the two-dimensional strip with a ring of DRE. The strip was placed at $z = 134$ mm along the cone axis. It was cut from a strip of Kapton® tape and affixed to the surface. At the point where the two ends met, opposite the test side of the model, a small drop of cyanoacrylate glue was applied to prevent the strip from peeling away during a run. The strip was 127 μm in thickness per layer, and 1.4 mm in streamwise width ($\approx 0.5\lambda_{\text{Mack}}$). Measurements were made using this configuration with both one and two layers of the tape, however, owing to their similarity, only the two-layer case is discussed herein.

The DRE ring used in conjunction with the Kapton® strip were dry-transfer ink much like those used by Hunt (2011). These circular DREs were placed at $z = 138$ mm to match the location of the disturbance in Sivasubramanian & Fasel (2012*b*). They were placed at wavenumber of $k_c = 150$, resulting in $\lambda_c \approx 1$ mm. The diameter of each element was $d = \lambda_c/2 \approx 0.5$ mm and the height of each element was 13 μm.

3.4.2 Hot-wire measurements

Given the fragility of the 2.5 μm wires required to fully resolve the expected 250 kHz Mack mode, it was decided to use 5 μm wires (with a frequency response up to approximately 180 kHz) in the initial experiments while searching for evidence of mean-flow distortion. The roughness elements are spaced at $k_c = 150$, therefore, any azimuthal modulation is expected to occur at the same wavenumber, which corresponds to $\lambda = 2.4°$.

A number of measurement profile patterns were used, including boundary-layer profiles in the r-direction and azimuthal profiles in the θ-direction. For example, a series of r profiles conducted on the interval $87.6° \leq \theta \leq 89.2°$ were performed (Figure 3.3). While the wire broke after the 89.2° run and the range represents only 2/3 of one wavelength, it would be expected that even over this truncated distance, clear evidence of azimuthal variation should be observable. As is clear from the picture, no such variation is readily apparent.

Further evidence of the lack of azimuthal variation was provided by a series of azimuthal scans which, when strung together, cover several wavelengths worth of azimuthal distance. Figure 3.4 shows several of these scans strung together to cover a range of several wavelengths. The small variation that does exist and leads to slight discontinuity at the borders between each run is explained by the slight variation in Re' over the course of each run, producing a slight thickening of the boundary layer

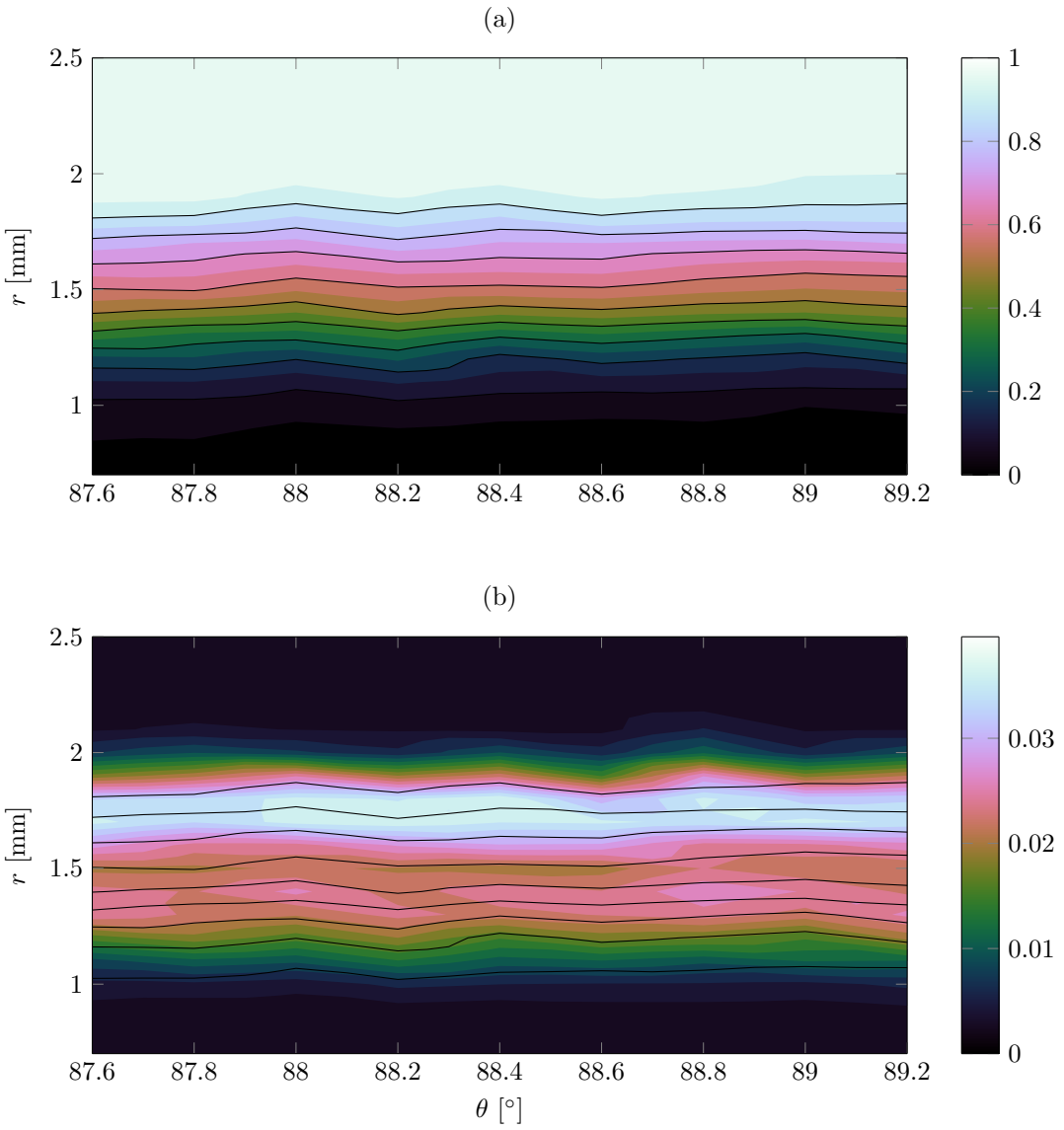

Figure 3.3: Flow contours at $z = 493$ mm over the 93-10 flared cone with the 2-D strip and DREs. Contours of mean (a) and fluctuating (b) hot wire voltage normalized by the boundary layer range.

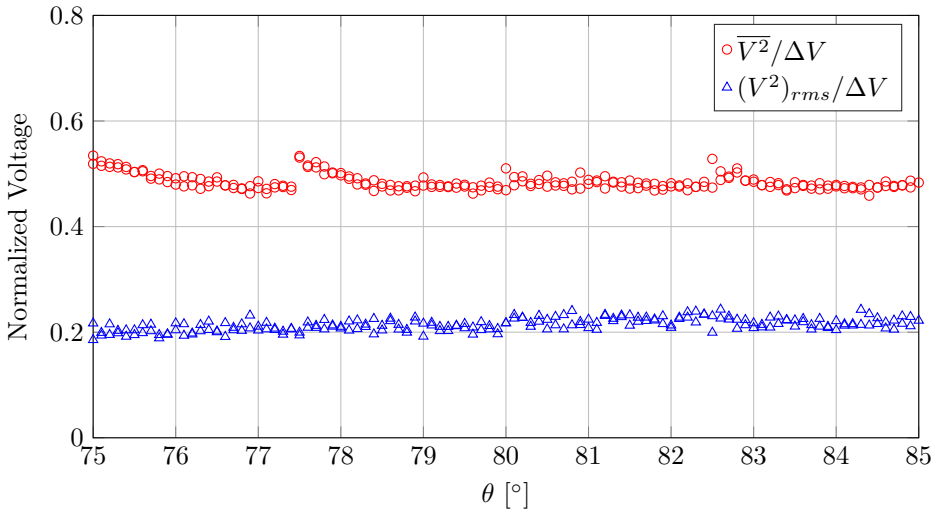

Figure 3.4: A series of azimuthal boundary layer scans at $r = 1.575$ mm over the 93-10 flared cone with two layers of tape and DREs. $Re' \approx 10.5 \times 10^6$/m.

over time.

Despite considerable effort and over 50 tunnel runs worth of data, no evidence of azimuthal variation in either the mean flow or the fluctuating signal was observed. It was decided that the most likely explanation was that the height (13 μm) of the DREs was simply too small to meaningfully affect the flow. Even with an increased amplitude in the primary wave, the oblique wave may simply have too little space to growth to sufficient amplitude for nonlinear interaction with the primary wave before reaching the base of the cone. As a result, an alternate method of DRE application was sought.

3.5 Ovoid decal DRE

3.5.1 Roughness elements

In light of the inability of the strip/DRE to produce the desired result and the aforementioned diminutive size of the DREs, it was decided that the strip and DREs

should be combined into one set of modified DREs. Further, it was important that the new design could be easily layered in order to produce larger overall roughness heights. This resulted in several challenges, chief among them being the difficulty of working with dry-transfer DREs both in their initial application and in lining up additional layers on a curved surface.

The dry-transfer DREs have previously be applied in multiple layers in low-speed applications in a straight, flat line. In such situations, alignment of additional layers is comparatively simple compared to aligning a ring around a cone. When attempting to apply multiple layers to the conic surface, however, the fragility of each dot became apparent when the simple act of aligning a new layer was often enough to dislodge one or more of the elements from the surface, ruining the pattern. As a result, alternate methods of DRE application were sought.

The most promising solution was high-temperature vinyl water slide decals. This method uses a UV-cured ink screen-printed onto a dextrose transfer paper in the desired pattern. The decals are wetted and removed from their backing paper and placed on the surface. The adhesion is derived from the water/dextrose mixture that is spread on the surface during application. This combination dries overnight, and while still wet acts as a lubricant, allowing the DRE pattern to be easily slid into place and aligned even while the pattern is in contact with the surface. The resulting bond is strong enough to hold up to surface cleaning with water (necessary to remove the remaining dextrose residue), touching the surface with a finger, or sliding another layer of decals over the top for alignment. The decals may be easily removed with acetone.

The decal DREs for the present experiments were printed in an ovoid shape (Figure 3.5) and sized in order to be placed at $z = 138$ mm. At this location, $\lambda_c \approx 0.5$ mm and the width of the DREs was chosen as half the azimuthal wavelength. The length

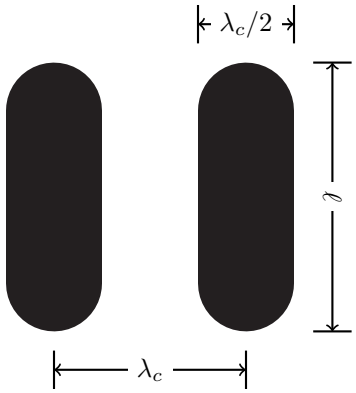

Figure 3.5: Diagram showing the layout of ovoid decal DREs.

of the elements was chosen as half the wavelength of the most amplified Mack-mode frequency, which in this case, resulted in $\ell \approx 1.4$ mm. Due to a manufacturing error, the DREs produced were translucent, and as such, optical profilometry measurements of their height were plagued with high uncertainty. While an exact height was not possible, each layer is approximately 20 µm in height with noise in the measurments constituting approximately ±5 µm worth of scatter. Measurements were performed with three layers of DREs applied to the surface for a total roughness height of $k \approx 60$ µm, or $Re_{kk} \approx 1$.

3.5.2 Hot-wire measurements

Hot-wire measurements with the decal DREs installed followed much the same pattern as with the strip/DRE combination. Once again, a 5 µm wire was used for the exploratory portion of the campaign.

A series of r profiles spanning $80° \leq \theta \leq 86°$ were taken and combined to obtain a

contour at the axial location $z = 493$ mm and is depicted in Figure 3.6. Once again, the mean flow (Figure 3.6a) shows no evidence of azimuthal variation. The fluctuating content (Figure 3.6b) does show considerable variation in azimuth. However, these fluctuations occur at a wavelength that appears to be considerably larger than the expected 2.4°. Further investigation of this variation was therefore required.

The run at $\theta = 86°$ was repeated to check for repeatability. The mean signal matched the first run at that location, but the fluctuating signals from the two runs did not match. Re-tuning the wire resulted in improvement, however, shortly thereafter, the wire broke. It is therefore evident that changes in the probe resitance near the end of life affected the dynamic response of the anemometer, resulting in erratic fluctuation measurements. As the mean signal remained repeatable throughout the process, Figure 3.6a is assumed to remain valid. However, Figure 3.6b is clearly tainted by the degradation of the wire's dynamic behavior near the end of its life.

Despite the failing wire, over the course of a single run, the results were still instructive in regards to looking for azimuthal modulation. Several azimuthal scans were performed over a range of several expected wavelengths. Figure 3.7 shows one such scan performed at $(r, z) = (1.65, 493)$ mm. Once again, there is no evidence of azimuthal variation in either the mean signal or the fluctuating signal. This run was followed by a campaign of over 30 additional similar runs, both in hot- and cold-wire configurations and a number of (r, z) positions. No evidence of azimuthal variation was found in any of these measurements.

3.6 Discussion

It is apparent that the present DRE configuration is unable to excite Mack mode waves and the interacting oblique waves sufficiently to achieve breakdown on the LaRC 93-10 cone in M6QT. There are several factors that likely play a role in why

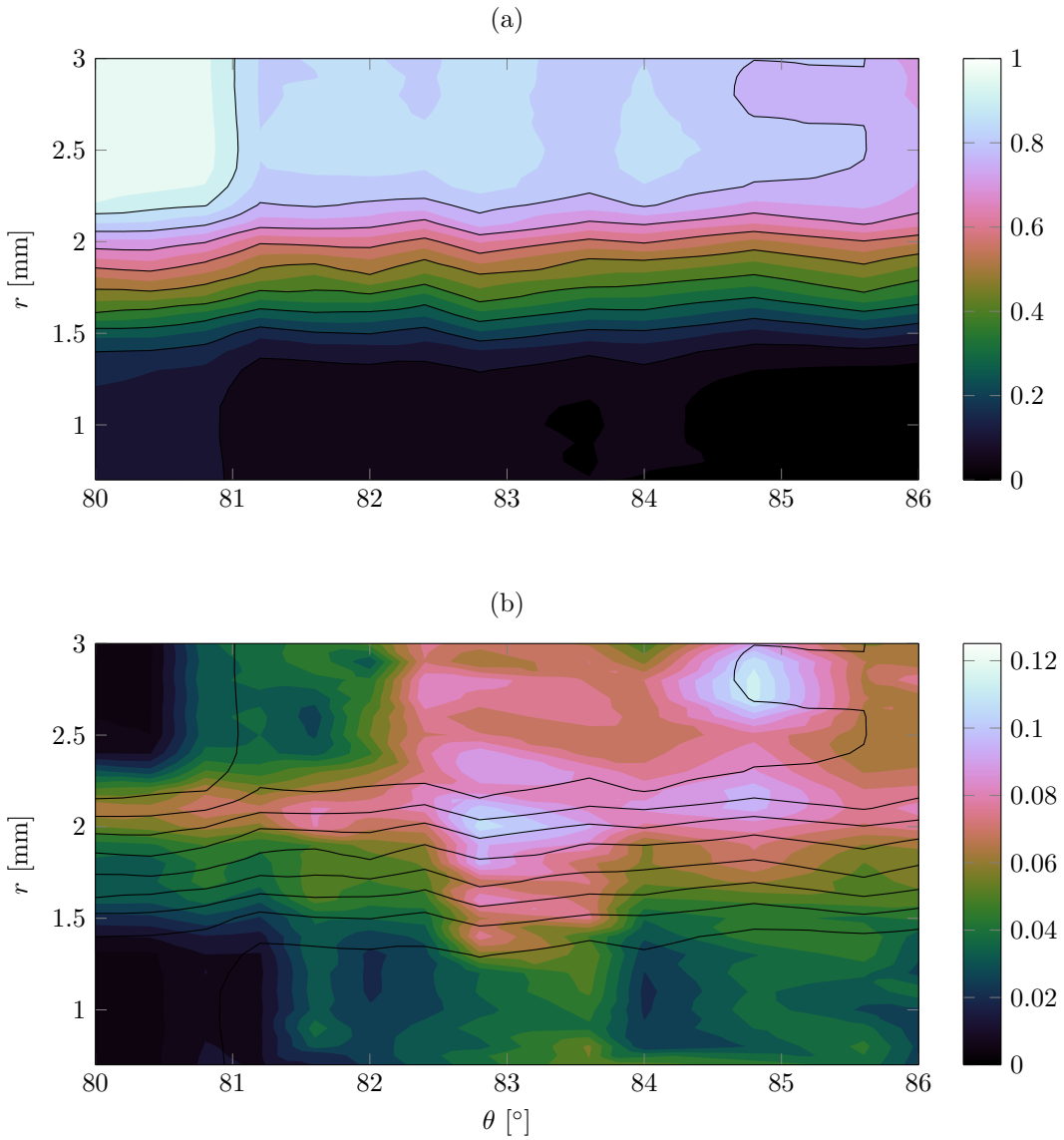

Figure 3.6: Flow contours at $z = 493$ mm over the 93-10 flared cone with ovoid DRE decals. Contours of mean (a) and fluctuating (b) hot wire voltage normalized by the boundary layer range.

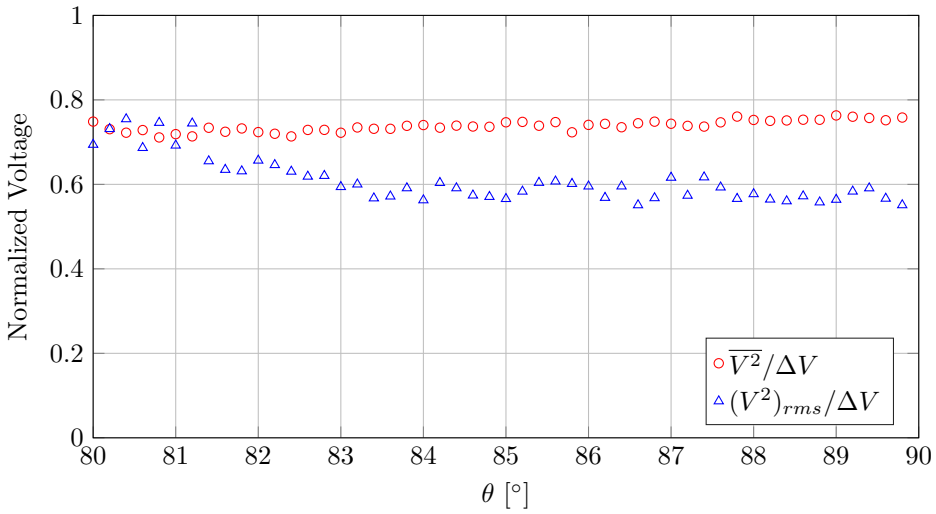

Figure 3.7: Azimuthal boundary layer scans at $r = 1.65$ mm over the 93-10 flared cone with 3 layers of decal DREs. $Re' \approx 10 \times 10^6$/m. Unusually high fluctuation levels may be due to failing wire.

this is the case. It is likely that addressing several of these issues would be required in order to achieve breakdown.

First, the DREs may simply be too small. It is already known that considerably greater roughness is required to meaningfully affect a hypersonic boundary layer as compared to the subsonic case. It may therefore be necessary to increase the roughness height in order to input a larger initial disturbance. However, care must be taken to avoid roughness elements so large that a persistent wake is formed (Luersen, 2012), as this fundamentally alters the stability of the boundary layer. This step might easily be implemented in M6QT by applying additional layers of DREs.

Second, a hot wall is counterproductive toward achieving maximum N on a given model. Further destabilization of the Mack mode may be achieved by instead enforcing a cold wall on the model. Currently, a cooling system is available for use in M6QT with this intended purpose. However, the LaRC 93-10 is not at present

compatible with this system. In order to implement wall cooling, modification to this model is necessary. Other models that are already compatible require modification for compatibility with the installation system and traverse in M6QT.

It is possible that no possible combination of larger roughness and a colder wall will result in sufficient amplitude to break down over the relatively small distance available on any M6QT model. If such is the case, there are two possible solutions. A new model design may be necessary, such as a novel compression cone design. Such a model may take the form of a cone with a variable, large-radius flare extending nearly to the tip. The flare might also be tailored so as to provide a constant boundary-layer thickness, ensuring that a narrow band of frequencies remains the most amplified over the entire length of the model, achieving maximum N for that band.

The remaining option is to use a larger model capable of achieving substantially higher Re along the arc length of the model. Such a model is not feasible for use in existing facilities due to their size. As such, this approach would require the construction of a new, larger low-disturbance facility, requiring considerable investment of time and resources.

4. RESULTS: CROSSFLOW INSTABILITY ON A YAWED CONE

4.1 Overview

The bulk of the present set of experiments entails a detailed study of the crossflow instability in the boundary layer over a yawed, 7° cone (§ 2.2.2) in Mach 6 flow at 5.6° yaw. This section details the natural, stationary crossflow study using a smooth cone tip. A similar study using a rough cone tip is detailed in § 5.

As the azimuthal integration renders focusing schlieren unsuitable for three-dimensional flows of this sort, the principle measurement techniques are CTA for boundary-layer measurments and IR thermography for surface flow visualization.

The analysis in this chapter is broken down into several sections. The run conditions for the yawed cone are discussed in § 4.2, IR flow visualization is discussed in § 4.3, the CTA measurements are covered in detail in § 4.4.

4.2 Operating conditions

Each run in the present set of experiments spans approximately 30 seconds at constant conditions. Unless otherwise specified, the run conditions for each point are $T_0 \approx 430$ K and $p_0 \approx 896$ kPa (130 psia) corresponding to $Re' \approx 10 \times 10^6$ m^{-1}.

In order to achieve an adiabatic wall on the thick-walled cone model, a 624 W heating element was placed inside the model and operated with a PID process controller. The cone is heated to $T_w = 375$ K using the heating element and allowed to convectively heat to $T_w = 400$ K during the tunnel preheating process. The result is a nearly constant temperature during the course of a run (Figure 4.1), indicating that $T_w/T_{aw} \approx 1$. The tip and base of the frustum typically remain at $T_w/T_{aw} \approx 0.988$ and $T_w/T_{aw} \approx 0.963$ respectively due to their proximity to the large, unheated thermal mass in the cone tip and base respectively. The aft-most measurement location is at

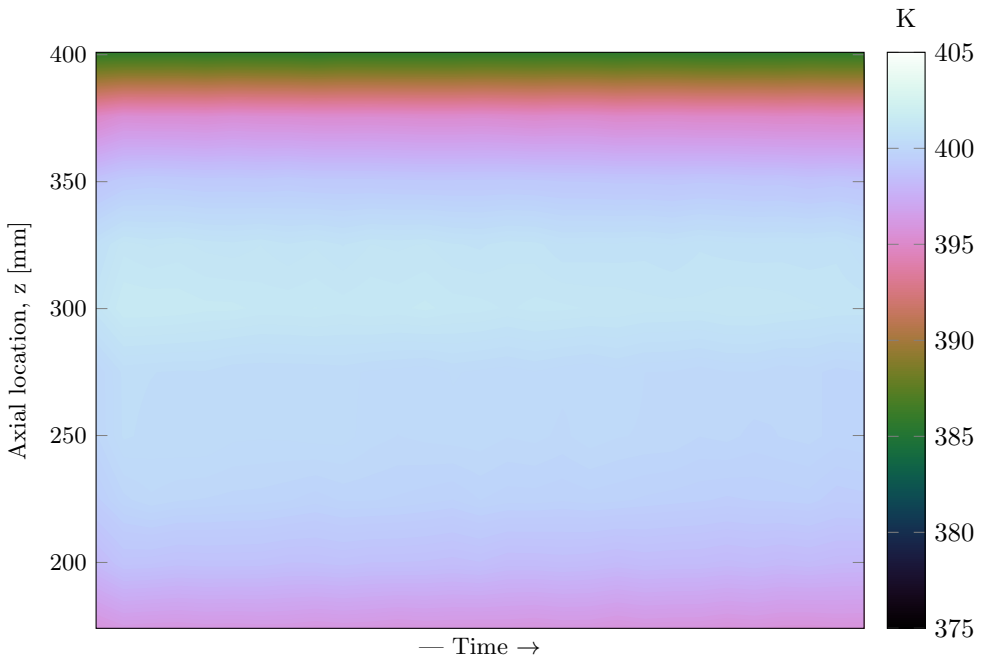

Figure 4.1: Model surface temperature on the TAMU 7DC over the course of one tunnel run.

$T_w/T_{aw} \approx 0.98$. For runs utilizing IR thermography, the cone is left unheated in order to increase the heat transfer rate into the surface and maximize the temperature difference across each streak.

4.3 Infrared flow visualization and transition detection

In order to facilitate the use of IR imaging, a non-reflective, PTFE-coated tape was placed over a portion of the base of the model. This patch spanned 50 mm upstream from the base (380 mm $\leq z \leq$ 430 mm) and 67.5° in either direction from the leeward attachment line (112.5° $\leq \theta \leq$ 247.5°).

Since hot-wire measurements are inherently delicate and time-consuming, IR flow visualization was first conducted in order to help confirm the existence of stationary crossflow waves and experimentally confirm their approximate spacing. Figure 4.2

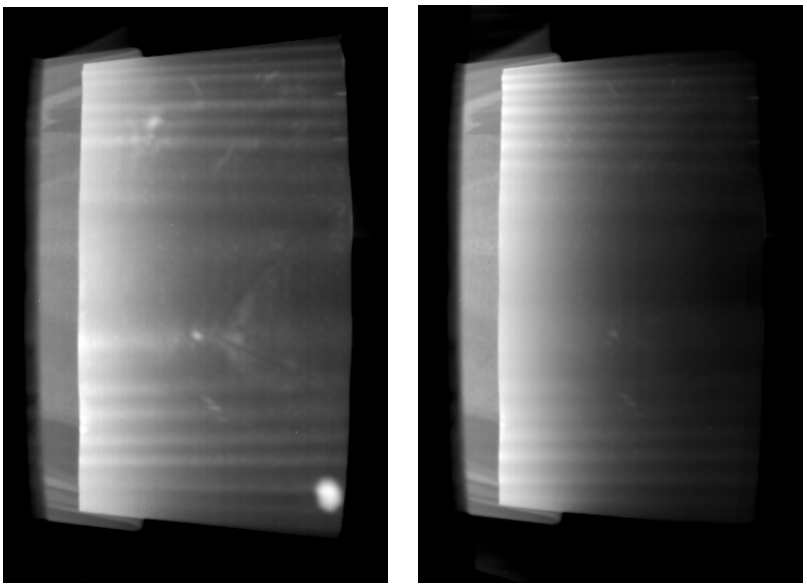

Figure 4.2: IR thermography depicting crossflow vortices on TAMU 7DC. Flow is from left to right. Left: $Re' = 10 \times 10^6$ m^{-1}, right: $Re' = 11 \times 10^6$ m^{-1}.

depicts two IR images taken at the typical $Re' = 10 \times 10^6$/m flow condition on the left and and elevated $Re' = 11 \times 10^6$/m on the right. Both images show a strong stationary crossflow pattern on the leeward half of the cone with spacing approximately equivalent to that predicted by NPSE calculations (Kuehl *et al.*, 2012).

The purpose of the high-Reynolds-number case was to operate at the margins of quiet flow in the tunnel and determine whether natural transition was possible without roughness elements. Transition was not observed in any quiet-flow run, as evidenced by the strong crossflow streaking present in the high-Re' case. Since this high-Re' condition is at the margin of reliable quiet flow in M6QT and still did not achieve transition, all subsequent measurements were performed at the lower Re' condition.

4.4 Hot-wire measurements

Natural crossflow was measured in detail at five equally-spaced axial locations in the range, 350 mm $\leq z \leq$ 390 mm. A series of constant-height scans were made over the same azimuthal range in order to generate a grid of points in the (r, θ) plane normal to the cone axis at a given z location. Azimuthal profiles were selected instead of wall-normal profiles for two reasons. First, azimuthal profiles were shown to allow greater flexibility in run time and the maximum number of sample points available in a given run. Second, as the θ gradient was expected to be of greater import to secondary instability, azimuthal profiles ensure that any profile misalignment would affect only the r gradient.

4.4.1 z = 350 mm

The most upstream measurement location was $z = 350$ mm. At this location, the stationary crossflow wave was already well into its development and has created a wave stucture which, while it has not yet exhibited the rollover characteristic of more developed crossflow, has already begun that process and shows substantial skew to the windward side (Figure 4.3a). The most amplified crossflow wavelength according to linear theory (Kuehl *et al.*, 2012) is expected to be somewhere in $50 \leq k_c \leq 60$ band, and with approximately 6° of spacing in Figure 4.3a, the measurements are consistent with predictions. The contour of rms fluctuation levels (Figure 4.4b) shows substantial fluctuations up to 11.6% located primarily in the region along the leeward edge of each upwelling.

Figure 4.3c depicts a series of normal profiles generated using the contour data at a 0.5° spacing (thin lines) and their mean (thick, black line). Further, the departure of each profile from the mean flow (mass flux defect) is plotted for each normal profile in Figure 4.3d. Taking the azimuthal rms of these profiles produces a stationary

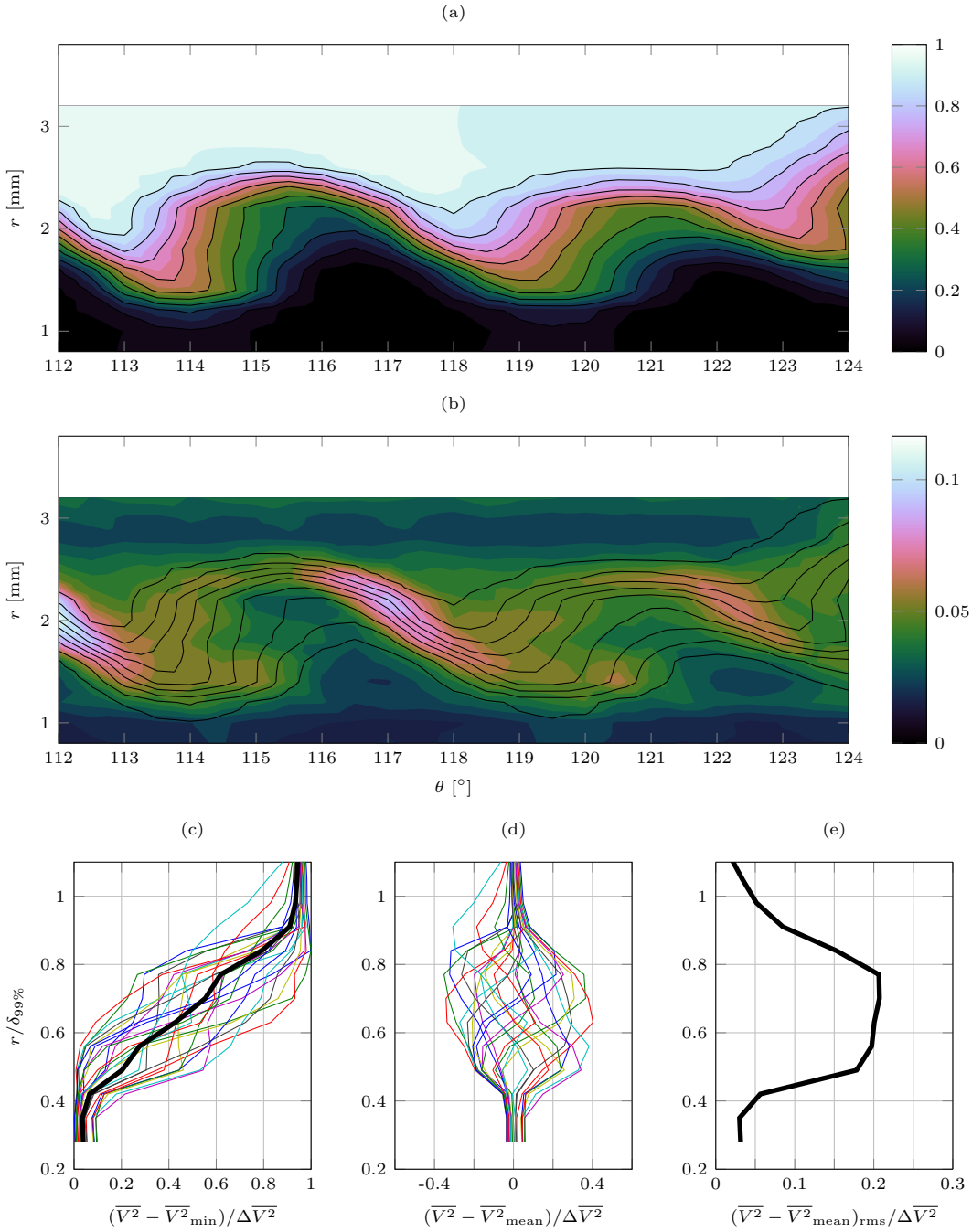

Figure 4.3: Hot-wire data at $z = 350$ mm. (a) Mean flow contour showing contours of normalized mass flux ($\overline{V^2}$). (b) Normalized rms mass flux fluctuation levels ($(V^2)'_{\text{rms}}$) plotted as a fraction of the free-stream value. Contour lines are levels of 10% mean flow. (c) Wall-normal profiles of normalized mean flow, (d) rms mass flux fluctuations, and (e) mean mass flux defect. Thick black lines are the mean of all profiles.

wave mode shape, shown in Figure 4.3e. At $z = 350$ mm this point, the maximum mode amplitude has already reached nearly 21%. However, it is still likely that the growth adheres to linear theory to this point, as the mode shape does not feature a noticeable secondary lobe such as those indicative of significant nonlinearity in low speed flows (Reibert *et al.*, 1996; White & Saric, 2005).

The fluctuating signal was further analyzed by placing the power spectral density into a three-dimensional array, P_{ijk}, where each i corresponded to one element in the r-vector, each j corresponded to an element of the θ-vector, and each k corresponded to an element of the f-vector produced by the FFT. In this way, each slice at constant k represents a spatial contour in (r, θ) space of the power spectral density of a particular f. By sliding through the values of f, frequency bands with high spatial localization. In this way, two frequency bands were identified with spatially coherent content: 15 kHz $\leq f \leq$ 60 kHz and 80 kHz $\leq f \leq$ 130 kHz.

Figure 4.4 depicts contours of the fluctuation rms levels in signals that have been band-passed in the frequency bands of interest using an 8th-order, zero-phase, digital Butterworth filter. As can be seen in Figure 4.4a, the energy in the $[15, 60]$ kHz band at this location is spread fairly evenly along the areas of high mass flux gradient. This frequency band represents the expected frequency range for traveling crossflow. See § 4.5 for further discussion of the low-frequency band. Figure 4.4b depicts the energy in the $[80, 130]$ kHz band. This band is located in the region associated with secondary instability in low speed flows and its frequency matches well with the convective scaling relationship for secondary instability in low speed flows. See § 4.6 for further discussion of the high-frequency band.

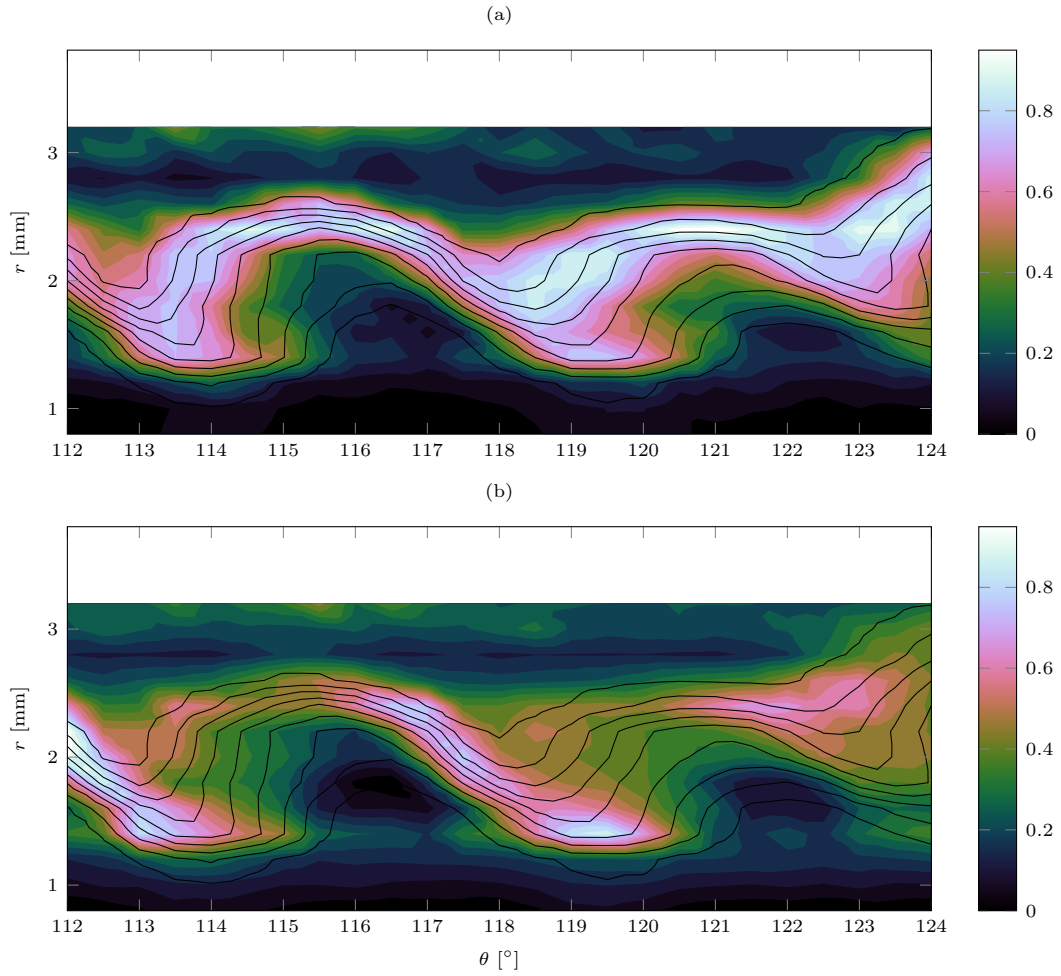

Figure 4.4: Contours of band-passed fluctuation rms at $z = 350$ mm in the bands (a) [15,60] kHz and (b) [80,130] kHz. Levels are relative to the maximum fluctuation rms level in each band.

4.4.2 z = 360 mm

Moving downstream to $z = 360$ mm, the mean flow (Figure 4.5a) shows a regression slight regression of the crossflow vortex structure compared to the observations at $z = 350$ mm. There is no evidence that the rollover process has yet begun at $z = 360$ mm. Accordingly, there is a decrease in overall fluctuation levels from the earlier location to 7.1% (Figure 4.5b) and the overall mean profile again shows no evidence of distortion (Figure 4.5c). The mode shape is much sharper (Figure 4.5e), reflecting the fact that the stationary vortex structure is less developed at this location. However, the peak amplitude of the mode shape is 22%, slightly larger than the upstream location.

The $[15, 60]$ kHz band is more tightly confined to the regions between vortices compared to the upstream location (Figure 4.6a). The maximum amplitude remains nearly unchanged. The $[80, 130]$ kHz secondary instability remains in the same basic location and exhibits a nearly 31% increase in amplitude (Figure 4.6b).

4.4.3 z = 370 mm

At $z = 370$ mm, the mean flow (Figure 4.7a) finally begins to show evidence of substantial mean-flow modification and vortex rollover and the overall fluctuation level has increased to approximately 7.8% (Figure 4.7b). The average mean flow profile shows substantial distortion (Figure 4.7c) and a secondary peak has developed in the much broader mode shape (Figure 4.7e). These two phenomena have been typically associated with the onset of nonlinearity in the mean flow modifications in low-speed flows.

The $[15, 60]$ kHz band has further concentrated itself in the regions between vortices and shifted slightly lower in these troughs with some content also observed along the windward edge of the vortices (Figure 4.8a). The low-frequency mode

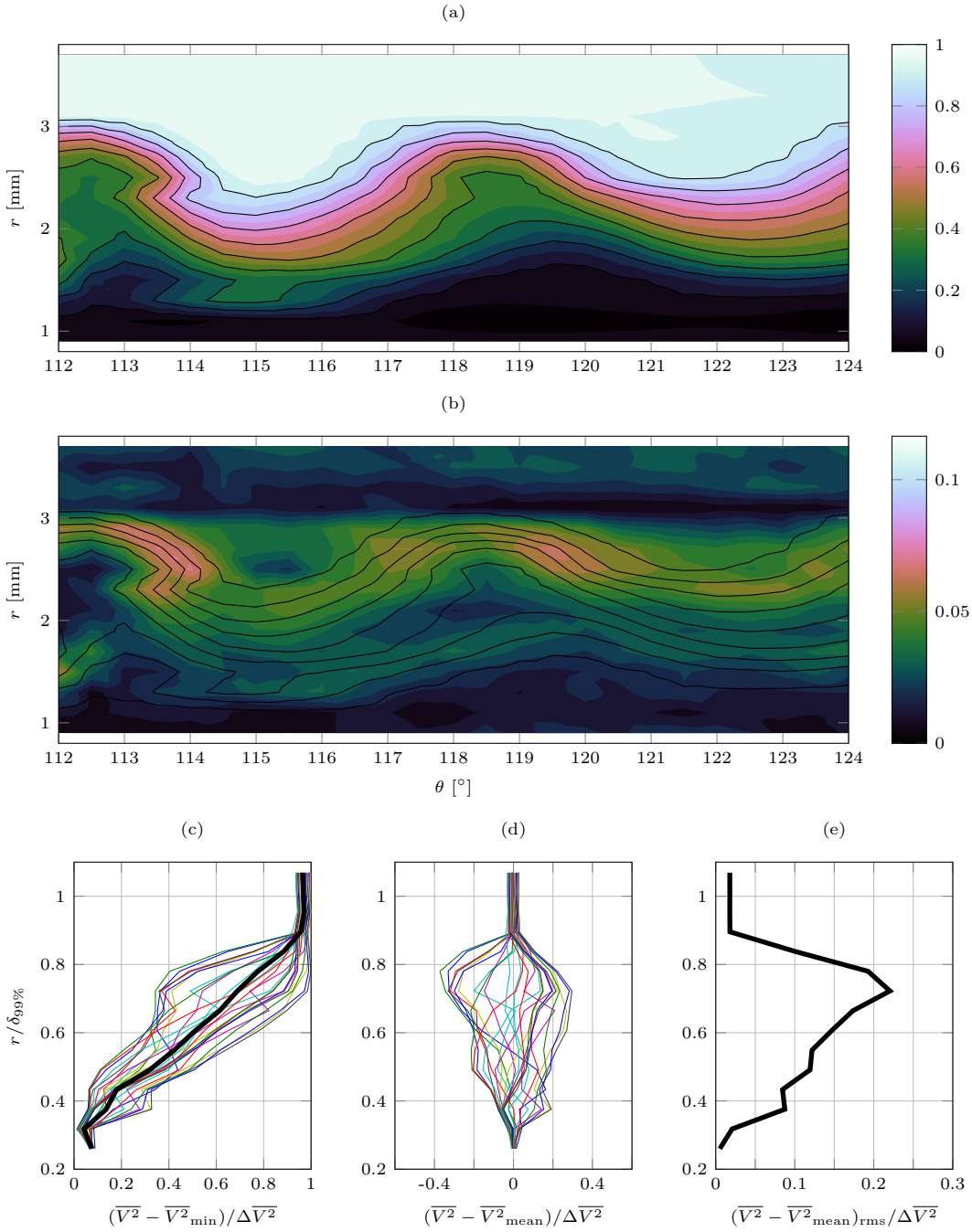

Figure 4.5: Hot-wire data at $z = 360$ mm. (a) Mean flow contour showing contours of normalized mass flux ($\overline{V^2}$). (b) Normalized rms mass flux fluctuation levels ($(V^2)'_{\text{rms}}$) plotted as a fraction of the free-stream value. Contour lines are levels of 10% mean flow. (c) Wall-normal profiles of normalized mean flow, (d) rms mass flux fluctuations, and (e) mean mass flux defect. Thick black lines are the mean of all profiles.

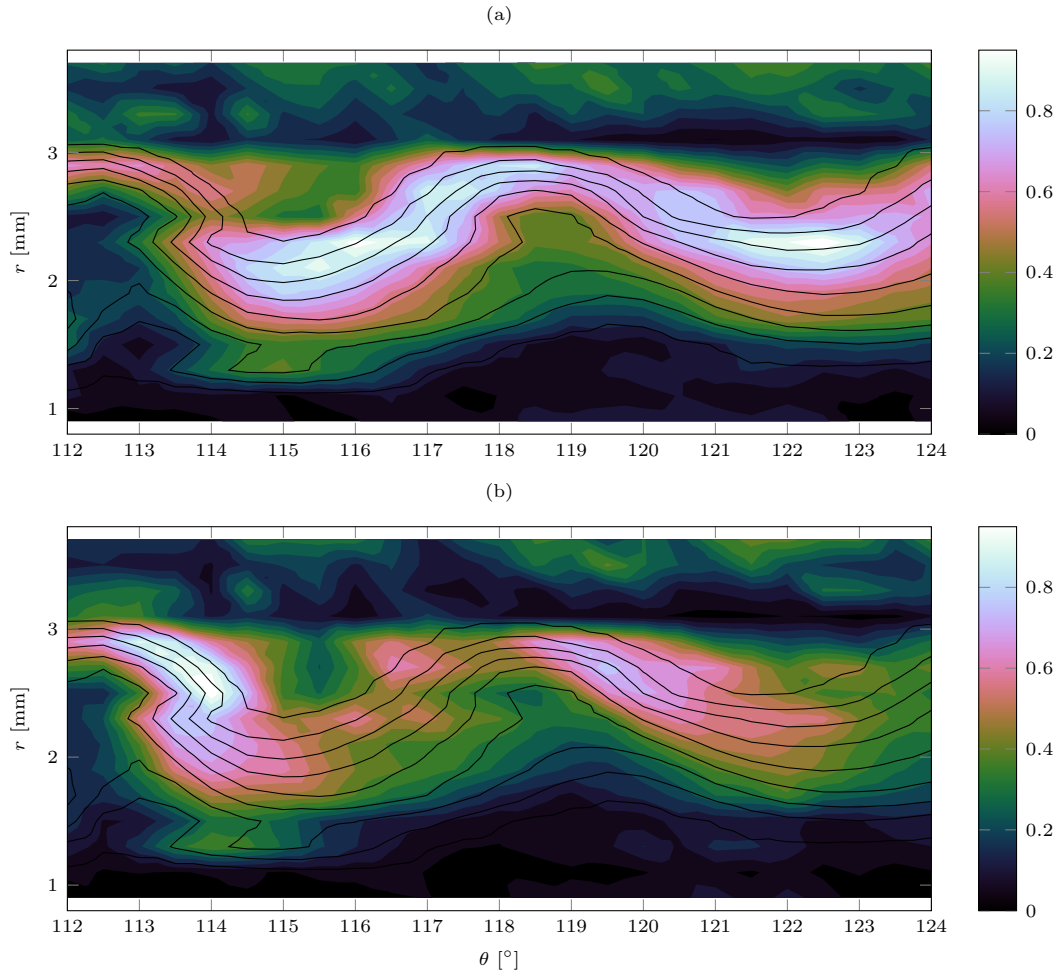

Figure 4.6: Contours of band-passed fluctuation rms at $z = 360$ mm in the bands (a) $[15, 60]$ kHz and (b) $[80, 130]$ kHz. Levels are relative to the maximum fluctuation rms level in each band.

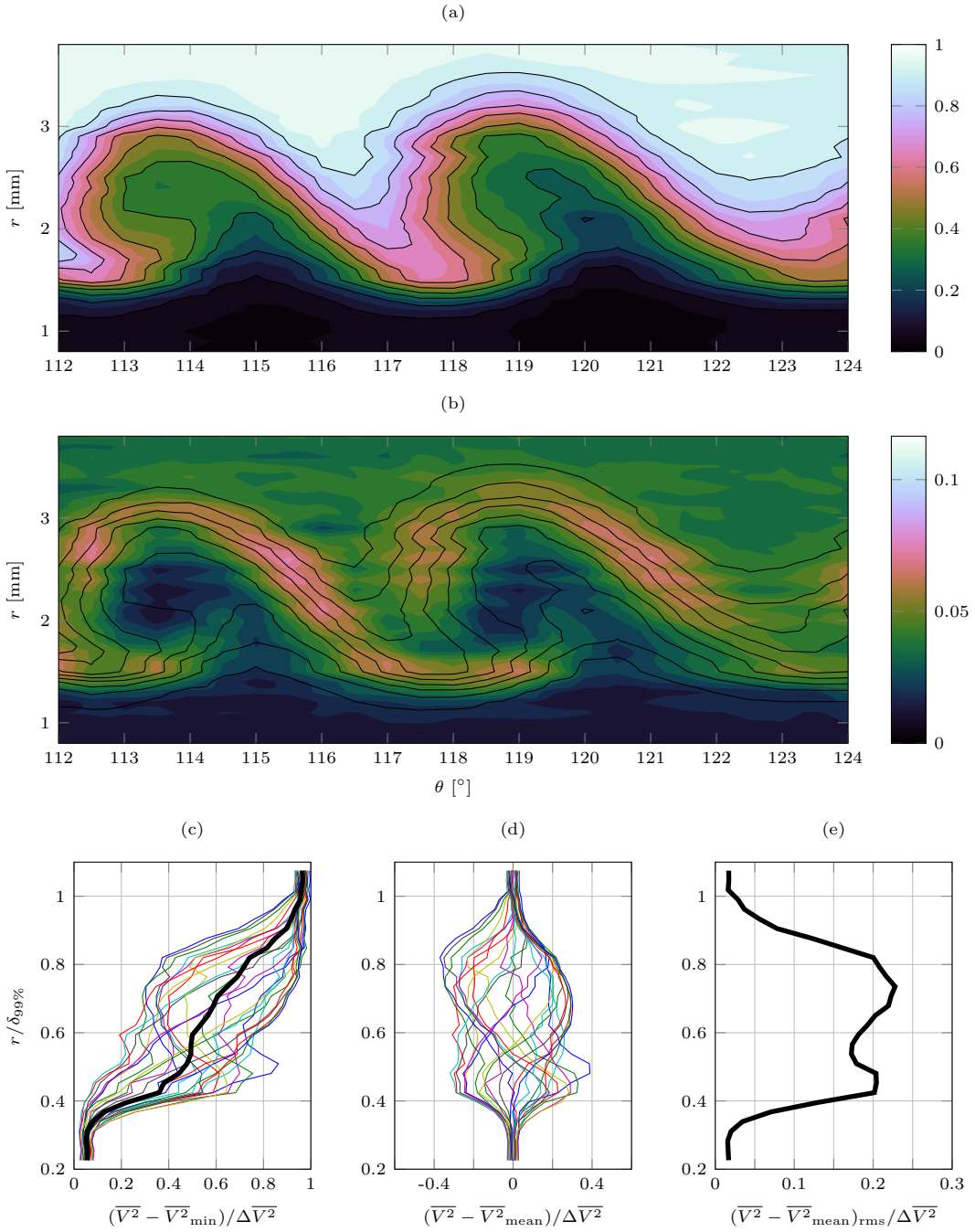

Figure 4.7: Hot-wire data at $z = 370$ mm. (a) Mean flow contour showing contours of normalized mass flux ($\overline{V^2}$). (b) Normalized rms mass flux fluctuation levels ($(V^2)'_{\text{rms}}$) plotted as a fraction of the free-stream value. Contour lines are levels of 10% mean flow. (c) Wall-normal profiles of normalized mean flow, (d) rms mass flux fluctuations, and (e) mean mass flux defect. Thick black lines are the mean of all profiles.

has, by this location, lost approximately 10% of its energy from its initial value at 350 mm. The $[80, 130]$ kHz secondary instability (Figure 4.8b) has grown by about 54% compared to its initial value at 350 mm. The location of this band coincides with the region of greatest overall fluctuation from (Figure 4.7b).

4.4.4 z = 380 mm

The mean flow at $z = 380$ mm shows the beginning of the deterioration of the stationary vortex structure (Figure 4.9a). The high-momentum fluid does not extend as deep into the boundary layer as it had previously. This fact is reflected in the reduced distortion in the average mean flow profile (Figure 4.9c) and the attenuation of the stationary mode (Figure 4.9e), which has broadened slightly while dropping to 18.6% amplitude. The overall fluctuation levels (Figure 4.9b) have once again grown only slightly to 8.1% and are now concentrated almost exclusively between the vortices and in the secondary instability location.

The majority of the $[15, 60]$ kHz band is now located between vortices (Figure 4.10a) and has remained at approximately the same amplitude as at $z = 370$ mm. The $80, 130$ kHz secondary instability (Figure 4.10b) remains in the same location but it's peak amplitude has not grown any further. In fact, while the peak amplitude has remained constant, the spatial extent of the highest-energy region in this band has begun to shrink slightly, no longer stretching to the top of the vortex structure.

4.4.5 z = 390 mm

At the final measurement location, $z = 390$ mm, the stationary vortex structure in the mean flow has continued to degrade (Figure 4.11a), continuing the general trend from $z = 380$ mm. These trends extend to most of the other properties as well. The distortion in the average mean flow profile (Figure 4.11c) continues to decrease and the mode shape (Figure 4.11e) continues to shrink down to 17.6% and

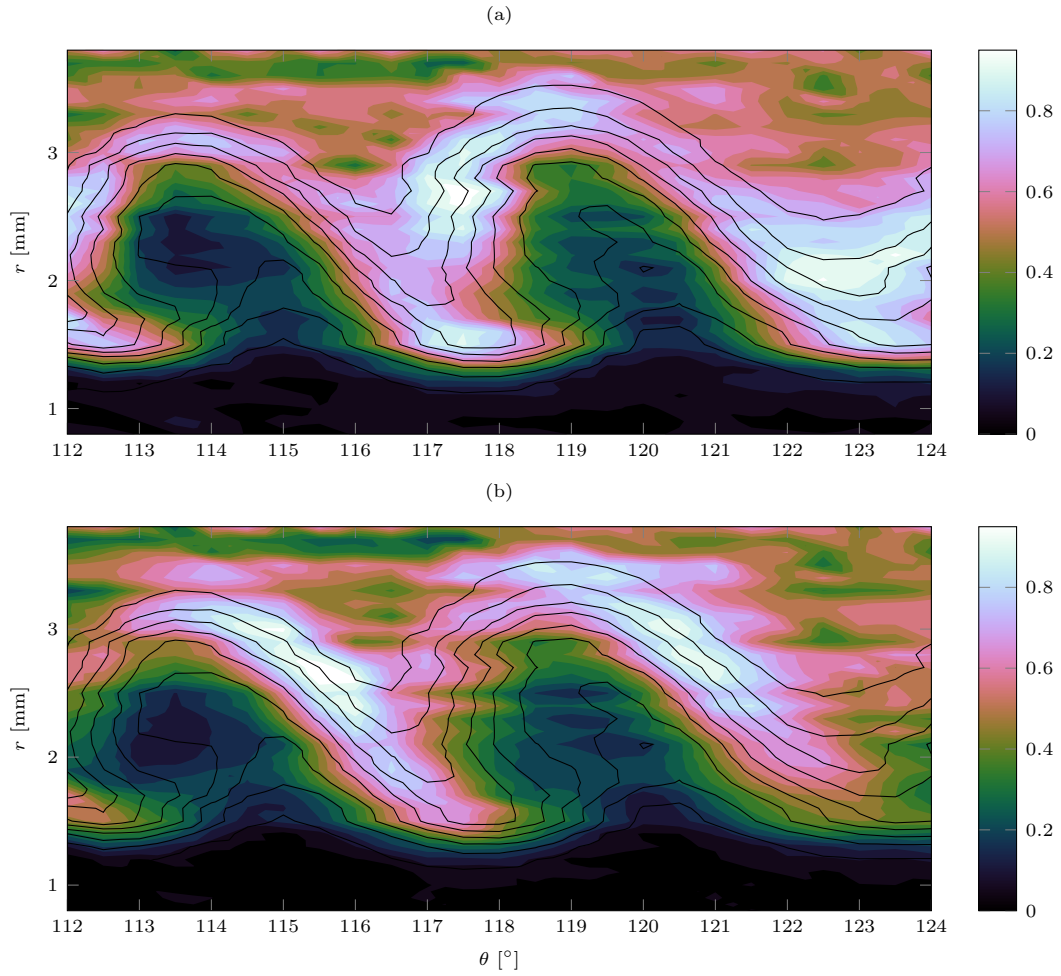

Figure 4.8: Contours of band-passed fluctuation rms at $z = 370$ mm in the bands (a) [15,60] kHz and (b) [80,130] kHz. Levels are relative to the maximum fluctuation rms level in each band.

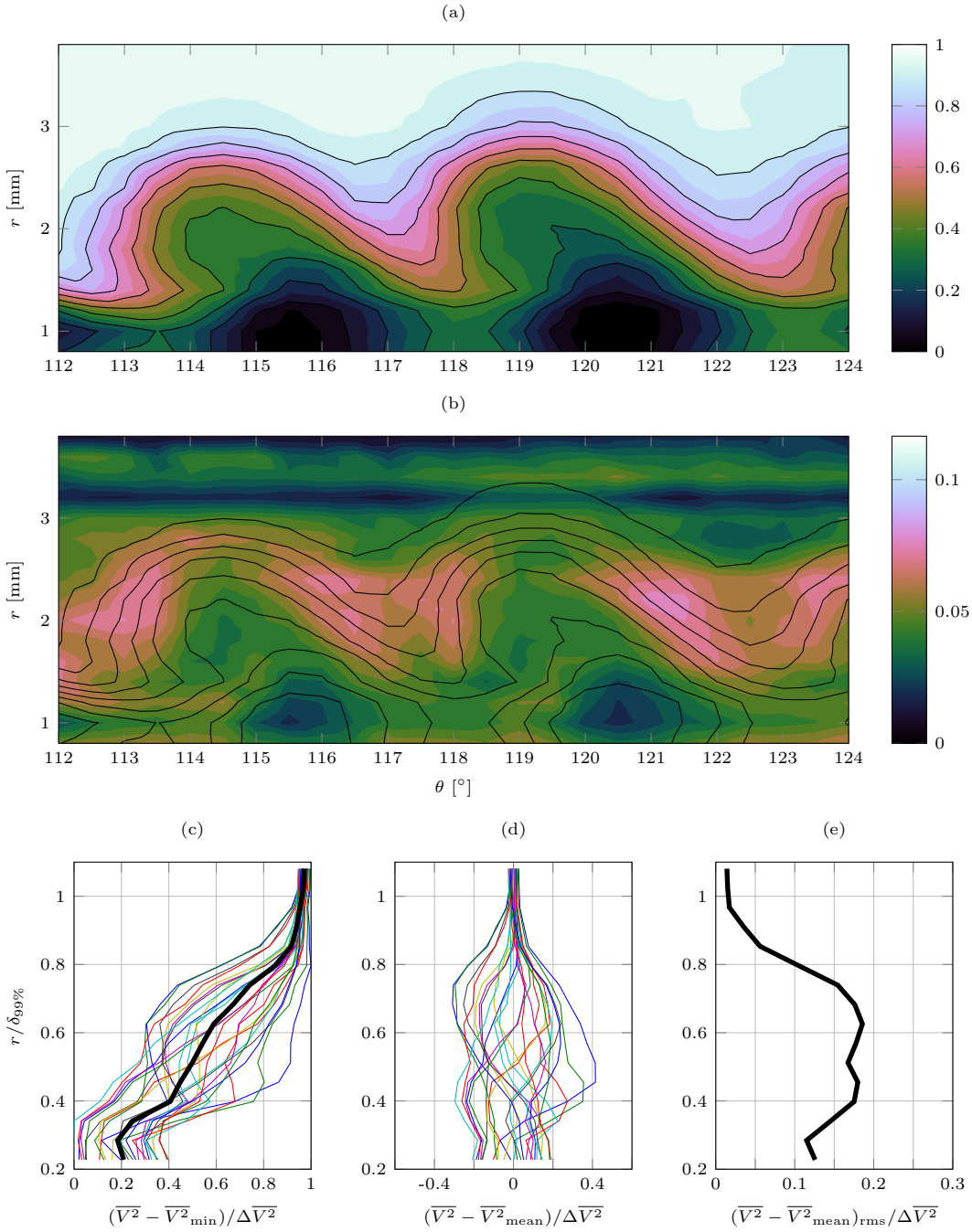

Figure 4.9: Hot-wire data at $z = 380$ mm. (a) Mean flow contour showing contours of normalized mass flux ($\overline{V^2}$). (b) Normalized rms mass flux fluctuation levels ($(V^2)'_{\text{rms}}$) plotted as a fraction of the free-stream value. Contour lines are levels of 10% mean flow. (c) Wall-normal profiles of normalized mean flow, (d) rms mass flux fluctuations, and (e) mean mass flux defect. Thick black lines are the mean of all profiles.

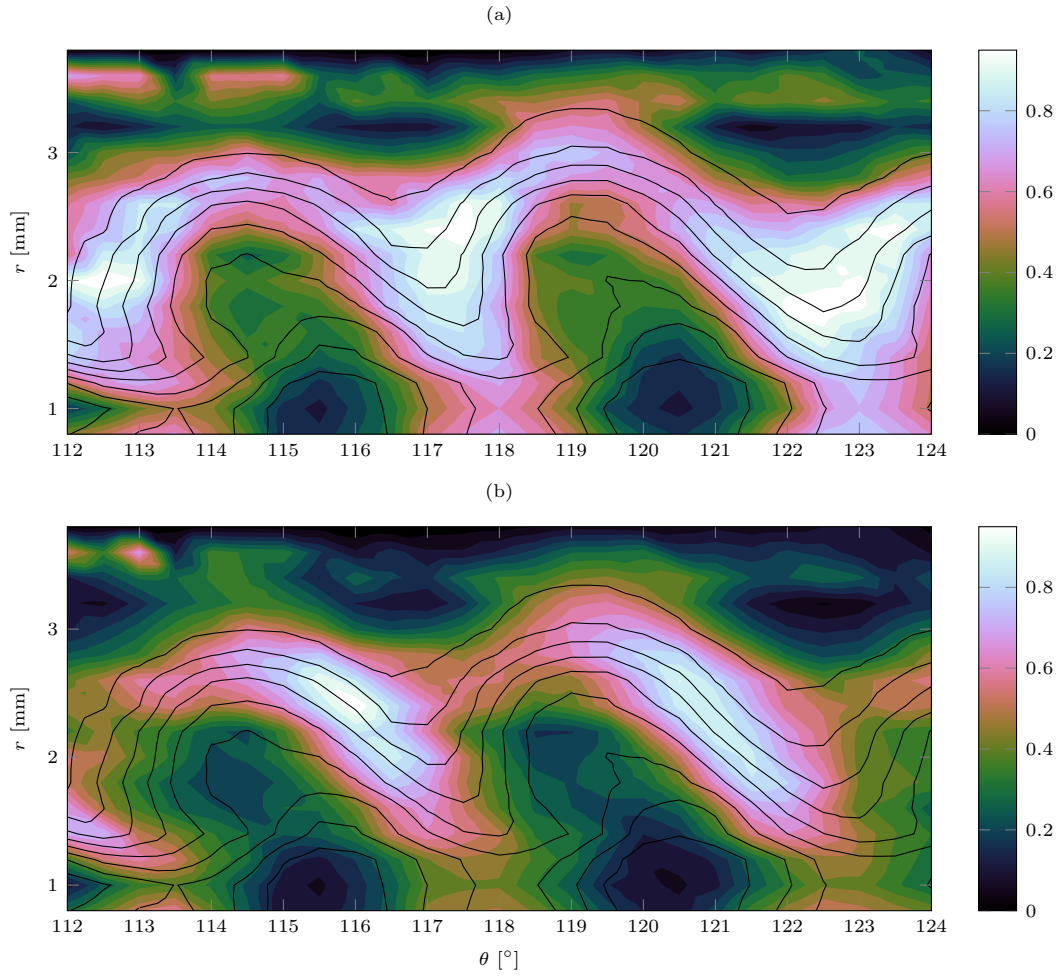

Figure 4.10: Contours of band-passed fluctuation rms at $z = 380$ mm in the bands (a) [15,60] kHz and (b) [80,130] kHz. Levels are relative to the maximum fluctuation rms level in each band.

feature decreasingly prominent peaks. Overall fluctuation levels have begun to fall to approximately 7.8% and the spatial extent of this content is clearly beginning to shrink (Figure 4.11b).

The $[15, 60]$ kHz band continues to be focused in the troughs between vortices (Figure 4.12a) and has continued its slow decrease to 72.7% of its upstream amplitude. The $[80, 130]$ kHz secondary instability (Figure 4.12b) remains in a saturated state at 1.52 times its earlier amplitude and the spatial extent of the high-energy region continues to shrink.

4.5 Traveling crossflow and first-mode waves

Surface pressure measurements made by Muñoz *et al.* (2014) on nearly the same geometry indicated the presence of a broadband peak in approximately the same frequency band as the $[15, 60]$ kHz band in the present experiments. While Muñoz *et al.* identified this peak as being most likely associated with first-mode waves, computations by Kuehl *et al.* (2012) and Reed (private communication) suggest that traveling crossflow waves are the more likely source. Kuehl *et al.* showed that the most amplified traveling crossflow frequencies fall into the range of 20 kHz $\leq f \leq$ 40 kHz, which fits neatly into the $[15, 60]$ kHz band observed in the present experiments.

Further, incompressible experiments have shown that traveling disturbances are concentrated near the base of the vortices and tend to be pulled into the lower portion of the low-speed upwelling (White & Saric, 2005). The behavior in the present experiment partially matches that in the incompressible case, arising primarily near the base of the troughs between vortices. However, while there is no evidence of the $[15, 60]$ kHz content being drawn into the low-momentum upwellings here, this is likely attributable to transonic effects. As the wire moves into the low-momentum upwellings and the Mach number approaches unity, the wire is expected to lose

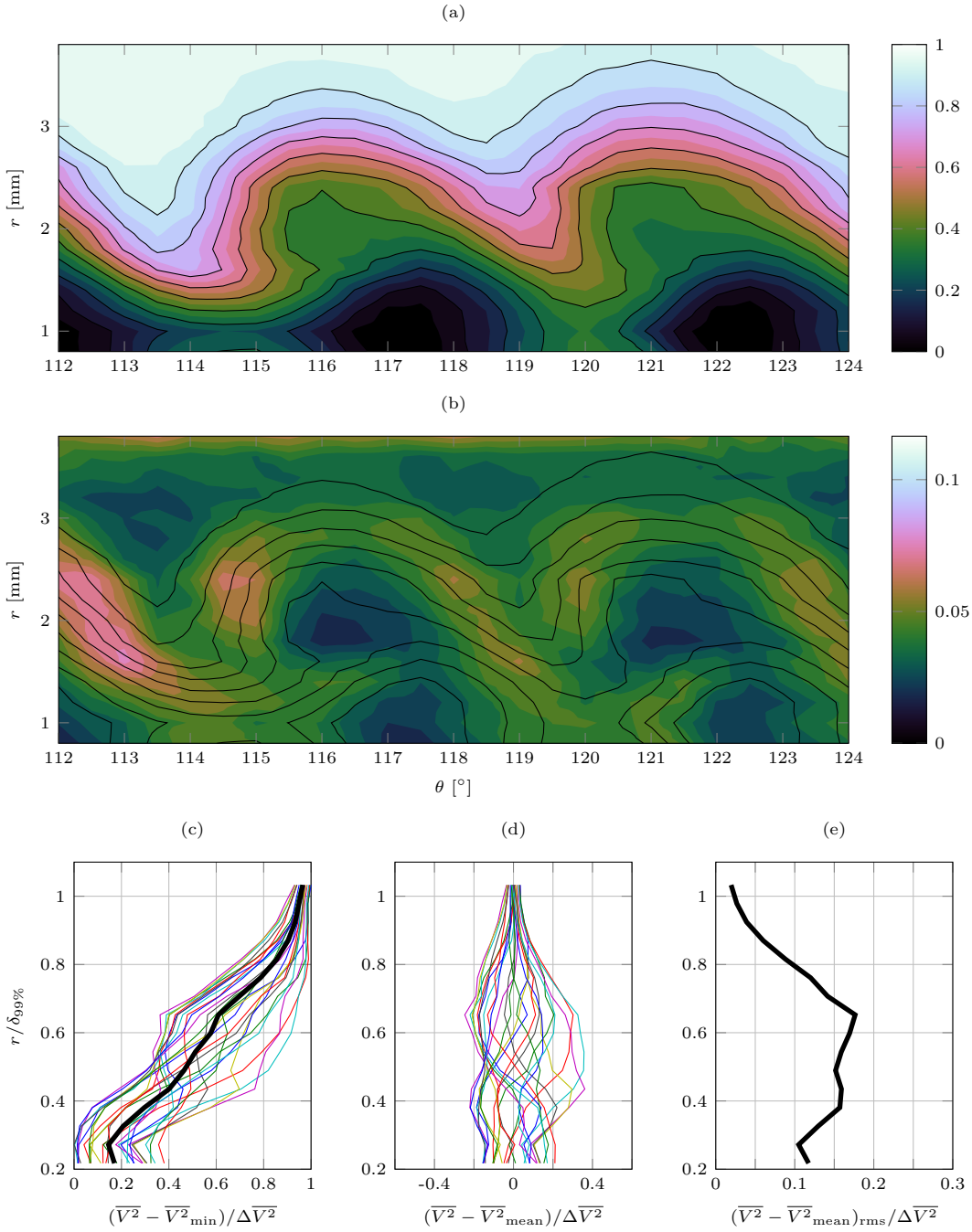

Figure 4.11: Hot-wire data at $z = 390$ mm. (a) Mean flow contour showing contours of normalized mass flux ($\overline{V^2}$). (b) Normalized rms mass flux fluctuation levels ($(V^2)'_{\text{rms}}$) plotted as a fraction of the free-stream value. Contour lines are levels of 10% mean flow. (c) Wall-normal profiles of normalized mean flow, (d) rms mass flux fluctuations, and (e) mean mass flux defect. Thick black lines are the mean of all profiles.

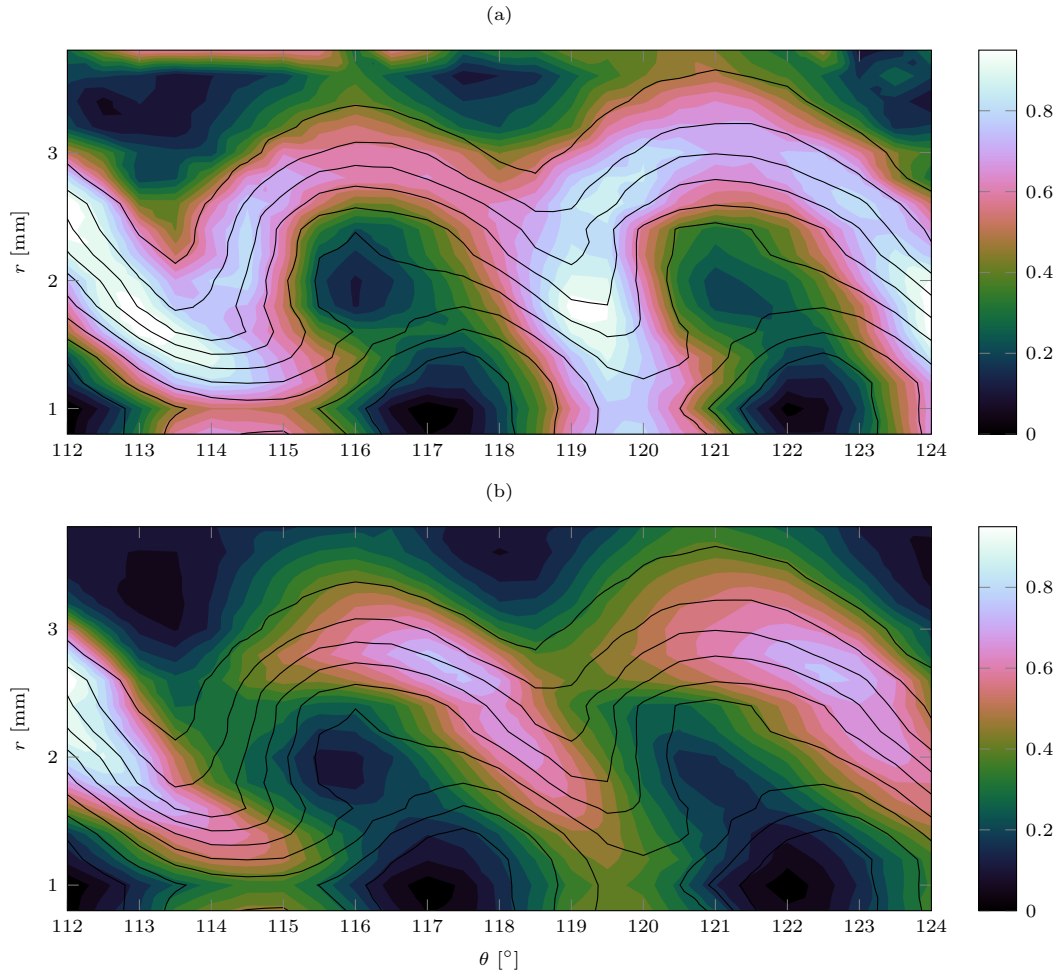

Figure 4.12: Contours of band-passed fluctuation rms at $z = 390$ mm in the bands (a) [15,60] kHz and (b) [80,130] kHz. Levels are relative to the maximum fluctuation rms level in each band.

its tuning, and further, its relative sensitivities to mass flux and temperature are expected to change. As a result, it is likely that the $[15, 60]$ kHz band is a result of traveling crossflow waves, particularly further downstream where the content is exclusively concentrated in the relevant areas.

At some locations, however, particularly early in the development of the stationary structure, there is considerable $[15, 60]$ kHz content higher in the boundary layer concentrated especially in regions of high mass flux gradient. It is therefore possible that this behavior may be explained by the existence of first-mode waves occurring with approximately the same frequency range as the traveling crossflow waves. This content then slowly attenuates further downstream, leaving the traveling wave content between vortices as the only representative of this frequency band.

4.6 Secondary instability

In each location, the $[80, 130]$ kHz band is located along the upper leeward edge of each vortex (for example, Figure 4.8b). This location is in agreement with the expected location for secondary instabilities in incompessible flows (White & Saric, 2005; Bonfigli & Kloker, 2007). The $[80, 13]$ kHz content in the present experiment is therefore expected to indicate the presence of secondary instability.

In order to confirm this suspicion, it is important to consider several facts. Following the nomenclature introduced by (Malik *et al.*, 1996), these secondary instabilities may be of either of two types: type-I instabilities arising from the $\partial(\overline{\rho U})/\partial\theta$ extrema, and type-II instabilities arising from the $\partial(\overline{\rho U})/\partial r$ extrema. Figure 4.13 depicts the band-passed contour of the $[80, 150]$ kHz content overlaid onto a surface representing the gradients. The upstream location of $z = 360$ mm since this is near where this frequency band appears to originate. The areas of high concentration of the $[80, 130]$ kHz energy coincide one-to-one with the regions of high $\partial(\overline{\rho U})/\partial\theta$ (Figure 4.13b), which is

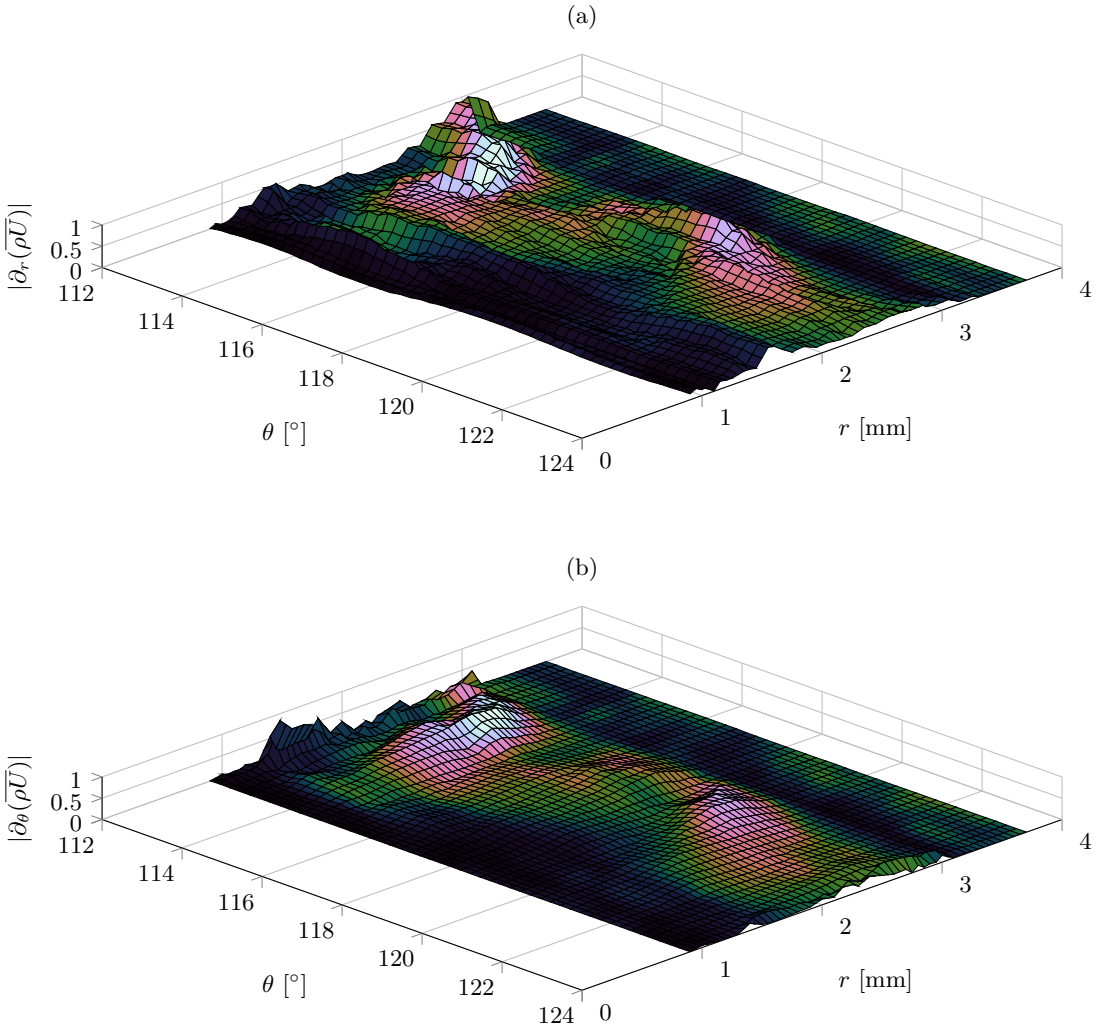

Figure 4.13: Contour of band-passed fluctuation rms at $z = 360$ mm in the bands [80,130] kHz overlaid surfaces representing (a) $\partial(\overline{\rho U})/\partial r$ and (b) $\partial(\overline{\rho U})/\partial\theta$.

the forcing mechanism for crossflow. While there is also some overlap with $\partial(\overline{\rho U})/\partial r$ peaks (Figure 4.13a), this appears to be largely coincidental, as there are regions with large r gradients without substantial energy in this band.

Incompressible studies have shown that the type-I secondary instability of stationary crossflow waves is a convective instability with a frequency proportional to U_e/δ. Based on the work of White & Saric (2005), the expected frequency for a type-I secondary instability dominated by $\partial U/\partial\theta$ would be roughly $f \approx U_e/(2\delta)$. Using the same scaling relationship with the relevant values from the present experiment, the predicted frequency falls in the vicinity of 120 kHz, right in the upper range of the $[80, 130]$ kHz band. The type-II instability exhibited a frequency approximately (but not exactly) twice that of the type-I instability.

It therefore is apparent that the $[80, 130]$ kHz energy, at least initially, represents a type-I secondary instability. As the flow develops downstream, the energetic region in this band convects up and around the top of the vortices slightly, drifting into regions dominated by the r gradient. Unsurprisingly, this appears to coincide with the saturation location for the secondary instability. While it is possible that a type-II instability coexists with the type-I instability in these locations, the expected frequency range is greater than the frequency response of the hot wire (assuming that the subsonic frequency scaling is as valid for type-II instability as it is for type-I in this case).

4.7 Mode growth and interaction

4.7.1 Mode growth and saturation

The growth of each of the three modes (traveling wave, secondary instability, and stationary wave) is plotted in Figure 4.14 as a fraction of each mode's initial amplitude. Even the secondary instability, which is the most amplified mode in the measurement

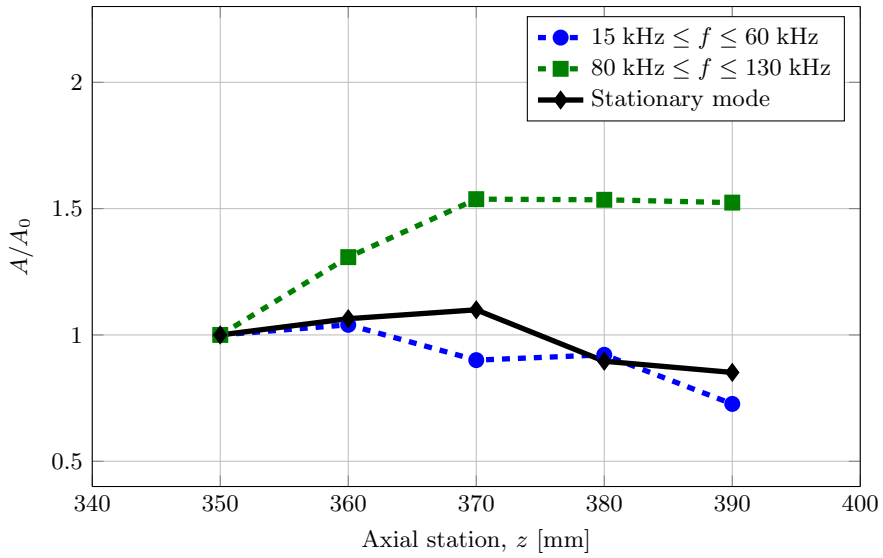

Figure 4.14: Growth in amplitude of both unsteady and stationary modes.

domain, achieves only a 50% increase in amplitude over a 40 mm distance. The same type-I instability was amplified by a factor of over 100 (Figure 4.15) on an incompressible swept wing (White & Saric, 2005) before breakdown, and only then did it show signs of saturation.

However, it is interesting to note that White & Saric (2005) did observe the existence of the type-I secondary instability at nearly constant amplitude over a distance of approximately 20 mm before observing the explosive growth leading to breakdown. Further, they observed a slight drop in the amplitude of the traveling wave and the saturation and slight attenuation of the stationary wave in the same region. It is therefore plausible that the present data set captures the type-I mode in this early stage prior to its explosive growth and that the spatial extent of this regime is simply extended compared to the low-speed swept wing as a result of the substantially higher edge velocity. Figure 4.15 is a modified reproduction of Figure 18 from White & Saric. The dashed box highlights the region of that data set for which

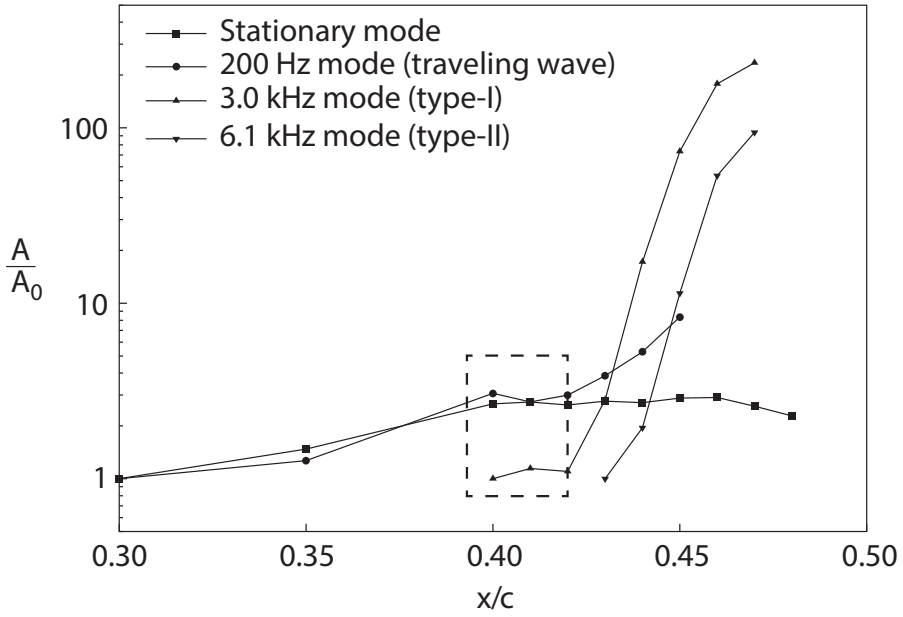

Figure 4.15: Crossflow mode growth in an incompressible, swept-wing boundary layer with spanwise-periodic discrete roughness elements. Modified from White & Saric (2005). Dashed box marks proposed analogous region to the present study.

the present data set may be an analogue.

4.7.2 Nonlinear interactions

The possibility remains that there is a fundamental difference in the growth of the secondary instabilities in a hypersonic boundary layer as compared to the incompressible case and that the secondary instability may actually reach saturation at this point. It is therefore interesting to explore the possibility of interaction between the traveling wave and the secondary instability as a source of the saturation behavior. Accordingly, the point at each z location that featured the largest colocated combination of each of the two unsteady modes was determined and the normalized, squared bicoherence of the signal was computed. See Appendix A for further detail

on bispectral analysis.

Figure 4.16 depicts contours of the normalized, squared bicoherence for two axial locations, $z = 370$ mm and $z = 380$ mm. These two locations were chosen because the contours at all other locations were uniformly approximately zero where a value of 1 would indicate perfectly coupled waves and a value of 0 would indicate two completely independent waves. A peak located at (f_1, f_2) implies an interaction between waves at f_1 and f_2 resulting in excitation at $f_1 + f_2$. As such, an interaction between waves in the two unsteady bands in the present study would tend to excite content in the range $95 \text{ kHz} \leq f_1 + f_2 \leq 190 \text{ kHz}$. The frequency response of the wire causes the signal to drop below the noise floor for frequencies higher than $f \approx 200$ kHz, so only data lying inside the dotted lines in Figure 4.16 should be considered meaningful. Since any combination of $f_1 + f_2$ for the bands of interest here result in $f_1 + f_2 < 200$ kHz, the analysis is capable of detecting the interaction should it exist.

While there are regions of broad, low-amplitude peaks near the upper tip of each of the two contours, neither of these include peaks in a region that indicates an interaction between the traveling wave and the secondary instability. The broad excited region instead lies in an area that indicates a wave of $f_1 \approx 180$ kHz interacting with frequency content in a neighborhood around itself, $f_2 = f_1 \pm \delta f$, where δf is around 20 kHz to 30 kHz. This would hint at the presence of another unsteady mode in the boundary layer. However, upon inspection, the frequency band in the vicinity of 180 kHz did now exhibit any type of discernable spatial coherence. Instead, 180 kHz is at the upper limit of the CTA frequency response and the low peak in the bicoherence is more likely a result of the dwindling signal-to-noise ratio.

There is a peak reaching as high as 0.3 near the origin of Figure 4.16b and stretching along the left edge of the contour where $f_2 \approx -f_1$. These interactions indicate mean flow distortion as a result of self-excitation of the traveling waves.

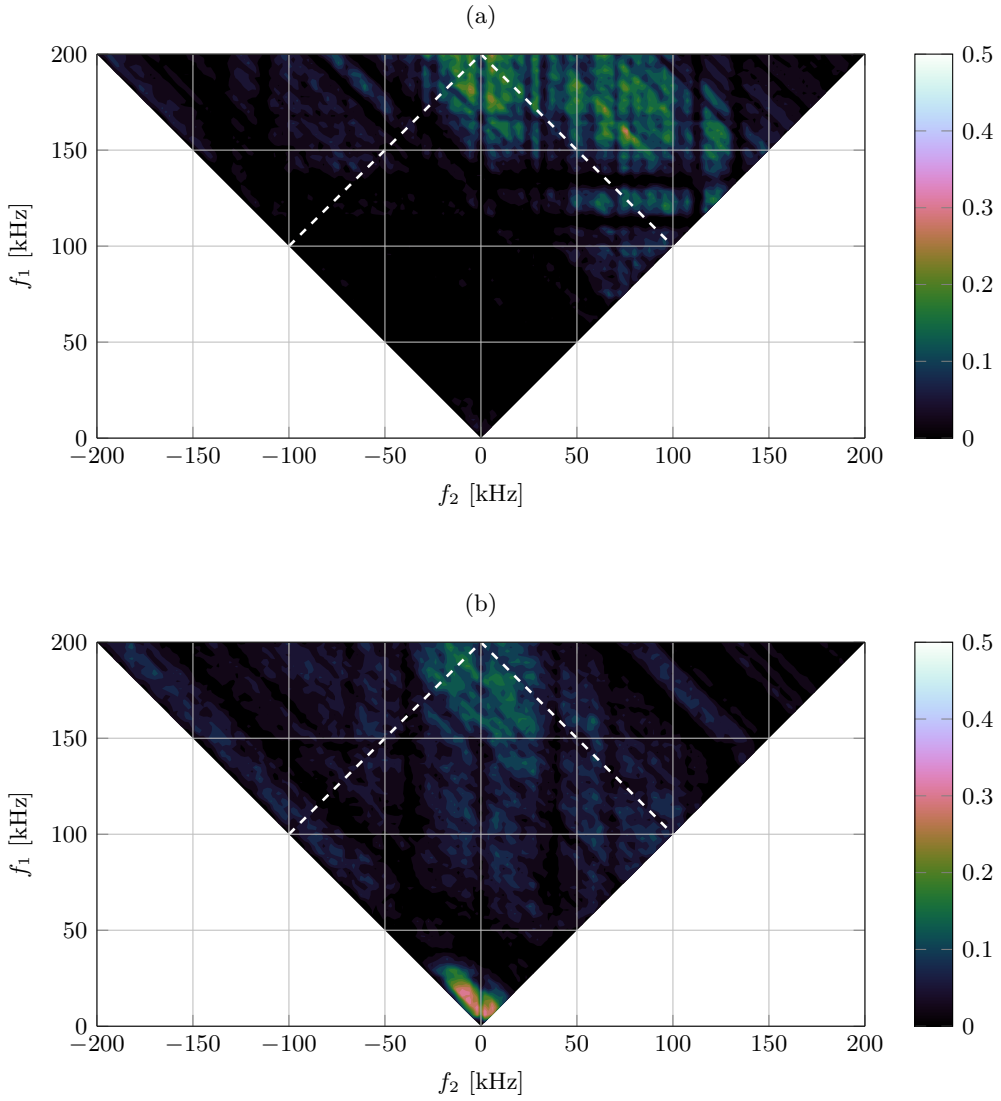

Figure 4.16: Normalized, squared bicoherence plots at (a) $z = 370$ mm and (b) $z = 380$ mm.

However, substantial mean-flow distortion exists at every axial station and this peak was not observed at any other location. The exact physical nature of this peak therefore remains uncertain.

5. RESULTS: DISTRIBUTED ROUGHNESS ON A YAWED CONE

5.1 Overview

Laminar-turbulent transition was not observed at any quiet-flow Reynolds number on the polished cone (see § 4). In order to encourage transition, several methods for increasing the initial disturbance amplitude were considered. The goal of this approach was that the larger initial amplitude would grow large enough to observe breakdown within the spatial constraints of the wind tunnel.

The first of these options was the use of DREs to preferentially excite one or more of the most unstable wavenumbers. The targeted wavenumber, known to be highly unstable, would then theoretically grow rapidly toward breakdown. However, in order for DREs to be most effective, they must be located near branch-I neutral point for the targeted unstable wavenumber and spaced and sized accordingly. While several studies have taken this approach by placing DREs around the azimuth of the cone at constant azimuthal spacing with moderate success (Schuele *et al.*, 2013; Ward, 2014), this approach is not optimal.

Unlike the case of a swept wing, where the neutral point is represented by a line of constant chord extending along the span near the leading edge, the neutral point on a yawed cone is not a ring around the cone at constant axis. Instead, for a given wavenumber, the neutral point is a curve near the windward attachment line. Further, the wavelength associated with a given number is not constant along the neutral curve as it is for a swept wing. As such, designing an optimal set of DREs requires consultation with computational studies. These computations are ongoing with the goal that an optimal set of DREs may be produced in the near future.

Instead the present study opts for using distributed roughness on the surface

of the cone forebody (see § 2.2.3.2). The distributed excites a broadband set of disturbance wavenumbers In the vicinity of the neutral point and a short distance along the path of the crossflow vortices. While this approach will excite many modes, the random nature of the roughness ensures that it does not preferentially excite any modes whose dominance would preclude the growth of the most unstable modes. As such, all wavenumbers in the excited band will have a larger initial amplitude and the most unstable modes are still expected to grow most rapidly.

5.2 Operating conditions

The run process for the rough-tip experiments largely mirror those of the smooth-tip case (§ 4.2). The primary difference is that runs were performed at a number of total pressures resulting in runs at a range of Re' spanning roughly $6 \times 10^6/\text{m} \leq Re' \leq 6.5 \times 11^6/\text{m}$. Total temperature was still held at $T_0 \approx 430$ K for all runs with the same wall temperature conditions as the previous campaign for all hot-wire measurements. IR thermography was more heavily utilized in this campaign, and each of these runs utilized the unheated surface to improve contrast.

5.3 Infrared flow visualization

As an exploratory study, the flow over the rough tip was more efficiently investigated using IR thermography to help guide future hot-wire measurements. Once again, IR thermography was made possible on the reflective model through the application of of the same size as that reported in § 4.3.

Initial tunnel runs were performed at the two previously explored Re' conditions of $10.0 \times 10^6/\text{m}$ and $11.0 \times 10^6/\text{m}$ in order to facilitate comparison with previous measurements. The results for these two conditions are shown in Figure 5.1. Aside from the bubble in the tape at the bottom of the $Re' = 10 \times 10^6/\text{m}$ image, Figure 5.1 shows only a near-uniform surface temperature and no evidence of crossflow.

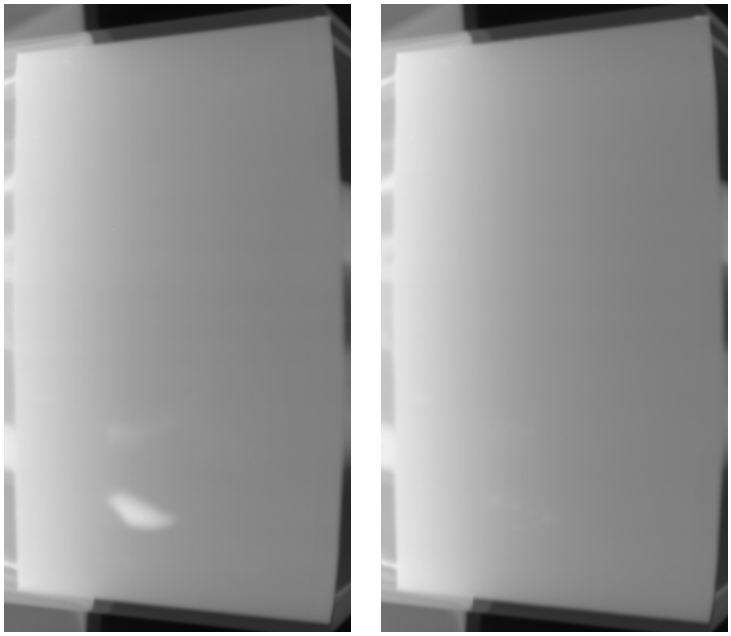

Figure 5.1: Initial IR thermography on the TAMU 7DC with rough tip. Left to right: $Re' = 10 \times 10^6$/m, $Re' = 11 \times 10^6$/m. Images are looking down on the leeward attachment line of the cone (vertically centered). Flow is left to right.

To explore a wider range of Re', several runs were performed where the tunnel was started and the pressure slowly swept. The IR camera's shutter was synchronized with the sampling of tunnel conditions. As the pressure was swept, a data point and corresponding IR image were recorded at 10 Hz. Each run therefore produced anywhere from 200 to 400 images at a known Re'. A sample of these images is presented in Figure 5.2 ranging from $Re' = 6.5 \times 10^6$/m to $Re' = 10.0 \times 10^6$/m.

While it is clear that there are stationary streak structures at the four lowest Re' conditions, at $Re' = 8.5 \times 10^6$/m the streaks are very faint and by $Re' = 9.0 \times 10^6$/m they are gone entirely and the flow resembles that in Figure 5.1. It is therefore apparent that the boundary layer becomes turbulent somewhere just above $Re' = 8.5 \times 10^6$/m and all streak structures rapidly disappear.

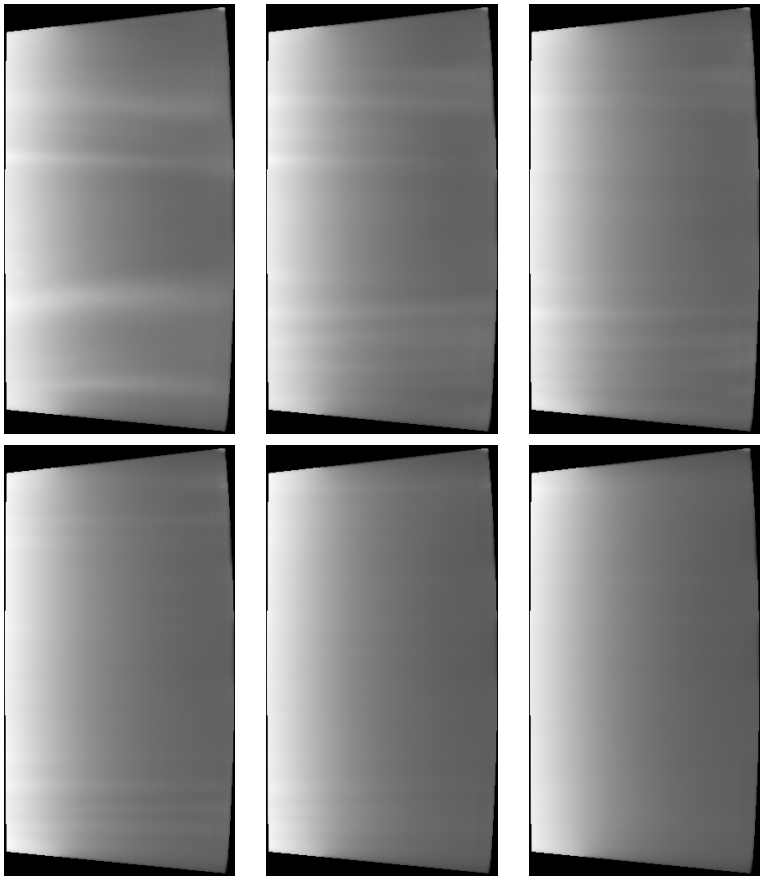

Figure 5.2: IR thermography on the TAMU 7DC with rough tip. Top row, left to right: $Re' = 6.5 \times 10^6$/m, $Re' = 7.0 \times 10^6$/m, $Re' = 7.5 \times 10^6$/m. Bottom row, left to right: $Re' = 8.0 \times 10^6$/m, $Re' = 8.5 \times 10^6$/m, $Re' = 9.0 \times 10^6$/m. Images are looking down on the leeward attachment line of the cone (vertically centered). Flow is left to right.

At $Re' = 6.5 \times 10^6$/m (corresponding to $p_0 \approx 85$ psia), the streaks are large and irregularly spaced. It is therefore believed that these streaks at low Re' are the result of a wake from particularly large spots of roughness or transient growth. With the current model and traverse installation, the tunnel requires $p_0 \approx 100$ psia to start initially and unstarts during a downward pressure sweep in the vicinity of this test point.

However, the streaking does bear some similarity to the IR images depicting crossflow on the smooth cone for the image in the range $7.0 \times 10^6/\text{m} \leq Re' \leq 8.5 \times 10^6/\text{m}$. The images in Figure 5.2 have had their black levels scaled for additional contrast, as the streaks are more faint in appearance than those on the smooth cone (Figure 4.2). Still, the streaks exhibit a remarkably regular magnitude and spacing as would be expected of those caused by stationary crossflow vortices.

5.4 Hot-wire measurements

As the primary goal of the roughness is induction of a crossflow-dominated breakdown to turbulence, the streak structures observed in the middle of the Re' range in Figure 5.2 bear further investigation, particularly as Re' nears the level at which breakdown is observed. As a result, several azimuthal hot-wire scans were made near the expected transition Re'. Figure 5.3 depicts two such scans at Re', $7.8 \times 10^6/\text{m}$ and $10.0 \times 10^6/\text{m}$. Both profiles were taken at a constant height of 2.5 mm from the wall where secondary instabilities are expected to occur in a laminar boundary layer at this location.

The $Re' = 7.8 \times 10^6/\text{m}$ profile shows a smooth, nearly sinusoidal variation in hot-wire voltage over the azimuthal range, the amplitude of which spans a sizable potion of the total boundary-layer $\Delta\overline{V^2}$. The Range of about 0.1 to 0.9 indicates that the measurement height went nearly through the center of the vortex structure, capturing displaced low-momentum and high-momentum regions. The wavelength is considerably larger than the smooth-wall crossflow waves at approximately 10°, but this is not entirely unexpected given that roughness results in a dramatically different initial disturbance than in the smooth-wall case. Upon increasing Re', profile flattens almost completely, bearing little evidence of azimuthal variation. Further, the relatively small variation that does exist can be largely explained by a thickening

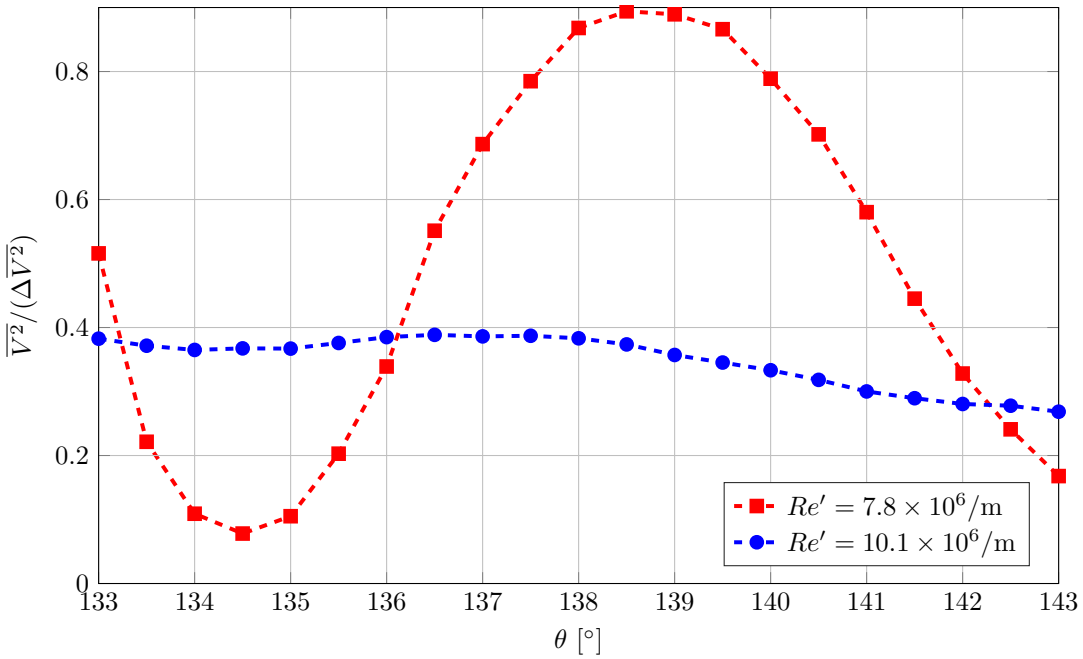

Figure 5.3: Azimuthal boundary layer scans with the rough tip. Values are normalized by each condition's respective free-stream $\overline{V^2}$.

boundary layer in the positive θ direction due to the yaw.

Figure 5.4 depicts two axis-normal profiles at the location of the previous azimuthal measurements and sheds light on the nature of the difference in the azimuthal profiles. At $Re' = 7.8 \times 10^6$/m, $\delta \approx 3$ mm, while at $Re' = 10.0 \times 10^6$/m, a reasonable estimate of δ is not possible, as the measurement range did not capture the full boundary layer ($\delta > 6$ mm). The lower overall voltage in the high-Re' case from Figure 5.3 is clearly due to the fact that the boundary layer is considerably thicker at this condition than the low-Re' case. It is therefore apparent that the boundary layer has transitioned to turbulence as a result of the increased Re'. The very low fluctuation levels ($< 1\%$) in the low-Re' case, where the boundary layer is expected to at least be at the early stages of transition based on Figure 5.2, indicate that it is unlikely that the observed

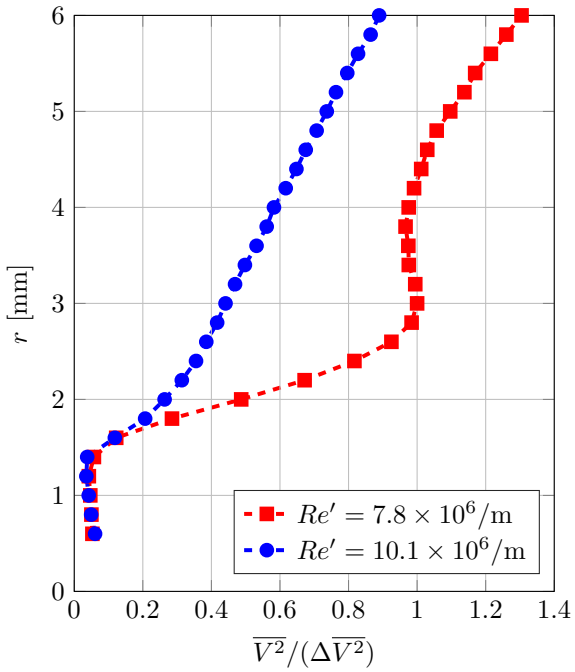

Figure 5.4: Axis-normal boundary-layer profiles with the rough tip. Values are normalized by each condition's respective free-stream $\overline{V^2}$.

transition was caused by the breakdown of crossflow vortices.

Considering the above evidence, the likely explanation for the observations is as follows. The distributed roughness is preferentially exciting crossflow waves of $\lambda \approx 10°$ ($k_c \approx 36$). This wavenumber is expected to be substantially more stable than the naturally-occurring $k_c \approx 60$. The initial amplitude of this excitation, while higher than the natural baseline, appears to be small enough that the downstream amplitude is below that required for breakdown as evidenced by the low fluctuation levels and the relatively faint IR streaks. The breakdown observed at higher Re' is therefore not likely to be crossflow-dominated, and is instead the result of some other mechanism.

Measurement of the step size from the roughness onto the smooth cone at the

downstream interface revealed that the step, k fell in the range $0 \leq k \leq 1$ mm. The majority of the interface fell approximately into the range 300 µm $\leq k \leq$ 500 µm. This corresponds to $Re_{kk} = O(10^4)$ at the location of maximum step size and $O(10^2) \leq Re_{kk} \leq O(10^3)$ for a large portion of the interface. These values of Re_{kk} are well above those observed to cause transition directly on low-speed swept wings by Duncan, Jr. (2014) and Crawford (2015).

6. CONCLUSIONS AND FUTURE WORK

6.1 Conclusions

6.1.1 Mack-mode breakdown

One of the objectives of this study was the investigation of the breakdown characteristics of the Mack mode. In particular, numerical evidence Sivasubramanian & Fasel (2012*a*,*b*) has shown that the breakdown mechanism is three-dimensional in nature and bears remarkable similarity to the breakdown of Tollmien-Schlichting waves first observed by Klebanoff *et al.* (1962). Mack-mode breakdown does not occur naturally under conditions achievable in M6QT (Hofferth, 2013) due to the small initial disturbance amplitudes and the relatively slow spatial growth of Mack-mode waves. To counter this, the application of roughness near the tip is required to provide larger initial amplitudes for the relevant modes. This objective was not achieved during the present study. However, the pursuit of this goal led to several important developments.

A new, azimuthal traversing mechanism was designed for investigation of such three-dimensional phenomena. This system allows greater than 180° of travel around an axisymmetric model such as a cone. The traverse is fixed to the model axis, and as such, may be placed at nonzero angle of incidence to the flow along with the model, enabling a number of experiments that were previously impossible in M6QT. This system is compatible with a number of types of probes, including hot wires and Pitot tubes.

Additionally, a new method of producing DREs was developed. The water slide decal method offers several advantages over the dry transfer method, the previous state of the art. The vinyl decals are more durable and easily hold up under the heat

of a tunnel run (a test batch applied to the vertical support mounting support has been in place for over 400 runs). Further, the wetted decals can be easily slid across a surface for alignment without any damage. The finished roughness elements can also be safely wiped with water and handled by hand. These decals have been printed in a number of thicknesses ranging from 10 μm to 30 μm and may theoretically be printed much thicker with some additional development.

6.1.2 Natural crossflow

The next primary objective of these experiments was a detailed study of the natural growth of crossflow waves in a hypersonic boundary layer. To this end, CTA measurements were made at several axial locations on a right, circular cone model designed specifically for the study. The model included an internal heating system to help enforce an adiabatic wall, a point of weakness in some previous experimental studies. Contours of mean and fluctuating CTA voltage (approximately proportional to mass flux) were created at five axial locations and the growth of the instability was tracked over that extent.

It was observed that the dominant stationary crossflow wavenumber and the dominant traveling wave frequency were accurately predicted by linear theory in the form of LPSE computations. Linear theory is not expected to accurately predict the growth rates in this region, however, as the disturbance has clearly become nonlinear. The accuracy of NPSE calculations in this case remains unaddressed pending forthcoming computations.

Additionally, the structure and behavior of the crossflow instability in a hypersonic boundary layer bears striking resemblance to its low-speed, extensively-studied counterpart:

- The stationary wave saturates at nearly the same amplitude as the low-speed

case, then begins to slowly lose amplitude.

- Traveling wave energy is concentrated in the regions between the upwellings caused by the stationary wave.

- Nearing saturation portends the development of a type-I secondary instability in the region dominated by the azimuthal gradient.

- The frequency of the type-I secondary instability obeys a similar scaling law to the low-speed case: $f \approx U_e/(2\delta)$.

The present study appears to capture a point in the growth of the crossflow instability that very closely matches (qualitatively) the middle measurement region in White & Saric (2005) as highlighted in Figure 4.15. The rapid growth of the secondary instability expected just downstream of this region was never observed. While this region may still exist on the model in question, it is unlikely that the ensuing transition occurs based on IR images of the region.

No evidence of nonlinear interaction was observed between the traveling wave and the secondary instability. However, this technique was somewhat limited by the frequency response of the wire and could not capture, for example, self-excitation of the secondary instability.

6.1.3 Breakdown of crossflow vortices

High-amplitude distributed roughness was applied to the cone tip in an effort to provide an increased initial disturbance amplitude and encourage boundary-layer transition on the model. While it was apparent that transition was achieved using this method, evidence suggested that this transition was not dominated by the crossflow instability.

The probable explanation for this appears to be that the roughness, while intended to provide a broadband disturbance, primarily excited a more stable wavenumber than the naturally-dominant wave. The less stable wave never reached sufficient amplitude to undergo transition, and likely remained at a smaller amplitude than the the previously-measured natural crossflow. Meanwhile, the roughness appeared to have excited another instability mechanism, possibly transient growth, which ultimately led to breakdown.

6.2 Future considerations and recommendations

While this study did provide the first extensive measurements of crossflow waves in a hypersonic boundary layer, a number of questions remain open and a number of new questions have arisen. The experiences gained during the course of these experiments have provided a great deal of insight into new approaches to answering these questions.

6.2.1 Mack-mode breakdown

While the breakdown of Mack-mode waves was not achieved in the present experiments, much was learned about how to achieve this goal in M6QT. The most promising approach is that of wall cooling combined with the input of a controlled disturbance. The LaRC 93-10 should be adapted to work with the existing cooling system, allowing cold-wall experiments on an extensively-studied geometry. DREs should also be applied in the same manner as the experiment detailed herein.

Should this approach fail to achieve the breakdown of Mack-mode waves, a new model would be required. A flared "compression cone" is a promising approach for maximizing the Mack-mode N-factor for a given Re'. Such a design would be flared nearly up to the tip, creating an adverse pressure gradient over nearly the entire length of the model. This approach could be potentially maximized by tailoring the

flare to produce a boundary layer of near-constant thickness.

6.2.2 Future crossflow experiments

While successful overall, the crossflow experiments did not succeed in documenting the rapid growth of the secondary instability, likely leading to transition. Further experiments are warranted with this goal. In the present configuration, the distance of travel for each crossflow wave did not cover the length of the cone, but instead a much shorter curve from the 0° ray line to the 180° ray. Therefore, achieving breakdown in M6QT is not likely through the growth of naturally-occurring crossflow waves alone. Instead, a controlled disturbance should be input.

Though the azimuthal ring of DREs is not the optimal design for a controlled disturbance input, there exists evidence that it may still be sufficient to achieve at least a transitional boundary layer (Ward, 2014). As such, performing such experiments is the next step for boundary-layer measurements. However, it would also be useful to develop a more optimal DRE pattern. Such a pattern should be designed to lie on the branch-I neutral point for the most unstable wavenumber at at given axial location. This wavenumber very likely varies, and the neutral points will form a curve near the windward attachment line.

Should the DRE approach fail, a long, swept wedge would provide a configuration whose most unstable wavenumber is constant and much easier to effectively excite. The proper DRE design on such a configuration is already well-known. Depending on the tunnel geometry, it may also provide a greater distance over which the unstable wave can grow. As swept wedges are not typically featured in hypersonic vehicle design, such a study would be purely fundamental and useful primarily for comparison with computations rather than for its analogy with flight vehicle configurations.

Finally, in any future crossflow experiments, efforts should be made to use smaller

hot wires with greater frequency response. While the 280 kHz response of Hofferth (2013) is unnecessary for resolution of the $f \approx 110$ kHz type-I secondary instability, it may be necessary to detect the expected type-II instability. Further, the additional frequency response would allow a bicoherence analysis to detect any self-interaction of the type-I instability and potentially the interaction of type-I and type-II instabilities, which are expected to be spatially colocated.

6.2.3 General recommendations

6.2.3.1 Traversing mechanism

The traversing mechanism represents a significant step forward in the experimental capabilities of M6QT. However, as reported previously, one of the primary limitations on the number of points measurable in a single run is the azimuthal velocity of the traverse. This shortcoming may be easily solved in any future facility desiring such a system.

The current mechanism operates using a stationary, ring-like rack gear and a pinion gear attached to the moving carriage. This arrangement requires substantial torque and the use of a planetary gearhead with a large reduction ratio. If instead this situation is reversed, the ring gear may be allowed to rotate freely with a counterweight opposing the carriage to drastically reduce the torque requirement. The smaller gear could then be mounted mounted rigidly to the model mount and used with either a much smaller gearhead or no gearhead entirely, allowing much more rapid travel in azimuth. This approach has the added advantage of freeing up additional space in the carriage, allowing easier installation and radial travel range.

6.2.3.2 Infrared thermography

IR thermography has proven to be a valuable flow visualization technique and a means to rapidly iterate experimental configurations. However, at present the measurements are largely qualitative. A spatial and temperature calibration scheme would be useful for providing additional data.

Temperature calibration is relatively straightforward and the camera has built-in functions for performing the process. Calibrated temperature data would allow the approximation of surface heat transfer for use as a more definitive transition detection mechanism. As predicting the heat transfer rate is one of the primary goals of a hypersonic stability analysis on a vehicle, it would also provide a valuable point of comparison between experiments and computations. Constructing future models out of a matte, low-conductance material such as PEEK would greatly ease this effort due to its known heat transfer properties and the associated lack of a need for the insulating tape.

Spatial calibration would allow the pixels in the image to be accurately converted into their spatial location on the cone. This can be achieved through post-processing of the image data using a suitable calibration image. One possible way of achieving this is to produce a thin sheet that fits over the profile of the model in the region in question. This sheet would have a checkerboard-like pattern on it composed of rays of constant θ and arcs of constant z. A calibration image could then be used by the image processing software to transform the complex surface into a cartesian (z, θ)-plane.

6.2.3.3 Hot-wire calibration

While the uncalibrated measurements are still useful, it would, of course, be preferable to obtain calibrated data. A number of suggestions to this end were discussed by Hofferth (2013). However, as a result of the nearly linear King's law relationship of the probes used, performing a suitable approximate calibration may be feasible much more simply.

While the full range of pressures achievable under quiet flow cannot cover the entire range of of boundary-layer mass flux, it does cover as much as 2/3 of that range. Furthermore, a substantial portion of the unattainable range corresponds to the low portion of the boundary layer where transonic (and subsonic) flows render the tuning invalid anyway. As a result, an approximate calibration may be performed using a simple pressure sweep and some extrapolation out to the free-stream mass flux.

While extrapolation does introduce error into the calibration, the nature of this method is much simpler than previously proposed solutions in this facility and does not necessitate removal of the model. This allows wires to be calibrated on the fly as needed rather than calibrating many ahead of time without knowing how many will ultimately be necessary for the experiment.

6.2.3.4 Roughness elements

The water slide decal method of producing DREs holds great promise. However, the process is new and requires additional refinement. The overnight drying time required for the adhesion of the decals makes the application of multiple layers of roughness elements tedious and the durability of each decal layer has been variable from one batch to another. Further cooperation with companies capable of producing

such decals should focus on achieving thicker decals that eliminate the need for multiple layers and a more consistent quality of adhesion.

REFERENCES

Arnal, D. 1994 Boundary layer transition: Predictions based on linear theory. In *AGARD Special Course on Progress in Transition Modeling*, p. 63. N94-33884 10-34.

Balakumar, P. & Owens, L. R. 2010 Stability of Hypersonic Boundary Layers on a Cone at an Angle of Attack. In *40th AIAA Fluid Dynamics Conference and Exhibit*. Chicago, IL: AIAA 2010-4718.

Bippes, H. 1999 Basic experiments on transition in three-dimensional boundary layers dominated by crossflow instability. *Prog. Aero. Sci.* **35** (4), 363–412.

Bippes, H., Müller, B. & Wagner, M. 1991 Measurements and stability calculations of the disturbance growth in an unstable three-dimensional boundary layer. *Phys. Fluids A: Fluid Dynamics* **3** (10), 2371.

Bippes, H. & Nitschke-Kowsky, P. 1990 Experimental study of instability modes in a three-dimensional boundary layer. *AIAA J.* **28** (10), 1758–1763.

Blanchard, A. E., Lachowicz, J. T. & Wilkinson, S. P. 1997 NASA Langley Mach 6 Quiet Wind-Tunnel Performance. *AIAA J.* **35** (1), 23–28.

Bonfigli, G. & Kloker, M. 2007 Secondary instability of crossflow vortices: validation of the stability theory by direct numerical simulation. *J. Fluid Mech.* **583**, 229.

Borg, M. P. & Schneider, S. P. 2008 Effect of Freestream Noise on Roughness-Induced Transition for the X-51A Forebody. *J. Spacecraft and Rockets* **45** (6), 1106–1116.

Butler, K. M. & Farrell, B. F. 1992 Three-dimensional optimal perturbations in viscous shear flow. *Phys. Fluids A* **6** (8), 1637–1650.

Chen, F.-J., Wilkinson, S. P. & Beckwith, I. E. 1993 Görtler Instability and Hypersonic Quiet Nozzle Design. *J. Spacecraft and Rockets* **30** (2), 170–175.

Chokani, N. 1999 Nonlinear spectral dynamics of hypersonic laminar boundary layer flow. *Phys. Fluids* **11** (12), 3846.

Chokani, N. 2005 Nonlinear evolution of Mack modes in a hypersonic boundary layer. *Phys. Fluids* **17** (1), 014102.

Corke, T. C., Cavalieri, D. A. & Matlis, E. H. 2002 Boundary-Layer Instability on Sharp Cone at Mach 3.5 with Controlled Input. *AIAA J.* **40** (5).

Crawford, B. K. 2015 Laminar-turbulent transition due to 2-D excrescences at 1% chord on a swept wing. Doctoral dissertation, Texas A&M University.

Dagenhart, J. R., Saric, W. S., Hoos, J. A. & Mousseux, M. C. 1989*a* Experiments on Swept-Wing Boundary Layers. In *Laminar-Turbulent Transition, IUTAM Symposium*, pp. 369–80. Toulouse, France: Springer-Verlag Heidelberg.

Dagenhart, J. R., Saric, W. S., Mousseux, M. C. & Stack, J. P. 1989*b* Crossflow-vortex Instability and Transition on a 45-degree Swept Wing. In *20th AIAA Fluid Dynamics, Plasma Dynamics and Lasers Conference*. Buffalo, NY: AIAA 89-1892.

Demetriades, A. 1974 Hypersonic Viscous Flow Over a Slender Cone Part III: Laminar Instability and Transition. In *7th AIAA Fluid and Plasma Dynamics Conference*.

Deyhle, H. & Bippes, H. 1996 Disturbance growth in an unstable three-dimensional boundary layer and its dependence on environmental conditions. *J. Fluid Mech.* **316**, 73–113.

Deyhle, H., Höhler, G. & Bippes, H. 1993 Experimental Investigation of Instability Wave Propagation in a Three-Dimensional Boundary-Layer Flow. *AIAA J.* **31** (4), 637–45.

Doggett, G. P. & Wilkinson, S. P. 1997 Hypersonic boundary-layer stability experiments on a flared-cone model at angle of attack in a quiet wind tunnel. In *35th AIAA Aerospace Sciences Meeting*. Reno, NV: AIAA 97-0557.

Duncan, Jr., G. T. 2014 The effects of step excrescences on swept-wing boundary-layer transition. Doctoral dissertation, Texas A&M University.

Fedorov, A. V. 2011 Transition and Stability of High-Speed Boundary Layers. *Annu. Rev. Fluid Mech.* **43**, 79–95.

Gray, W. E. 1952 The effect of wing sweep on laminar flow. *Tech. Rep.*. Royal Aircraft Establishment, RAE TM Aero 255.

Gregory, N., Stuart, J. T. & Walker, W. S. 1955 On the Stability of Three-Dimensional Boundary Layers with Application to the Flow Due to a Rotating Disk. *Phil. Trans. R. Soc. A* **248** (943), 155–199.

Gronvall, J. E., Johnson, H. B. & Candler, G. V. 2012 Hypersonic Three-Dimensional Boundary Layer Transition on a Cone at Angle of Attack. In *42nd AIAA Fluid Dynamic Conference*. New Orleans, LA: AIAA 2012-2822.

Gustavsson, L. H. 1991 Energy growth of three-dimensional disturbances in plane Poiseuille flow. *J. Fluid Mech.* **224**, 241–260.

Haynes, T. S. & Reed, H. L. 2000 Simulation of swept-wing vortices using nonlinear parabolized stability equations. *J. Fluid Mech.* **405**, 325–349.

Herbert, T. 1997 Parabolized Stability Equations. *Annu. Rev. Fluid. Mech.* **29** (1), 245–283.

Hinich, M. J. & Wolinsky, M. 2005 Normalizing bispectra. *J. Stat. Planning and Inference* **130**, 405–411.

Hofferth, J. W. 2013 Boundary-Layer Stability and Transition on a Flared Cone in a Mach 6 Quiet Wind Tunnel. Doctoral dissertation, Texas A&M University.

Hofferth, J. W., Bowersox, R. D. W. & Saric, W. S. 2010 The Mach 6 Quiet Tunnel at Texas A&M: Quiet Flow Performance. In *27th AIAA Aerodynamic Measurement Technology and Ground Testing Conference*. Chicago, IL: AIAA 2010-4794.

Hofferth, J. W., Humble, R. A., Floryan, D. C. & Saric, W. S. 2013 High-Bandwidth Optical Measurements of the Second-Mode Instability in a Mach 6 Quiet Tunnel. In *51st AIAA Aerospace Sciences Meeting*. Grapevine, TX: AIAA 2013-0378.

Hofferth, J. W. & Saric, W. S. 2012 Boundary-Layer Transition on a Flared Cone in the Texas A&M Mach 6 Quiet Tunnel. In *50th AIAA Aerospace Sciences Meeting*. Nashville, TN: AIAA 2012-0923.

Hofferth, J. W., Saric, W. S., Kuehl, J. J., Perez, E., Kocian, T. S. & Reed, H. L. 2012 Boundary-Layer Instability & Transition on a Flared Cone in a Mach 6 Quiet Wind Tunnel. In *NATO RTO-AVT-200-10*.

Horvath, T. J., Berry, S. A., Hollis, B. R., Chang, C.-L. & Singer, B. A. 2002 Boundary Layer Transition on Slender Cones in Conventional and Low Disturbance Mach 6 Wind Tunnels. In *32nd AIAA Fluid Dynamics Conference and Exhibit*.

Hunt, L. E. 2011 Boundary-Layer Receptivity to Three-Dimensional Roughness Arrays on a Swept-Wing. PhD thesis.

Kendall, J. M. 1975 Wind Tunnel Experiments Relating to Supersonic and Hypersonic Boundary-Layer Transition. *AIAA J.* **13** (3), 290–299.

Kim, Y. C. & Powers, E. J. 1979 Digital Bispectral Analysis and Its Applications to Nonlinear Wave Interactions. *IEEE Tran. Plasma Sci.* **7** (2).

Kimmel, R. L. & Kendall, J. M. 1991 Nonlinear Disturbances in a Hypersonic Laminar Boundary Layer. In *29th Aerospace Sciences Meeting*. Reno, NV: AIAA 91-0320.

Klebanoff, P. S., Tidstrom, K. D. & Sargent, L. M. 1962 The three-dimensional nature of boundary-layer instability. *J. Fluid Mech.* **12** (1), 1–34.

Kocian, T. S., Perez, E., Oliviero, N. B., Kuehl, J. J. & Reed, H. L. 2013 Hypersonic Stability Analysis of a Flared Cone. In *51st AIAA Aerospace Sciences Meeting*. Grapevine, TX: AIAA 2013-0667.

Kohama, Y., Saric, W. S. & Hoos, J. A. 1991 A high-frequency, secondary instability of crossflow vortices that leads to transition. In *Proceedings of the Royal Aerospace Society, Boundary-Layer Transition Control Conference*, pp. 4.1–4.13. Cambridge, UK.

Kovasznay, L. S. G. 1950 The Hot-Wire Anemometer in Supersonic Flow. *J. Aero. Sci.* **17** (9), 565–572.

Kovasznay, L. S. G. 1953 Turbulence in Supersonic Flow. *J. Aero. Sci.* **20** (10), 657–674.

van den Kroonenberg, A., Radespiel, R., Candler, G. V. & Estorf, M. 2010 Infrared measurements of boundary-layer transition on an inclined cone at Mach 6. In *48th AIAA Aerospace Sciences Meeting*. Orlando, FL: AIAA 2010-1063.

Kuehl, J. J., Perez, E. & Reed, H. L. 2012 JoKHeR : NPSE Simulations of Hypersonic Crossflow Instability. In *50th AIAA Aerospace Sciences Meeting*. Nashville, TN: AIAA 2012-0921.

Lachowicz, J. T. & Chokani, N. 1996 Boundary-Layer Stability Measurements in a Hypersonic Quiet Tunnel. *AIAA J.* **34** (12), 2496–2500.

Landahl, M. T. 1980 A note on an algebraic instability of inviscid parallel shear flows. *J. Fluid Mech.* **98**, 243–251.

Lees, L. & Lin, C. C. 1946 Investigation of the Stability of the Laminar Boundary Layer in a Compressible Fluid. *Tech. Rep.*. NACA Tech. Note No. 1115, Washington, D.C.

Luersen, R. P. K. 2012 Techniques for application of roughness for manipulation of second-mode waves on a flared cone at Mach 6. Masters thesis, Purdue University.

Mack, L. M. 1969 Boundary-Layer Stability Theory. *Tech. Rep.*. Jet Propulsion Laboratory, Doc. No. 900-277, Rev. A., Pasadena, CA.

Mack, L. M. 1984 Boundary-Layer Linear Stability Theory. *AGARD Report No. 709* .

Malik, M. R., Li, F. & Chang, C.-L. 1994 Crossflow disturbances in three-dimensional boundary layers: nonlinear development, wave interaction and secondary instability. *J. Fluid Mech.* **268**, 1–36.

Malik, M. R., Li, F. & Chang, C.-L. 1996 Nonlinear crossflow disturbances and secondary instabilities in swept-wing boundary layers. In *IUTAM Symposium on Nonlinear Instability and Transition in Three-Dimensional Boundary Layers* (ed. Philip W Hall & P. W. Duck), pp. 257–266.

Muñoz, F., Heitmann, D. & Radespiel, R. 2014 Instability Modes in Boundary Layers of an Inclined Cone at Mach 6. *J. Spacecraft and Rockets* **51** (2), 442–454.

Perez, E., Reed, H. L. & Kuehl, J. J. 2013 Instabilities on a Hypersonic Yawed Straight Cone. In *43rd AIAA Fluid Dynamics Conference*. San Diego, CA: AIAA 2013-2879.

Prandtl, L. 1904 Über Flüssigkeitsbewegung bei sehr kleiner Reibung. *Verhaldlg III Int. Math. Kong.* pp. 484– 491.

Reed, H. L. & Saric, W. S. 1989 Stability of Three-Dimensional Boundary Layers. *Annu. Rev. Fluid Mech.* **21** (1), 235–284.

Reed, H. L., Saric, W. S. & Arnal, D. 1996 Linear Stability Theory Applied to Boundary Layers. *Annu. Rev. Fluid Mech.* **28**, 389–428.

Reibert, M. S., Saric, W. S., Carrillo, Jr., R. B. & Chapman, K. L. 1996 Experiments in Nonlinear Saturation of Stationary Crossflow Vortices in a Swept-Wing Boundary Layer. In *34th AIAA Aerospace Sciences Meeting*. Reno, NV: AIAA 96-0184.

Reshotko, E. 2001 Transient growth: A factor in bypass transition. *Phys. Fluids* **13** (5), 1067.

Reshotko, E. 2007 Is Re_θ/M_e a Meaningful Transition Criterion? *AIAA J.* **45** (7), 1441–1443.

Reynolds, O. 1883 An Experimental Investigation of the Circumstances Which Determine Whether the Motion of Water Shall Be Direct or Sinuous, and of the Law of Resistance in Parallel Channels. *Phil. Trans. R. Soc. London* **174**, 935–982.

Saric, W. S., Carrillo, Jr., R. B. & Reibert, M. S. 1998 Leading-Edge Roughness as a Transition Control Mechanism. In *36th Aerospace Sciences Meeting & Exhibit*. AIAA 98-0781.

Saric, W. S., Reed, H. L. & Kerschen, E. J. 2002 Boundary-Layer Receptivity to Freestream Disturbances. *Annu. Rev. Fluid Mech.* **34**, 291–319.

Saric, W. S., Reed, H. L. & White, E. B. 2003 Stability and Transition of Three-Dimensional Boundary Layers. *Annu. Rev. Fluid Mech.* **35** (1), 413–440.

Schmid, P. J., Henningson, D. S., Khorrami, M. R. & Malik, M. R. 1993 A study of eigenvalue sensitivity for hydrodynamic stability operators. *Theo. Comp. Fluid Dynamics* **4**, 227–240.

Schneider, S. P. 2007 The Development of Hypersonic Quiet Tunnels. In *37th AIAA Fluid Dynamics Conference and Exhibit*.

Schuele, C. Y., Corke, T. C. & Matlis, E. H. 2013 Control of stationary cross-flow modes in a Mach 3.5 boundary layer using patterned passive and active roughness. *J. Fluid Mech.* **718**, 5–38.

Semper, M. T. 2013 Examining a hypersonic turbulent boundary layer at low Reynolds number. Doctoral dissertation, Texas A&M University.

Semper, M. T., Tichenor, N. R., Bowersox, R. D. W., Srinivasan, R. & North, S. W. 2009 On the Design and Calibration of an Actively Controlled Expansion Hypersonic Wind Tunnel. In *47th AIAA Aerospace Sciences Meeting*. Orlando, FL: AIAA 2009-799.

Shiplyuk, A. N., Bountin, D. A., Maslov, A. A. & Chokani, N. 2003 Nonlinear mechanisms of the initial stage of the laminar-turbulent transition at hypersonic velocities. *J. Appl. Mech. Tech. Phys.* **44** (5), 654–659.

Sivasubramanian, J. & Fasel, H. F. 2012*a* Growth and Breakdown of a Wave Packet into a Turbulent Spot in a Cone Boundary Layer at Mach 6. In *50th AIAA Aerospace Sciences Meeting*. Nashville, TN: AIAA 2012-0085.

Sivasubramanian, J. & Fasel, H. F. 2012*b* Nonlinear Stages of Transition and Breakdown in a Boundary Layer on a Sharp Cone at Mach 6. In *50th AIAA Aerospace Sciences Meeting*. Nashville, TN: AIAA 2012-0087.

Smith, A. M. O. & Gamberoni, N. 1956 Transition, pressure gradient and stability theory. *Tech. Rep.*. Douglas Aircraft Company, Report No. ES 26388.

Smits, A. J., Hayakawa, K. & Muck, K. C. 1983 Constant Temperature Hot-wire Anemometer Practice In Supersonic Flows - Part 1: The Normal Wire. *Exp. Fluids* **1** (2), 83–92.

Stetson, K. F. 1982 Mach 6 Experiments of Transition on a Cone at Angle of Attack. *J. Spacecraft and Rockets* **19** (5), 397–403.

Stetson, K. F. & Kimmel, R. L. 1992 On Hypersonic Boundary-Layer Stability. *Aerospace Sciences Meeting* .

Stetson, K. F., Thompson, E. R., Donaldson, J. C. & Siler, L. G. 1983 Laminar boundary layer stability experiments on a cone at Mach 8, part 1: sharp cone. In *AIAA 16th Fluid and Plasma Dynamics Conference*. Danvers, MA: AIAA 83-1761.

Swanson, E. O. & Schneider, S. P. 2010 Boundary-Layer Transition on Cones at Angle of Attack in a Mach-6 Quiet Tunnel. In *49th AIAA Aerospace Sciences Meeting*. Orlando, FL: AIAA 2010-1062.

Trefethen, L. N., Trefethen, A. E., Reddy, S. C. & Driscoll, T. A. 1993 Hydrodynamic Stability. *Science* **261**, 578–584.

Van Ingen, J. L. 1956 A suggested semi-empirical method for the calculation of the boundary layer transition region. *Tech. Rep.*. Delft Univ. Tech. Rep. No. VTH 74.

Ward, C. A. C. 2014 Crossflow Instability and Transition on a Circular Cone at Angle of Attack in a Mach-6 Quiet Tunnel. Doctoral dissertation, Purdue University.

Wassermann, P. & Kloker, M. 2002 Mechanisms and passive control of crossflow-vortex-induced transition in a three-dimensional boundary layer. *J. Fluid Mech.* **456**, 49–84.

White, E. B. & Saric, W. S. 2005 Secondary instability of crossflow vortices. *J. Fluid Mech.* **525**, 275–308.

APPENDIX A

BISPECTRAL ANALYSIS

Traditional spectral methods such as the power spectral density assume that the boundary-layer disturbance spectrum is composed of linearly independent, superposed waves. In reality, the disturbance spectrum in a laminar boundary layer is broadband and often involves highly nonlinear processes and wave interactions. The power spectral density therefore provides little information about the nonlinear nature of the flow.

Higher-order spectra such as the bispectrum (Kim & Powers, 1979) offer the ability to quantitatively analyze nonlinear effects in experimental data through the phase coupling of different frequency components. Kimmel & Kendall (1991) first applied bispectral techniques to the study of boundary-layer stability in a hypersonic boundary layer in a conventional wind tunnel environment. This study used the autobicoherence to explain the the appearance of frequency components not predicted by LST. Similar analysis was performed by Shiplyuk *et al.* (2003). Chokani (1999) extended bispectral techniques into a low-disturbance environment, where the nonlinear processes were found to largely agree with the conventional data. The first use of the cross-bicoherence was performed by Chokani (2005).

While Kim & Powers (1979) provides a rather complete treatment of bispectral analysis, a brief explanation is provided here. First, let $X(f) = \mathcal{F}[x(t)]$ be the discrete Fourier transform of some time series (such as a hot-wire signal) $x(t)$ at the discrete frequency f. Then the bispectrum, $B(f_1, f_2)$ is defined as

$$B(f_1, f_2) = E[X(f_1)X(f_2)X^*(f_1 + f_2)], \tag{A.1}$$

where f is frequency, * denotes the complex conjugate, and $E[\cdot]$ is the expectation operator.

The non-normalized bispectrum is easily dominated by spectral components with high energy and sometimes marginalizes less energetic components with a greater degree of phase coherence. As a result, it is advantageous to normalize the bispectrum in order to accurately reflect the relative degree of phase coupling independent of the spectral energy. There are multiple means of normalization, and while Hinich & Wolinsky (2005) suggest that the method favored by Kim & Powers (1979) and (Chokani, 2005) may not be statistically the most correct, it is used in the present study for the sake of consistency with exiting boundary layer literature. The bicoherence, b^2, is defined as

$$b^2(f_1, f_2) = \frac{|B(f_1, f_2)|^2}{E\left[|X(f_1)X(f_2)|^2\right] E\left[|X(f_1 + f_2)|^2\right]}. \tag{A.2}$$

For physical intuition, consider three waves with frequencies f_1, f_2, and $f_3 = f_1 + f_2$. Representing their Fourier transforms exponentially in Equation A.1,

$$B(f_1, f_2) = E[r_1 r_2 r_3 e^{i(\theta_1 + \theta_2 - \theta_3)}]. \tag{A.3}$$

For a windowed time signal, $x(t)$, if the quantity $\theta_1 + \theta_2 - \theta_3$ is constant across all windows, then the exponential term will have the same phase in each window. When taking the mean, its coefficients sum and $b^2 \to 1$. If the waves are instead independent and the phases are randomly distributed, they will tend to offset one another in the mean and $b^2 \to 0$. A high value of b^2 therefore indicates the nonlinear interaction of f_1 with f_2 to produce $f_1 + f_2$, often denoted $(f_1, f_2) \to f_1 + f_2$.

The bicoherence spectrum has the following symmetry:

$$b^2(f_1, f_2) = b^2(f_2, f_1) = b^2(-f_1, -f_2). \tag{A.4}$$